International Workshop

Regional Climate Models-II

Novetel Ambassador Busan, Korea ; September 10-12, 2013

Program & Abstract

MIMISTRY OF
OCEANS AND FISHERIES

RIO

PICES

▶Organized by Research Institute of Oceanography, Seoul National University

▶Supported by OCCAPA Program/Ministry of Oceans and Fisheries
RIO/Seoul National University
North Pacific Marine Science Organization (PICES)

International Workshop

Development and Application of Regional Climate Models-II

General Information

We have the pleasure of announcing the Regional Climate Modeling Workshop II following its successful first workshop in Seoul, Korea in 2011. The workshop was motivated with the realization that physically-based regional climate projections are the starting point for many socio-economic impact and adaptation considerations to future climate. While the global coupled models capture large-scale climate behavior, they have limitations for regional assessment due to their coarse spatial resolutions and lack of regionally important physical processes. As was the case in the 1st workshop, we invite presentations that discuss the regional climate projections based on ocean or coupled models, novel downscaling techniques including implementation of surface and lateral boundary conditions, and existing roadblocks. We also encourage papers to consider both physics and biogeochemistry.

Extending the scope of the workshop, we also invite presentations for the 2nd workshop that discuss some pivotal physical and biological processes important to climate projections focusing on ocean's sub-mesoscale motions. There is considerable current interest in motions in the ocean on the sub-mesoscale and their impact on the marine ecosystem. Understanding the fundamental physics of these motions, their influence on lateral and vertical transports, and how they influence the functioning of the marine ecosystem is necessary in order to be able to assess likely changes and shifts to the system under a changing climate. The presentations will discuss the following key questions; How much do we know? Do we know enough to be able to say with confidence how conditions at these scales may change? What are the major unanswered questions? Other oceanographic processes important to the regional climate projections will also be addressed.

Also invited are presentations on the climate variability of and changes in physical and biogeochemical properties in the North Pacific based on long-term observational data and climate models.

Dates and venue

The workshop will be held on September 10 – 12, 2013, at Novotel Ambassador Busan (BallroomC/5F), Busan, Korea.

Conveners

Kyung-Il Chang
School of Earth and Environmental Sciences, Seoul National University
E-mail) kichang@snu.ac.kr

Enrique Curchitser
Institute of Marine and Coastal Sciences, Rutgers University
E-mail: enrique@marine.rutgers.edu

Chan Joo Jang
Ocean Circulation and Climate Research Division, Korea Institute of Ocean Science and Technology
E-mail) cjjang@kiost.ac

Kelvin Richards
International Pacific Research Center/Department of Oceanography
University of Hawaii at Manoa
E-mail) rkelvin@hawaii.edu

Sponsors

OCCAPA Program funded by Ministry of Oceans and Fisheries, Korea
Research Institute of Oceanography (RIO), Seoul National University
North Pacific Marine Science Organization (PICES)

HOTEL INFORMATION/LOCATION

☐ **NOVOTEL AMBASSADOR BUSAN (http://www.novoelbusan.com)**

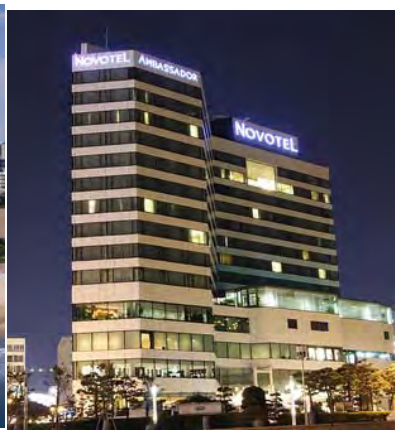

Address : 1405-16, Jung-Dong, Haeudaegu, Busan, Korea

Tel : 82-51-743-1234 Fax : 82-51-743-1250

From GIMHAE International Airport (http://www.airport.co.kr/mbs/gimhae)

- Limousine Bus:

  Cost : Adult-KRW 7,000, Kid-KRW 4,500

  Operation Hours : every 20 minutes

  To Hotel 7:10 ~ 21:40 Airport 5:10 ~ 19:50

- Bus No.: 307

- Taxi : 1hour, Fee : About KRW 25,000

PROGRAM

Program

September 10 (Tuesday), 2013

08:30-09:30 **Registration**

09:30-09:40 **Welcoming Address**

Mr. Hyung-Ki Nam

(Director General for Marine Environment Policy Bureau, Ministry of Oceans and Fisheries)

09:40-09:50 **PICES Welcome**

Dr. Skip McKinnell

(Deputy Executive Secretary, PICES)

Session I. Important Processes in RCM: Mesoscale and Submesoscale Motions

Kelvin Richards, Presiding

10:00-10:10 ***Kelvin Richards (Univ. Hawaii, USA)***
Session introduction

10:10-10:50 ***Hidenori Aiki (JAMSTEC, Japan)***
Energetics of the global ocean: the role of mesoscale eddies

10:50-11:30 ***Annalisa Bracco (Georgia Tech. Univ., USA)***
Submesoscale dynamics and transport properties in the Gulf of Mexico

11:30-12:10 ***Hideharu Sasaki (JAMSTEC, Japan)***
Seasonality of submesoscale activity around the Kuroshio Extension in a high-resolution simulation

12:10-14:00 *Lunch Break*

Session I. Important Processes in RCM: Mesoscale and Submesoscale Motions

Annalisa Bracco, Presiding

14:00-14:40 ***Paulo Calil (FURG, Brazil)***
Biological relevance of submesoscale dynamics in the highly stratified oligotrophic ocean

14:40-15:20 ***Chris Edwards (UCSC, USA)***
Spatiotemporal variability of air-sea CO2 exchange in the California

Current

15:20-16:00 ***Kelvin Richards (Univ. Hawaii, USA)***
Physical controls on biological production in the North Pacific sub-tropical gyre

16:00-16:30 *Tea/Coffee Break*

Session I. Important Processes in RCM: Mesoscale and Submesoscale Motions

Hidenori Aiki, Presiding

16:30-17:10 ***Hajoon Song (MIT, USA)***
Effect of eddies in the Southern Ocean ventilation

17:10-17:50 ***Kyung-Il Chang (SNU, Korea)***
Eddy statistics in the East/Japan Sea based on satellite altimetric data and numerical model

September 11 (Wednesday), 2013

Session II. Regional Climate & Ecosystem Projections

Enrique Curchitser, Presiding

09:00-09:10 ***Enrique Curchitser (Rutgers Univ., USA)***
Session introduction

09:10-09:50 ***Kwang-Yul Kim (SNU, Korea)***
Prescription of uncontaminated open boundary conditions for regional ocean model simulations of future climate

09:50-10:30 ***Michael Foreman (IOS, Canada)***
Regional ocean climate projections for the British Columbia continental shelf

10:30-11:00 *Tea/coffee break*

Session II. Regional Climate & Ecosystem Projections

Michael Foreman, Presiding

11:00-11:40 ***Enrique Curchitser (Rutgers Univ., USA)***
Multi-scale modeling of eastern boundary currents

11:40-12:20 ***Jason Holt (NOC, UK)***
Towards reliable climate impacts projections of shelf and coastal sea ecosystems

12:20-14:00 *Lunch Break*

Session II. Regional Climate & Ecosystem Projections

Jason Holt/Yang-Ki Cho, Presiding

14:00-14:40 ***Yang-Ki Cho (SNU, Korea)***
Future climate change projection of northwestern Pacific marginal seas by dynamical downscaling of the GCMs

14:40-15:20 ***Ping Chang (Texas A&M Univ., USA)***
Frontal-scale air-sea interactions along the Gulf Stream simulated by a

convection-resolving/eddy-resolving coupled regional climate model

15:20-16:00 ***Hyodae Seo (WHOI, USA)***

On the effect of marginal Sea SST variability on the North Pacific atmospheric circulation

16:00-16:40 ***Liwei Zou (IAP, China)***

Can a regional ocean-atmosphere coupled model improve the simulation of the interannual variability of the western North Pacific summer monsoon ?

Poster Session (16:40-18:00)

Uk Jae Jung (SNU, Korea) A Comparison of Surface Turbulent Heat Fluxes over the East Asian Marginal Seas

Doyoun Kim (ARA Co., Korea) Development of regional and coastal operational hydrodynamic/wave forecasting system in Korea

Youngji Joh (KIOST, Korea) An improvement of reproducibility of Pacific decadal oscillation in CMIP 5

Chun-Yong Jung (KIOST, Korea) Dynamical downscaling of future projections of precipitation change over the East Asia

Chul Min Ko (KIOST, Korea) Development of Regional Climate Model for western North Pacific: Assessment of a present ocean climate simulation

Minwoo Kim (KIOST, Korea) Effect of grid refinement in the global ocean circulation experiments

Dongwon Yi (KIOST, Korea) Effects of mixed layer depth on the changes in the sea surface temperature under global warming in CMIP5 models

Seung-Tae Yoon (SNU, Korea) Decadal variability and cooling trend of intermediate layer heat content in the southwestern East/Japan Sea

Banquet (18:30-20:30) **IRISroom (4F)**

September 12 (Thursday), 2013

Session III. Climate Variability in the North Pacific

Kwang-Yul Kim, Presiding

09:00-09:40 ***Shoshiro Minobe (Hokkaido Univ., Japan)***
Regional influence of basin-scale wind stress variability via jet-trapped Rossby waves in the western North Pacific

09:40-10:20 ***Benjamin Hamlington (Univ. Colorado, USA)***
Contribution of the Pacific Decadal Oscillation to global mean sea level trends

10:20-11:00 ***Robert Leben (Univ. Colorado, USA)***
Multi-Decadal Variability of Sea Level in the Southeast and Northeast Asian Seas

11:00-11:30 *Tea/coffee break*

Wrap-up and Recommendations (11:30-12:30)

Kelvin Richards/Enrique Curchitser, Presiding

Session summaries

1st & 2nd RCMs: Improvement & remaining issues

How do modelers feel the submesoscale processes ? Are they accounted for in their models ?

How do speakers on the submesoscale processes feel the current RCM activities ? Are they satisfactory in terms of meso- and submesoscale processes ? How to improve them ?

What else the important processes in the development of RCMs ?

Deliverables of the workshop, special issue ?

Necessity of the 3rd workshop

Presenters

Hidenori Aiki
Research Institute for Global Change
Japan Agency for Marine-Earth Science and Technology (JAMSTEC)
3173-25 Showamach, Kanazawa-ku, 236-0001, Yokohama
Japan
Phone : +81-45-778-5524
E-mail : aiki@jamstec.go.jp

Annalisa Bracco
School of Earth and Atmospheric Sciences
Georgia Institute of Technology
311 Ferst Dr., 30332, Atlanta, GA
USA
Phone : +1-404-894-1749
E-mail : abracco@gatech.edu

Paulo Calil
Instituto de Oceanografia
Universidade Federal do Rio Grande (FURG)
AvenidaItália,km.08 CEP96201-900RioGrande-RS
Brasil
Phone : +55-5384580508
E-mail : paulo.calil@furg.br

Ping Chang
Dept. of Oceanography and Dept. of Atmospheric Sciences
Texas A & M University
3146 TAMU,O&M Building, Room624, 77843 College Station, Texas
USA
Phone : +1-979-845-8196
E-mail : ping@tamu.edu

Kyung-Il Chang
School of Earth Environmental Science
Seoul National University
1 Gwanak-ro, Gwanak-gu, Seoul, 151-742
Korea
Phone : +82-2-880-6747
E-mail : kichang@snu.ac.kr

Yang-Ki Cho
School of Earth Environmental Science
Seoul National University
1 Gwanak-ro, Gwanak-gu, Seoul, 151-742
Korea

Phone : +82-2-880-6749
E-mail : choyk@snu.ac.kr

Enrique Curchitser
Dept. of Environmental Sciences, Institute of Marine and Coastal Sciences
Rutgers University
14 College Farm Rd., 08901, New Brunswick
USA
Phone : +1-848-932-7889
E-mail : enrique@marine.rutgers.edu

Chris Edwards
Dept. of Ocean Sciences
University of California
95065, Santa Cruz, CA
USA
Phone : +1-831-459-3734
E-mail : cedwards@ucsc.edu

Mike Foreman
Fisheries and Oceans Canada
Institute of Ocean Sciences
P.O.Box 6000, V8L 4B2, Sidney
Canada
Phone : + 1-250-363-6306
E-mail : mike.Foreman@dfo-mpo.gc.ca

Benjamin Hamlington
Cooperative Institute for Research in Environmental Science
University of Colorado at Boulder
216 UCB, 80309, Boulder
USA
Phone : +1-3034924113
E-mail : hamlingt@colorado.edu

Jason Holt
National Oceanography Centre
6Brownlow street, L3 5DA, Liverpool
UK
Phone : +44-776178675
E-mail : jholt@pol.ac.uk

Youngji Joh
Ocean Circulation and Climate Research Division
Korea Institute of Ocean Science and Technology (KIOST)
1270 Sa2-dong, SangRok-gu, 426-744, Ansan

Korea
Phone : +82-10-2999-4806
E-mail : yj_joh@kiost.ac

Chun-Young Jung
Ocean Circulation and Climate Research Division
Korea Institute of Ocean Science and Technology (KIOST)
1270 Sa2-dong, SangRok-gu, 426-744, Ansan
Korea
Phone : +82-10-2226-1621
E-mail : cyjung@kiost.ac

Uk Jae Jung
Research Institute of Oceanography
Seoul National University
1 Gwanak-ro, Gwanak-gu, Seoul, 151-742
Korea
Phone : +82-2-872-1679
Email : ujjung@curl.snu.ac.kr

Kwang-Yul Kim
School of Earth Environmental Science
Seoul National University
1 Gwanak-ro, Gwanak-gu, Seoul, 151-742
Korea
Phone : +82-2-880-4205
E-mail : kwang56@snu.ac.kr

Doyoon Kim
R&D center
ARA Consulting & Technology
SMART valley D-1510, 30, Songdomirae-ro, Yeonsu-gu, 406-840, Incheon
Korea
Phone : +82-70-7585-5436
E-mail : Doyoun71@gmail.com

Minwoo Kim
Ocean Circulation and Climate Research Division
Korea Institute of Ocean Science and Technology (KIOST)
787 Haean-ro, SangRok-gu, 426-744, Ansan
Korea
Phone : +82-10-9326-0518
E-mail : endowkim@nate.com

Chul Min Ko
Ocean Circulation and Climate Research Division

Korea Institute of Ocean Science and Technology (KIOST)
787 Haean-ro, SangRok-gu, 426-744, Ansan
Korea
Phone : +82-10-5380-8978
E-mail : kkobchul@kiost.ac

Robert R. Leben
Aerospace Engineering Sciences
University of Colorado at Boulder
Campus Box 431, 80309-0431, Boulder
USA
Phone : +1-3034924113
E-mail : Robert.Leben@colorado.edu

Shoshiro Minobe
Graduate School of Science
Hokkaido University
3F Rigaku 8 building, N10, W8, 060-0810, Sapporo
Japan
Phone : +81-11-706-2644
E-mail : minobe@mail.sci.hokudai.ac.jp

Kelvin Richards
International Pacific Research Center
University of Hawaii
1680 East West Road, 96822, Honolulu
USA
Phone : +1-808-398-8480
E-mail : rkelvin@hawaii.edu

Hideharu Sasaki
Earth Simulator Center
Japan Agency for Marine-Earth Science and Technology (JAMSTEC)
3173-25 Showa-machi, Kanazwa-ku, 236-0001, Yokohama
Japan
Phone : +81-45-778-5843
E-mail : sasaki@jamstec.go.jp

Hyodae Seo
Physical Oceanography Dept.
Woods Hole Oceanographic Institution
266 Woods Hole Road, MS#21, 02543, Woods Hole
USA
Phone : +1-774-392-3196
E-mail : hseo@whoi.edu

Hajsong Song
Department of Earth, Atmospheric and Planetary Sciences
Massachusetts Institute of Technology (MIT)
77 Massachusetts Ave., 02139, Cambridge
USA
Phone : +1-617-253-0098
E-mail : hajsong @mit.edu

Dongwon Yi
Ocean Circulation and Climate Research Division
Korea Institute of Ocean Science and Technology (KIOST)
1270 Sa2-dong, SangRok-gu, 426-744, Ansan
Korea
Phone : +82-31-400-7738
E-mail : yidongwonyi@gmail.com

Seung-Tae Yoon
School of Earth Environmental Science
Seoul National University
1 Gwanak-ro, Gwanak-gu, Seoul, 151-742
Korea
Phone : +82-2-872-1679
E-mail : styoon@curl.snu.ac.kr

Liwei Zou
LASG
Institute of Atmospheric Physics
Hua YanLi No.40, QiJiaHuoZi, Chaoyang District, P.O.Box 9804, 100029, Beijing
China
Phone : +8610-82995453
E-mail : zoulw@mail.iap.ac.cn

ABSTRACTS

Session I

Important Processes in RCM: Mesoscale and Submesoscale Motions

Energetics of the global ocean: the role of mesoscale eddies

Hidenori Aiki[1], Xiaoming Zhai[2], Richard J. Greatbatch[3]

[1]Research Institute for Global Change, Japan Agency for Marine-Earth Science and Technology, Yokohama, Japan [2]School of Environmental Sciences, University of East Anglia, Norwich, UK
[3]GEOMAR Helmholtz-Zentrum fur Ozeanforschung, Kiel, Germany
E-mail: aiki@jamstec.go.jp

Despite several theoretical studies in various research areas of atmosphere and ocean dynamics (cf. Rhines and Young, 1979; Andrews, 1983; Johnson and Bryden, 1989), the vertical redistribution of momentum by layer-thickness form stress and associated energy conversions have been little investigated based on output from high-resolution OGCMs. This is more or less a result of the four-box energy diagram of Lorenz (1955) being exclusively used in previous studies. For example, the pioneering paper by Holland and Lin (1975) included a diagnosis of the energetics of eddies and wind-driven circulation as simulated by a two-layer model. Holland and Lin (1975) used an energy diagram which is similar to that of Lorenz (1955) and hence there is no term representing the layer-thickness form stress. As will be shown in this talk, it is possible to revise the definition of the mean and eddy kinetic energies (KEs) in Holland and Lin (1975), with a consequence that the revised energy diagram involves an energy conversion term representing the role of the layer-thickness form stress (Fig. 1a).

In order to illustrate the energy cycle in the new energy diagram, we use a set of 3-day snapshots from a high-resolution (0.1-deg) near-global hindcast simulation. This simulation is called the OFES (OGCM for the Earth Simulator) hindcast run, and was forced by daily mean wind stress from the QuickSCAT data and daily-mean heat and fresh water fluxes from the NCEP/NCAR reanalysis (Masumoto, 2010). A set of 3-day snapshots archived throughout years 2004-2007 of the OFES hindcast run were used for the diagnosis (a total of 483 three-dimensional snapshots of the global ocean). These snapshots were originally in z-coordinates. The model has 54 depth levels, with the discretization varying from 5 m at the surface to 330 m at the maximum depth of 6065 m. Each snapshot was first mapped onto density coordinates in each vertical column. As in Aiki and Richards (2008, JPO), we use 80 density layers defined by the potential density referenced to sea surface pressure. This density was chosen in an attempt to overview the global ocean with most of the KE distributed above the main thermocline. In the present diagnosis, the low-pass temporal filter (overbar) was set to a four-year mean for 2004 to 2007. We have determined the global distribution of energy conversion terms concerning the budget of the mean KE in Fig. 1a. These are $-\overline{h}\overline{\mathbf{V}}\cdot\nabla\overline{\phi}$, $-\overline{h}\overline{\mathbf{V}}^{B}\cdot\nabla\overline{\phi}$, $-\hat{\mathbf{V}}\cdot\overline{h'''\nabla\phi'''}$, $-\rho_0\hat{\mathbf{V}}\cdot[\nabla\cdot(\overline{h\mathbf{V}''\mathbf{V}''})]$, for each of which the depth-integral in each vertical column is plotted in Fig. 2 with negative (positive) values indicating a decrease (increase) in the mean KE.

Whilst significant positive and negative signs are evident in the work of the isopycnal mean velocity $-\overline{h}\overline{\mathbf{V}}\cdot\nabla\overline{\phi}$ (Fig. 2a), the working rate in the model-global ocean integrates to −0.77 TW

(negative, 1 TW = 10^{12} watts), which indicates conversion of the mean KE to the mean PE. This quantity mainly reflects the wind-induced Ekman flow steepening the slope of isopycnal surfaces near the sea surface. Strictly speaking, the work of the isopycnal 229 mean velocity includes also the effects of continental-drag Ekman flow (associated with the sum of the horizontal friction term and the bottom friction term in the model), which is represented by the positive signals near the western boundaries of the Pacific, Atlantic and Indian Oceans, in particular the Greenland Sea, the upstream of the Kuroshio and the Gulf Stream, and the Agulhas Current. These positive signals indicate conversion of mean PE to mean KE, which is then dissipated by the boundary friction at the continental slope of the ocean. [See Aiki, Richards, and Sakuma (2011, Ocean Dynamics) for the global distribution of the energy dissipation by the boundary friction in the 0.1-deg OFES simulation; the working rate by the boundary friction integrates to −0.32 TW in the model-global ocean, not shown.] The work done by the bolus velocity, $-\overline{h}\mathbf{V}^B\cdot\nabla\overline{\phi}$, is shown in Fig. 3b. This quantity is clearly positive over each region of high eddy activity in the global ocean: mean PE is extracted to provide an input to the mean KE when the eddy-induced overturning circulation relaxes the slope of isopycnal surfaces. The working rate in the model-global ocean integrates to +0.87 TW. The fact that the global distribution is mostly positive indicates that this quantity provides a suitable basis for mesoscale eddy parameterization in climate ocean models, and is consistent with Gent et al. (1995, JPO).

The work done by the layer-thickness form stress, $-\hat{\mathbf{V}}\cdot\overline{h'''\nabla\phi'''}$, is shown in Fig. 2c, where negative values indicate an energy cascade to the eddy field associated with the relaxation of the vertical shear of the geostrophic currents. The horizontal distribution of the work done by the layer-thickness form stress is partly anti-correlated with the work done by the bolus velocity in Fig. 3b. Nevertheless, there are also positive signals, for example, in the Kuroshio Extension region. The working rate in the model global ocean integrates to −0.48 TW. The work done by the Reynolds stress, $-\rho_0\hat{\mathbf{V}}\cdot[\nabla\cdot(\overline{h\mathbf{V}''\mathbf{V}''})]$, is shown in Fig. 2d. The working rate in the model-global ocean integrates to −0.15 TW, suggesting an energy cascade to the eddy field associated with the relaxation of the lateral shear of the geostrophic currents. This might indicate the effect of barotropic instability, for example, at the western boundary of the Indian Ocean, and in the Kuroshio and the Gulf Stream regions. However in the Gulf Stream extension region, the signal is clearly positive, indicating acceleration of the mean current by the eddies (Held and Andrews, 1983; Greatbatch et al., 2010; Waterman and Jayne, 2011), in which the meridional radiation of Rossby waves could play a role (Thompson, 1971).

To summarize, the equilibrium of the mean KE in the wind-driven ocean circulation is maintained by the following energy cycle. Wind forcing provides an input to the mean KE, which is then transferred to the mean PE by the wind-induced Ekman flow (the role of the isopycnal mean velocity $\overline{\mathbf{V}}$). Nevertheless, the net mean PE does not change, because the eddy-induced overturning circulation (the role of the bolus velocity $\mathbf{V}^B$) extracts some of the mean PE and feeds the mean KE, which is subsequently drained by the work of the layer-thickness form stress term −h000rÁ000, endowing the eddy field with an energy cascade. The result of the above diagnosis is complementary to Aiki and Richards (2008) in that (i) we also identify the work of the Reynolds stress term, (ii) our statistics is based on a four-year mean of 3-day snapshots instead of monthly means of 3-day snapshots, (iii) we use the output of a hindcast simulation

forced by daily-mean atmospheric forcing instead of a climatological simulation forced by monthly-mean atmospheric forcing.

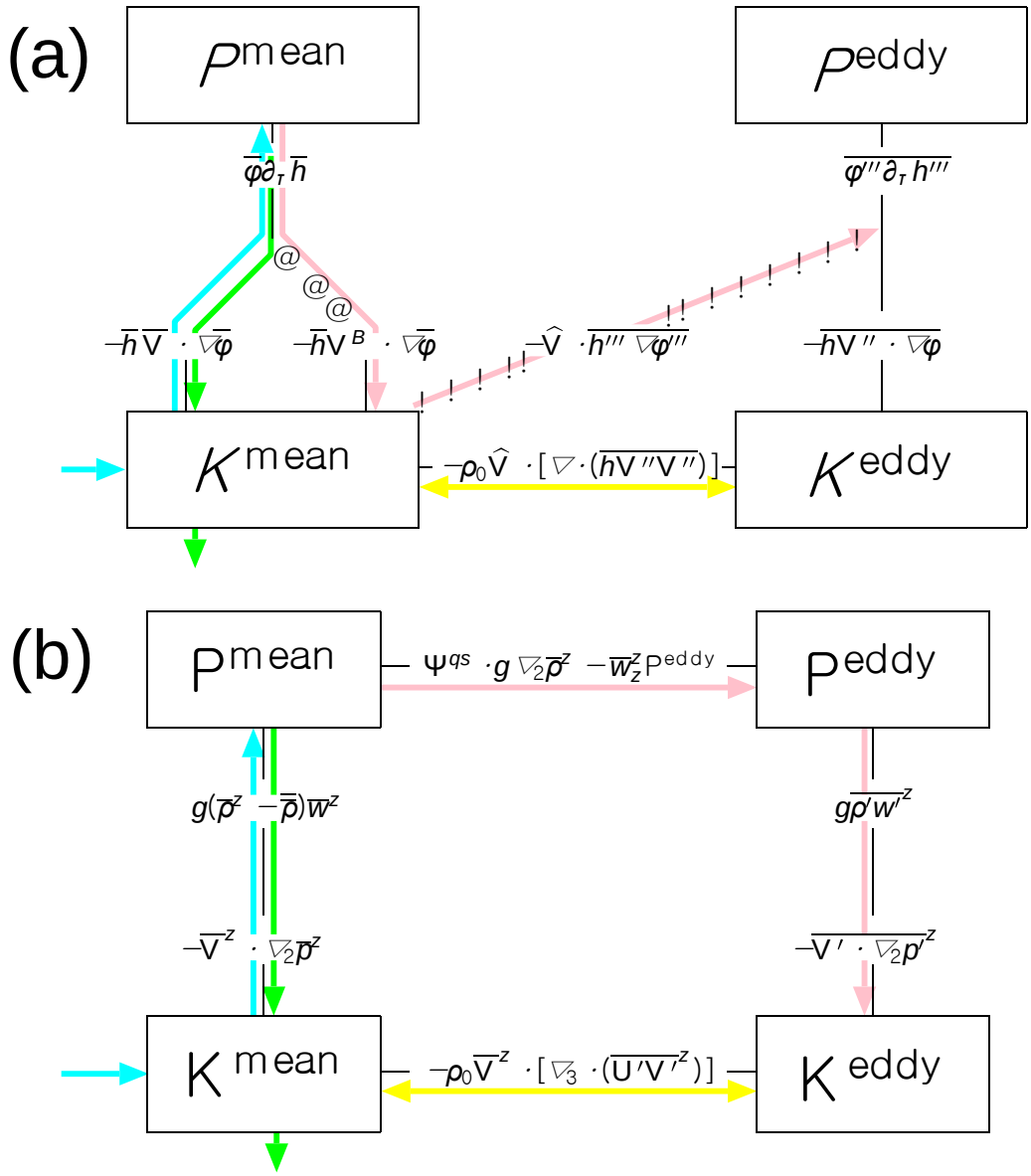

Figure 1. A four-box energy diagram based on energy equations averaged in (a) density-coordinates and (b) z -coordinates. Note rÁ = r2p (the lateral gradient of the MP in density-coordinates is identical to the horizontal gradient of hydrostatic pressure in z -coordinates). The cyan arrows represent the energy conversion route associated with the wind-induced Ekman flow. The green arrows represent the energy conversion route associated with the continental-drag Ekman flow. The pink arrows represent the main energy conversion route associated with eddies in baroclinic instability. The yellow arrows represent the energy conversion route associated with the Reynolds stress.

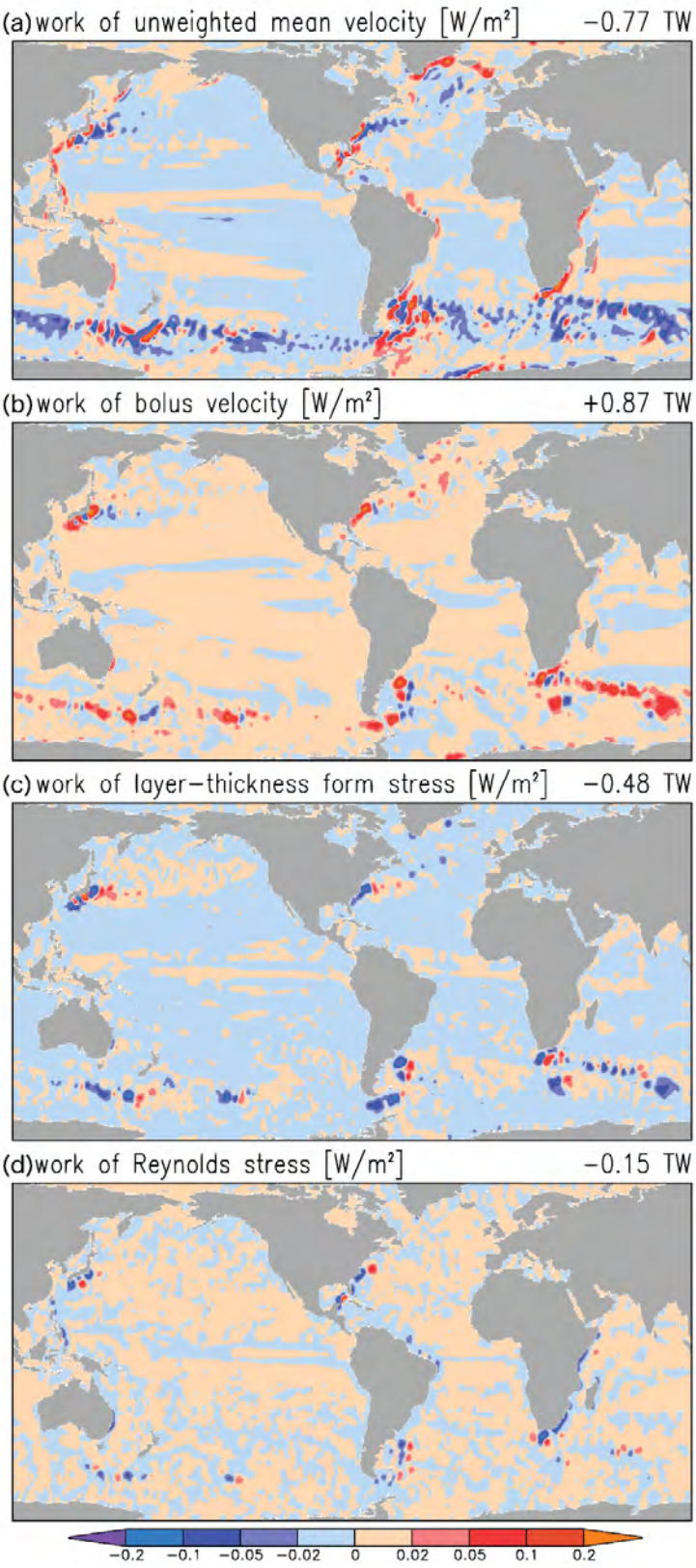

Figure 2. The depth-integral of the energy conversion rates [W/ m2] associated with (a) the unweighted mean velocity $-\overline{h}\overline{\mathbf{V}}\cdot\nabla\overline{\phi}$, representing the effect of the Ekman flow, (b) the bolus velocity $-\overline{h}\mathbf{V}^{B}\cdot\nabla\overline{\phi}$, representing the effect of the eddy-induced overturning circulation, (c) the layer-thickness form stress $-\hat{\mathbf{V}}\cdot\overline{h'''\nabla\phi'''}$, representing the effect of the vertical redistribution of momentum by eddies, and (d) the Reynolds stress $-\rho_0\hat{\mathbf{V}}\cdot[\nabla\cdot(\overline{h\mathbf{V}''\mathbf{V}''})]$, representing the effect of thelateral redistribution of momentum by eddies. The sign is referenced to the budget of the mean kinetic energy. The estimate is based on the 3-day snapshots of the OFES hindcast simulation with application of a four-year mean in density coordinates.

Submesoscale dynamics and transport properties in the Gulf of Mexico

Annalisa Bracco and Yisen Zhong

School of Earth and Atmospheric Sciences Georgia Institute of Technology, Atlanta, GA, USA
E-mail: abracco@gatech.edu

We analyze a suite of numerical simulations of the Gulf of Mexico that resolvethe submesoscale dynamics in northwestern portion of the basin. The runs are obtained using ROMS and exploiting its nesting capabilities. The horizontal resolution reaches 1km.

We present both Eulerian and Lagrangian passive tracer experiments; our focusis on the role that submesoscale dynamics play in the transport and mixing throughout the water column, above and below the mixed layer.

The domain of interest is populated by large Loop Current Eddies with typicaldiameter of 200 km, surrounded by smaller vortices (Figure 1), while large scale frontal structure are absent. By increasing the model horizontal resolution, the number and strength of submesoscale eddies and vorticity filaments in the mixed layer increase dramatically, and with them the vertical velocities. Increased vertical velocities for increasing resolution are found also inside the eddies, both large and small, and at their peripheries. Those high velocities are not limited to the surface, but are found at all depths. Horizontal velocities, on the contrary, are comparable.

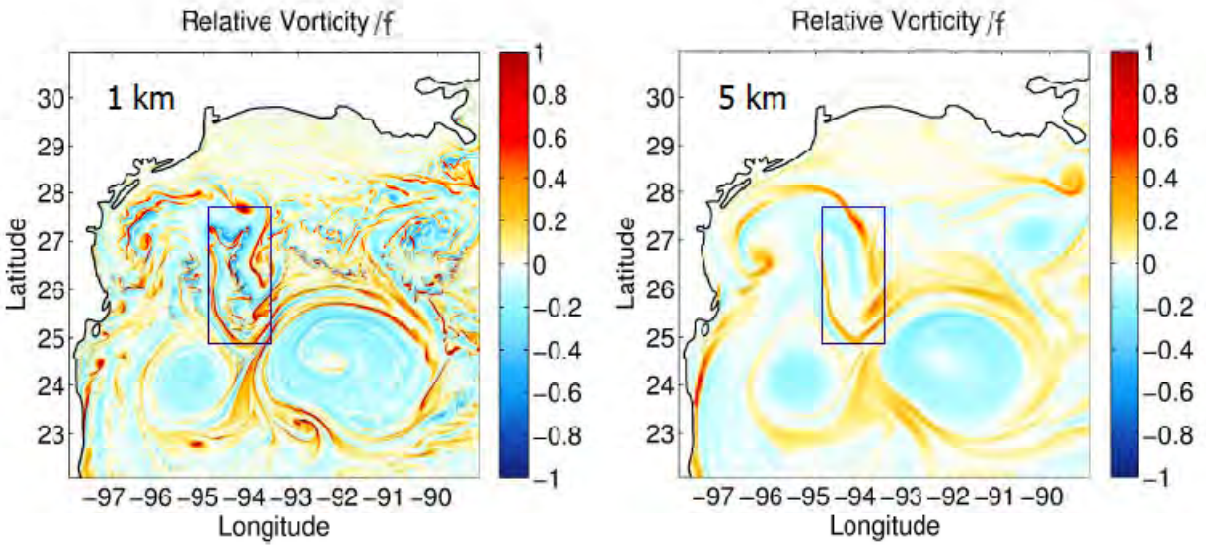

Figure 1. Snapshots of surface relative vorticity scaled by the Coriolis parameter f on April 21, 2005. (left) 1 km nested run and (right) 5 km parent grid. The boxes indicate where Lagrangian particles are deployed.

Lagrangian isobaric tracers are deployed close to the surface and at 100 m, and three dimensional, neutrally buoyant particles are released close to the surface, at the base of the mixed layer and at 100 m. Passive tracers are released at 5, 50 and 100 m in the box indicated in Figure 1 and in the core of the largest Loop Current eddy.

The horizontal dispersion curves for all Lagrangian deployments are independent of model resolution. The averaged pathways followed by the modeled tracers are comparable, and are dictated by the position and motion of the mesoscale structures with the Loop Current eddies stirring the tracers around their periphery. Close to the ocean surface, however, the strong divergence and convergence zones generated by ageostrophic processes in the submesoscale range - and resolved only in the simulation at higher resolution - are responsible for the creation of areas where the floating material accumulates. Floating particles concentrate in convergence regions in patterns comparable to the ones observed in the Gulf through the satellite images of *Sargassum*.

Vertical dispersion curves, on the other hand, depend on the model resolution and transport increases by several folds for increasing resolution at all depths explored (Figure 2), with the largest differences found close to the surface. Those differences are linked to a significant increase in amplitude of the modeled vertical velocities for increasing horizontal resolution through the whole water column. In our simulations, the distributions of vertical velocity w do not change in shape, but are resolution dependent in their variance, and the representation of the energy content of w is affected by the horizontal resolution at all frequencies. Larger vertical velocities for increasing horizontal resolution are found not only in correspondence to (surface intensified) submesoscale vorticity filaments, submesoscale fronts and in straining regions at the edge of the eddies, but also inside the eddies. Indeed, below the mixed layer the velocity field intensifies particularly inside the Loop Current eddies. Here the instantaneous values of the modeled w can reach several tens of m/day (up to 80 m/day). Those high values are not associated with significantly higher level of vertical diffusion (numerical and due to vertical mixing parameterization), but to different transport processes. Even higher values have been found in moored ADCP measurements in correspondence with the passage of Loop Current Eddies in the Gulf of Mexico.

We conclude that submesoscales processes play a fundamental role in driving vertical transport in eddy dominated flows, both within and below the mixed layer, for times comparable to the Eulerian time scale.

Acknowledgment

This work was supported by a grant (in part) from BP/the Gulf of Mexico Research Initiative to support consortium research entitled “Ecosystem Impacts of Oil and Gas Inputs to the Gulf (ECOGIG)” administered by the University of Mississippi, GRIID: R1.x132.141:0001 and by the National Science Foundation (OCE-0928495).

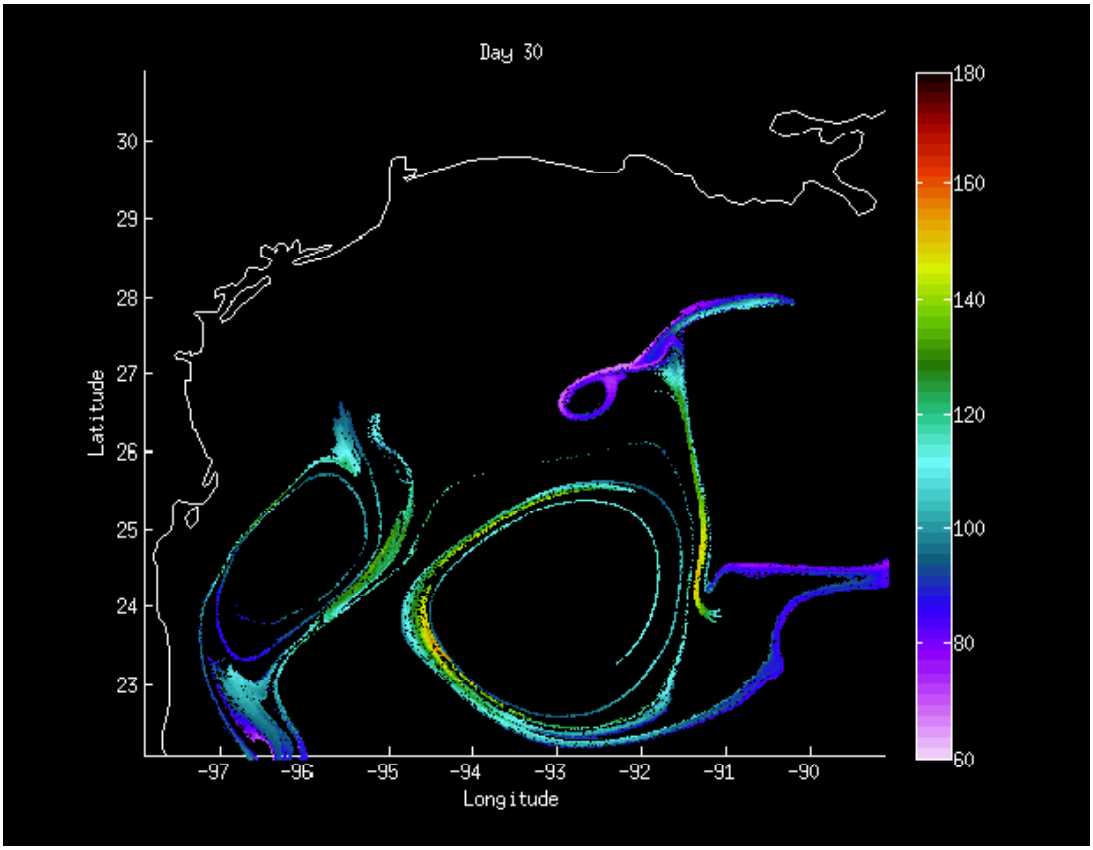

Figure 2. Vertical distribution of 3-D particles 30 days after deployment. The color of the particles indicates their depth (Unit: m). (Top) and (bottom): Tracers initially released at 100 m in the 1 km and 5 km horizontal resolution runs, respectively.

Seasonality of submesoscale activity around the Kuroshio Extension in a high-resolution simulation

Hideharu Sasaki[1], Patrice Klein[2], Bo Qiu[3], and Yoshikazu Sasai[4]

[1]Earth Simulator Center, JAMSTEC, Yokohama, Japan
[2]Laboratoire de Physique des Oceans, Ifremer-CNRS-UBO-IRD, 29280, Plouzané, France
[3]Department of Oceanography, University of Hawaii at Manoa, Hawaii, USA
[4]Research Institute for Global Change, JAMSTEC, Yokohama, Japan
E-mail: sasaki@jamstec.go.jp

1. Introduction

Ocean color and sea surface temperature fields observed by satellite exhibit not only mesoscale (O(100km)) structures but also smaller scales (submesoscales down to O(10km)) (e.g. Lévy et al. 2012). Non-negligible contributions of the submesoscales to vertical transports and impact on large-scale ocean properties via nonlinear interactions were revealed by recent studies (Capet et al. 2008; Klein et al. 2008; Lévy et al. 2010). However, spatial distributions of submesoscales and their temporal variations with seasonal to interannual time scale have not been observed yet in the real ocean.

Recently, Mensa et al. (2013) studied seasonality of submesoscale features in the Gulf Stream region in a realistic simulation. The occurrence of submesoscales appears to be controlled by the mixed layer (ML) depth. The mixed layer instabilities (MLIs: Stone, 1966; Nakamura, 1988; Haines and Marshall, 1998; Boccaletti et al. 2007) is one possible mechanism to leading vigorous submesoscales in winter, mostly due to deepening of the ML and increased available potential energy. The similar seasonality of submesoscale activity in the Kuroshio Extension region has been demonstrated by our realistic high-resolution simulation, which encourages us to observe its characteristics. The aim of this study is on the specific features in energetic and calm submesoscales around the Kuroshio Extension in winter and summer, respectively. Furthermore, what dynamics contributes to turbulent flow with energetic submesoscales within the ML is discussed.

2. North Pacific high-resolution simulation

In this study, we analyze outputs from a high-resolution (1/30˚ in the horizontal and 100 vertical levels) hindcast simulation of the North Pacific (100˚E–70˚W, 20˚S–66˚N) using the Ocean General Circulation Model for the Earth Simulator (OFES; Masumoto et al. 2004; Komori et al 2005) (see in Sasaki and Klein, 2012). The model is forced by surface wind stress and heat flux estimated from 6–hourly Japanese 25-year Reanalysis (JRA-25 ; Onogi et al., 2007). As the initial state, the output on 1 January 2000 from a 1/10˚ hindcast simulation starting from 1979 is used. The simulation has been integrated for 3 years from 2000 to 2002 (longer integration is in progress).

3. Results

The realistic simulation of the North Pacific highlights the seasonality of submesoscale activity. Oceanic structures of submesoscale (≈ 10 km) eddy and elongated filament around the Kuroshio Extension and subtropical countercurrent are more ubiquitous in late winter than during other seasons (Fig. 1). In this study, their seasonality in the box region of 150–160°E and 25–45°N around the Kuroshio Extension has been analyzed.

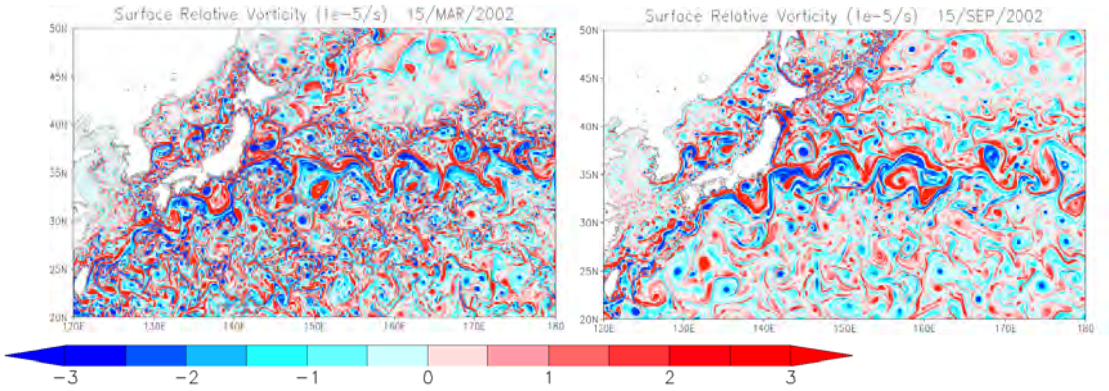

Figure 1. Surface relative vorticity (1e-5 s^{-1}) on (left) 15 March and 15 September in 2002.

The time series of the rms values of the surface relative vorticity shows that its magnitude is large in late winter and small in late summer (black line in Fig. 2a). In contrast, the seasonality of the rms values of SSH is unclear (blue line in Fig. 2a). This difference highlights significant seasonal variations of the submesoscale activity but not of the mesoscale activity. This seasonality of submesoscale activity is also examined by the time series of the total length of the isoline with zero relative vorticity (red line in Fig. 2a). The time evolution of the relative vorticity is mostly in phase with that of the ML depth (red line in Fig. 2b), although the ML depth suddenly becomes thin in spring not observed for the relative vorticity. This suggests that the seasonality of submesoscale activity is related to the ML dynamics that should be different in winter and summer.

The time series of the rms values of vertical motions within the ML (black line in Fig.2) exhibits strong seasonal variations, which correlates well with that of the ML depth (correlation is 0.973). The vertical motions are large (rms value > 8 m day^{-1}) in winter when ML is thick (> 100 m) and their amplitude suddenly decays at the beginning of April in the both years, in phase with the strong decay of the ML depth. What is interesting to note is that vertical motions below the ML, at 300 m and 500 m depths (blue and green line in Fig.2b) also exhibit similar seasonal variations, although with not so large amplitude and with much smoother decay during the spring compared to within the ML. Their variances are more in phase with that of the relative vorticity (Fig. 2a). These differences between the time series of vertical motions within and below the ML appear to confirm that the seasonal variation of submesoscales should be related to the ML dynamics, but also that this seasonal variation has a non negligible signature at depth.

4. Discussions

The emergence of a significant submesoscale activity in winter appears to occur principally within the ML. The most plausible explanation that can be invoked is the development of the

MLIs corresponding to small-scale baroclinic instability within the ML. To test the hypothesis, we have estimated the length scales of the most ML unstable waves by using the expression given by Nakamura (1988) (his equation (26)) and previously derived by Stone (1966). The resulting length scale averaged in the box region in March is 23.7 km. This scale is close to the small scales where the relative vorticity spectrum is still flat (≈ 30 km) (not shown). This flat spectrum down to this scale suggests an inverse kinetic energy cascade feed up by MLIs (Fox-Kemper et al., 2008). One further evidence is provided by the characteristics of the vertical motions within and below the ML. Scales associated with the spectral peak of the vertical motions within the ML are close to 25 km in March (now shown), which is similar to the MLIs scale. In September on the other hand, the length scale related to the MLIs is 14.2 km. Dynamical impact of such small-scale MLIs in summer appears negligible since results indicate a weak submesoscale activity during this period. However, these results have to be confirmed by using simulations with finer horizontal resolution, since the resolution of our simulation (1/30° ≈ 3km) does not seem to be high enough to resolve the MLI scale in summer.

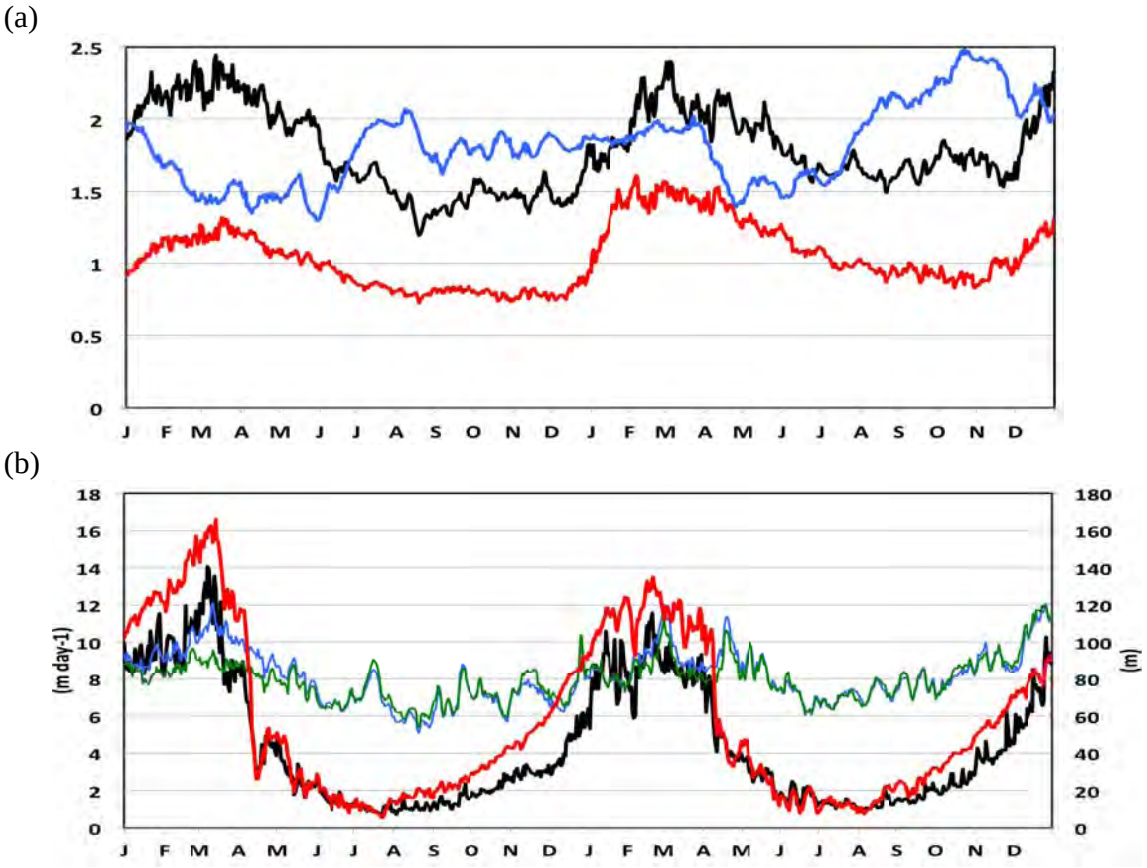

Figure 2. Time series in 2001 and 2002 in the box region of 150-160°E and 25-45°N. (a) Relative vorticity rms (black line, 1e-5 s^{-1}), contour line length of zero relative vorticity (red line, 1e8 m), and SSH rms (blue line, 1e-1 m); (b) vertical velocity rms (m day^{-1}) in the mixed layer (black line), at 303m (blue line) and 500 m (green line) depth and mean mixed layer depth (red line, m).

Other interesting characteristics concern the relationship of the ML vertical motions with the Laplacian of density in winter. Actually the daily mean patterns of the vertical motions appear to well match those of the density Laplacian (Fig. 3). A correlation between these two quantities in the box region is about 0.4, which is quite good since these quantities are small-scale. This means that, during winter, the ageostrophic dynamics very likely triggered by the MLIs but is also strongly constrained by the vertical mixing as expressed by the Garrett and Loder (1982) relationship between vertical motions and density Laplacian. This characteristic is not observed in summer.

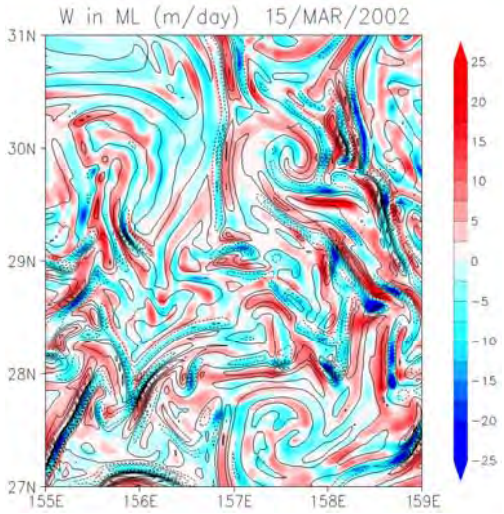

Figure 3. Upward vertical velocity (color, m day-1) and laplacian of potential density (contour, σ_θ m-2) averaged in mixed layer. Contour intervals are 2e-10 σ_θ m^{-2} and dotted contour curves indicate negative value.

5. Conclusions

A high-resolution realistic simulation exhibits seasonality of submesoscale characteristics in the Kuroshio Extension region, energetic in late winter and calm in late summer. When the submesoscale is energetic, ML thickness is large and vertical motions with submesoscale in horizontal in the ML are strong. The time evolution of submesoscale corresponding to relative vorticity rms does not decay rapidly in the spring compared to those of the ML depth and vertical motions within the ML. Not only the MLI but also vertical mixing within the ML and SI possibly contribute those seasonal vatiations.

The vertical motions in the ML partially penetrate through the bottom, which is expected to influence the ecosystem (Sasai et al. in preparation). Future satellite missions such as the SWOT (Fu and Ferrari 2008) and COMPIRA are expected to observe the submesoscale characteristics and its seasonality in the real ocean. Realistic simulations with an even higher resolution should also lead to better understanding of dynamics in the oceanic fields with energetic submesoscales.

Acknowledges

The simulation was done on the Earth Simulator. This work is partially supported by MEXT/JST KAKENHI (HS and YZ: 25400473, HS: 23340139, 22106006).

Biological Relevance of Submesoscale Dynamics in the highly stratified, Oligotrophic Ocean

Paulo H. R. Calil

Instituto de Oceanografia, Universidade Federal do Rio Grande, Brasil
E-mail: paulo.calil@furg.br

The permanently stratified, oligotrophic waters of the Central North Pacific Ocean around Hawaii pose an intriguing biogeochemical puzzle. Despite its low biomass, high productivity and a rich diversity of micro-organisms are observed in the region (Karl et. al 2008). New production, which ultimately constrain global export production in the ocean, depends on processes that supply in organic nutrients to the sunlit layer either directly via supply from waters within the nitracline or, indirectly, via phosphate supply for nitrogen fixing organisms that are commonly observed in the region [Church et al., 2009; Fong et al., 2008]. This intricate system is the result of the interaction between the physical and biogeochemical environments and their multi-scale spatial and seasonal variations. Therefore, the explanation of observed patterns most likely involve a combination of multiple factors rather than a single process. This study tries to shed light into one of these factors, namely the importance of submesoscale dynamics in supplying new nutrients into the upper ocean in a stratifed, oligotrophic environment.

Observational evidence of the impact of various physical mechanisms on nutrient dynamics and food-web structure in this region is overwhelming. Rossby waves [Nicholson et al., 2008; Sakamoto et al., 2004] and mesoscale eddies [Church et al., 2009; Fong et al., 2008; Letelier et al., 2000; Lukas and Santiago-Mandujano, 2001] have been shown to impact water properties and ecosystem structure at Station ALOHA. These processes are concomitant and constantly interact with one another which may lead to the formation of episodic fronts. These are usually associated with the edges of mesoscale features, whose width is O(10 km). Recent studies have associated the development and intensication of filamentous patches with high chlorophyll concentrations at the edges of anticyclonic to episodic frontal processes [Calil and Richards, 2010].

Because the waters in the upper euphotic zone (0-50 m) are extremely nutrient-poor and stratification just below the mixed layer is large during most of the year, physical processes will impact the upper and lower (50-150 m) euphotic zone differently. The effect of heaving isopycnals due to the passage of Rossby waves ([Nicholson et al., 2008; Sakamoto et al., 2004]) or mesoscale eddies ([Letelier et al., 2000; Lukas and Santiago-Mandujano, 2001]) would be confined to the lower euphotic zone. When light is not limiting, such motions would stimulate planktonic growth due to the delivery of nutrients. In the upper euphotic zone, more subject to seasonal surface forcing and relatively isolated from the deeper layers by stratification, there is evidence that nitrogen fixation plays an important role in the nutrient budgets in this region. In this layer, physical processes that provide ideal conditions for diazotrophs [e.g. stratified, warm waters) would, therefore, impact their growth favorably. Such conditions are usually met, for

example, in the core of anticyclonic eddies. This is why several studies have correlated their presence with diazotrophs [Church et al., 2009; Fong et al., 2008]. Nevertheless, diazotrophs are highly dependent on nutrients such as phosphate and iron which need to be somehow supplied to the upper euphotic zone. While the speci_c mechanisms are still unclear, [Calil et al., 2011] argue, based on remotely-sensed measurements of ocean color, sea surface temperature and dust deposition as well as Lagrangian diagnostics, that episodic injections associated with frontal processes may also play a role. Such episodic injections can be either due to wind mixing events, large vertical velocities at ocean fronts or to the exchange between the mixed-layer and the upper thermocline, which would be able to extract higher nutrient concentrations from the top of cyclonic structures, for example, even though such structures do not extend all the way to the surface.

In this study we will focus on the ability of physical processes at different scales to supply new nutrients into the upper ocean from below the euphotic zone. We use a simple, nitrogen-based plankton model which allows for the separation of new and regenerated production. The simplicity of the model is justified on the basis of the nutrient supply mechanism in focus (i.e. injection from the nitracline) as well as the computational cost of a high-resolution biogeochemical model.

Brief Model and Experiments Descriptions

The biological model is a modified version of Fasham's classic nutrient-phytoplankton1 zooplankton-detritus (NPZD) model [Fasham et al., 1990] that has been adapted to hydrodynamic Regional Ocean Modeling System (ROMS) and has been successfully applied to different regions [Gruber et al., 2006; Kone et al., 2005]. The version of the biological model used in this study consists of eight compartments, with nitrate (NO_3) and ammonium (NH_4) representing the pool of inorganic nitrogen and small and large compartments for phytoplankton, zooplankton and detritus. Three model experiments, with the horizontal resolution increasing from 10, 3 to 1 km, are shown for the domain around the Hawaiian Islands.

Results

The climatology of the buoyancy frequency obtained from monthly salinity and temperature measurements at Station ALOHA (Fig. 1) shows weaker stratification in the winter months with the mixed layer depth (MLD)----estimated as the depth at which potential density is 0.125 kg ms^{-3} larger than surface values---reaching a maximum of nearly 120 m in January. Seasonal buoyancy forcing causes the water column to be less stratified during late winter and early spring. Mixing events driven by instability mechanisms (e.g. baroclinic and probably submesoscale), potentially important in structuring the pelagic ecosystem, are more frequent during this period [Letelier et al., 2000; Johnson et al., 2010]. The onset of stratification in late spring shallows the MLD and further isolates it from the permanent thermocline by creating a layer of strong stratification that lasts until November, when it starts being eroded by enhanced vertical mixing driven by the seasonal surface buoyancy loss.

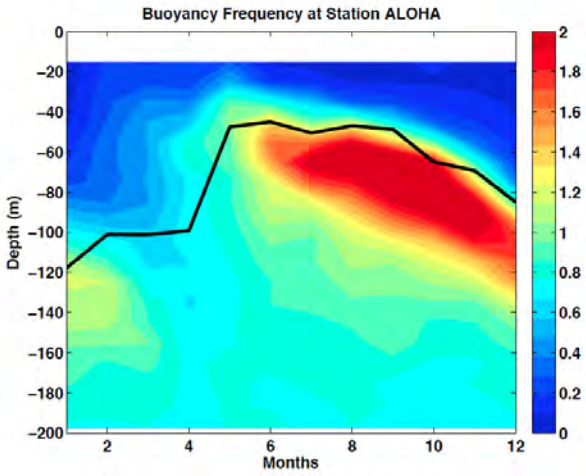

Figure 1. Climatological buoyancy frequency and MLD at Station ALOHA calculated from temperature and salinity measurements**.**

The 3-year average of the modeled buoyancy frequency at a subdomain encompassing the region of Station ALOHA (22º - 24ºN and 158.85º - 155ºW) in the different model runs is shown in Fig. 2. Also plotted are the average planetary layer depth (hBL), as calculated by the k-profile parameterization scheme in ROMS.

The overall characteristics of all runs are similar with regards to the onset of stratifica1 tion as well as planetary boundary layer depths. They compare well with the observations from monthly cruises at Station ALOHA (Fig. 1), although the high stratification layer in the model runs is shallower. The seasonal evolution of the buoyancy frequency (Fig. 2, right) is similar for the 3 runs, with the top of the high stratification layer at about 40 m depth in spring, a maximum in stratification in the summertime at about 60 m depth and the beginning of the destratification in the fall. Such evolution, along with the seasonal evolution of the planetary boundary layer, are consistent with observational studies in a region to the northeast of Station ALOHA [Cole et al., 2010].

The modeled vertical velocity variance (Fig. 3), taken from profiles of 2-day averages at the location of Station ALOHA, increases substantially with increased resolution. Values are larger just below 50 m depth, approximately the average boundary layer depth. The seasonal evolution of the vertical velocity variance shows that in all runs it is larger, as expected, in the winter due to enhanced vertical mixing. The magnitude increases with resolution with peak values just below hBL. As resolution is increased, vertical velocity variance increases in other seasons as well, particularly during fall and spring. In the summertime, it is much smaller than in other seasons for all runs. A small peak is discernible in HI1km during summertime at approximately 40 m depth. Differences in mean vertical velocity values are not very large in the different runs, a result consistent with recent modeling studies [Levy et al., 2011]. It is noteworthy that the increased variance of the vertical velocity associated with the high resolution runs does not a_ect vertical mixing processes within and below the mixed layer. This is desirable, as excess vertical mixing would lead to substantial problems in the heat budget within the upper ocean [Jenkins and Doney, 2003]. In general, the physical processes are relatively similar in all runs, even though signature of submesoscale processes is evident in the relative vorticiy (not shown) and vertical velocity

fields.

Biophysical Dynamics

The main difference between the model runs in terms of biological standing stocks is the emergence of the large phytoplanktonic species at high resolutions as seen in the time series of 2-day averages in Fig. 3. This point-wise view, as opposed to the box-averaged one, is useful for gaining insight into the different temporal and spatial variability in the different runs, as box-averages will smear out such variability.

Large phytoplankton, whose values in the 10 km run are very low, occupy a significant portion of the lower euphotic zone (between 50 and 150 m) from late spring to early fall in HI3km and HI1km. In the context of our model simulations, such large concentrations can only arise as a consequence of larger nitrate inputs at the top of the nitracline, just below the high stratification layer. Episodic, vertical nitrate injections at 100 m depth are clearly more frequent in HI3km and HI1km than in HI10km, even though there are no big differences in terms of isopycnal displacements---with the 24.5 isopycnal relatively stable around 100 m depth in all three runs, the depth at which large phytoplankton concentrations are centered---or nitracline depth. Vertical excursions of isolines of nitrate are largest in HI3km. In HI1km they are not intense as in HI3km, but they are more frequent than in HI10km. Interestingly, even with the nitracline slightly deeper in HI1km, large phytoplankton still emerges, which suggests that the episodic vertical excursions of the isopycnals increase the exchange between the nutrient-rich from below the mixed-layer and surface, nutrient depleted waters. These values arise during late spring and summer due to the combination of increased nutrient supply in the high-resolution runs and light availability. In contrast, the only instances in which large phytoplankton arises in HI10km are two large injections between days 360 and 400 (Fig. 3). The fact that episodic injections are not as intense or frequent in HI10km could explain why large phytoplankton concentrations are very low in this run except for the strong late winter event at around day 400 (Fig. 3).

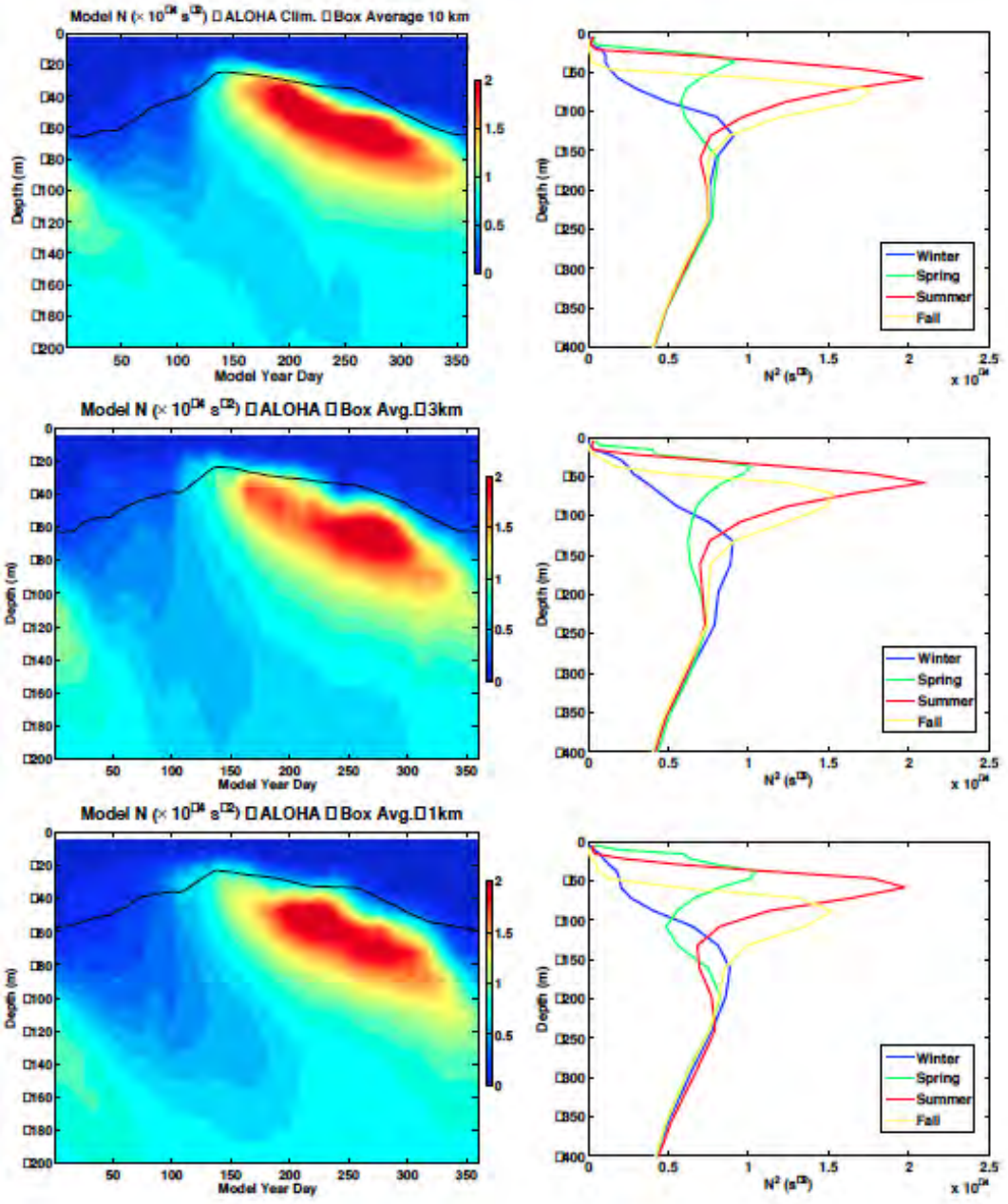

Figure 2. Model 3-year average of the buoyancy frequency at a subdomain around Station ALOHA. (left) and seasonal averages of the respective vertical profiles (right). HI10km (top), HI3km (middle) and HI1km (bottom).

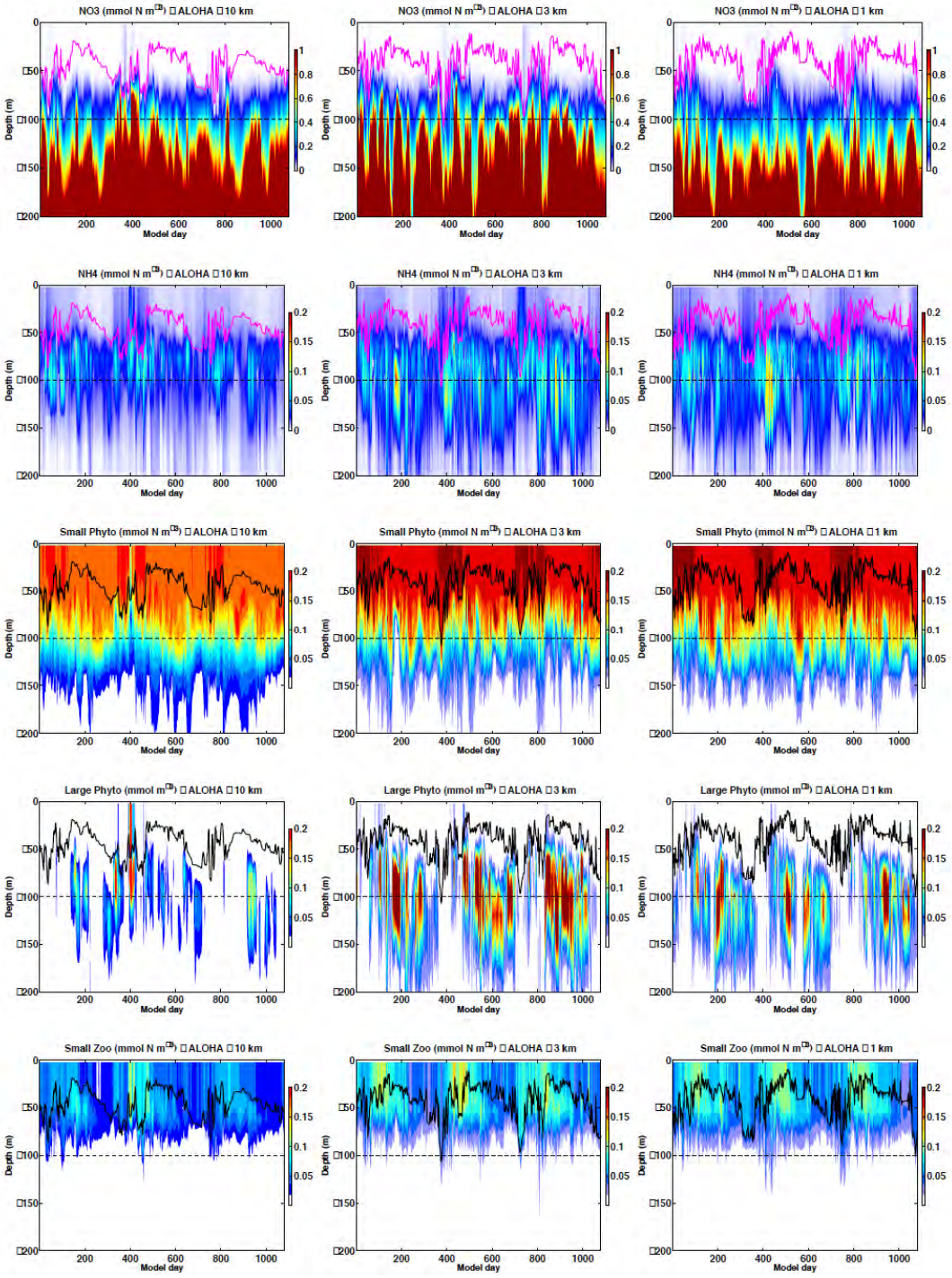

Figure 3. Modeled vertical profiles at the location of Station ALOHA for various biological variables. HI10km (left column), HI3km (middle column), HI1km (right column).

Conclusions

In this study we have used a plankton model embedded into a hydrodynamical model at8 different horizontal resolutions in order to estimate the effect of submesoscale processes on the biological rates and standing stocks in the oligotrophic ocean around Hawaii. Despite the fact that this is a region of shallow mixed layers and relatively weak surface density gradients, where submesoscale e_ects are not necessarily predominant, interactions of the mesoscale eddy _eld with existing surface density gradients give rise to structures that are not captured without the adequate modeling|and, most likely, sampling|strategy.

Our results show that the upper ocean and mixed layer dynamics are not substantially affected with increased resolution. One difference that deserves further investigation is the enhanced subduction at higher resolutions, as waters with low stratification reach deeper in the water column after winter mixing. Mixed-layer depths and buoyancy frequency patterns are relatively similar. The biggest di_erence in terms of the physics is the substantial increase in vertical velocity variance at the base of the planetary boundary layer. This is a consequence of frontogenesis, the creation and intensification of density gradients caused by straining of the mesoscale eddy field.

The response of the biological model to increased resolution is not as straightforward as the general idea that increased resolution leads to increased production. Although there is a substantial increase in new production from HI10km to HI3km, further increasing the resolution causes a reduction in new production from late winter to early summer, even though values are consistently larger than in HI10km throughout the year. The 3-year average at the ALOHA subdomain shows that the nutricline is depressed in HI1km when compared to all other runs, which is possibly a consequence of the asymmetry in the vertical velocity at the submesoscale caused by surface frontogenesis which leads, on average, to enhanced downwelling. Such depression of the nitracline is consistent with results from a recent study that attributes it and the subsequent decrease in phytoplankton concentration at submesoscales to remote, long-term e_ects that balance the locally enhanced nutrient supply [Levy et al., 2011]. Despite the nitracline being deeper in HI1km than in HI10km, the strength of episodic events still allow larger phytoplankton to emerge. Such events select species with high growth rates that can make e_ective use of the episodic bursts of new nutrients, which is why subsurface blooms occur from spring to late summer in HI3km and HI1km, but not in HI10km. In HI10km, the slighly shallower nitracline and frequent mesoscale events arenot enough to drive such blooms. This study highlights the importance of episodic submesoscale motions for biological processes in the oligotrophic ocean around Hawaii and suggests that they should be taken into account when attempts to explain observed patterns in the biological fields are made.

Physical controls on biological production in the North Pacific sub-tropical gyre

Kelvin Richards and Francois Ascani

International Pacific Research Center and Department of Oceanography,
University of Hawaii at Mānoa, USA
E-mail: rkelvin@hwaii.edu

We will review the mechanisms by which physical processes impact biological production in the North Pacific sub-tropical gyre, in particular through the flux of nitrate. There has been much controversy over the relative roles of the vertical and lateral fluxes of nitrate in fueling primary production. The controversy is fueled by the difficulties in making good estimates of these fluxes. Recent interest has focused on the possible impact of sub-mesoscale flow features that can produce strong vertical motions as well as re-stratify the upper ocean through frontogenesis and mixed layer instabilities. To illustrate we show the vertical component of velocity and the near surface stratification from a snapshot of a high-resolution regional model around the islands of Hawai`i taken in January 2010. We see upward motions in excess of 20 m/day. There are associated large values in the relative vorticity (with $|\zeta/f|\sim 1$) and strong gradients in SST.

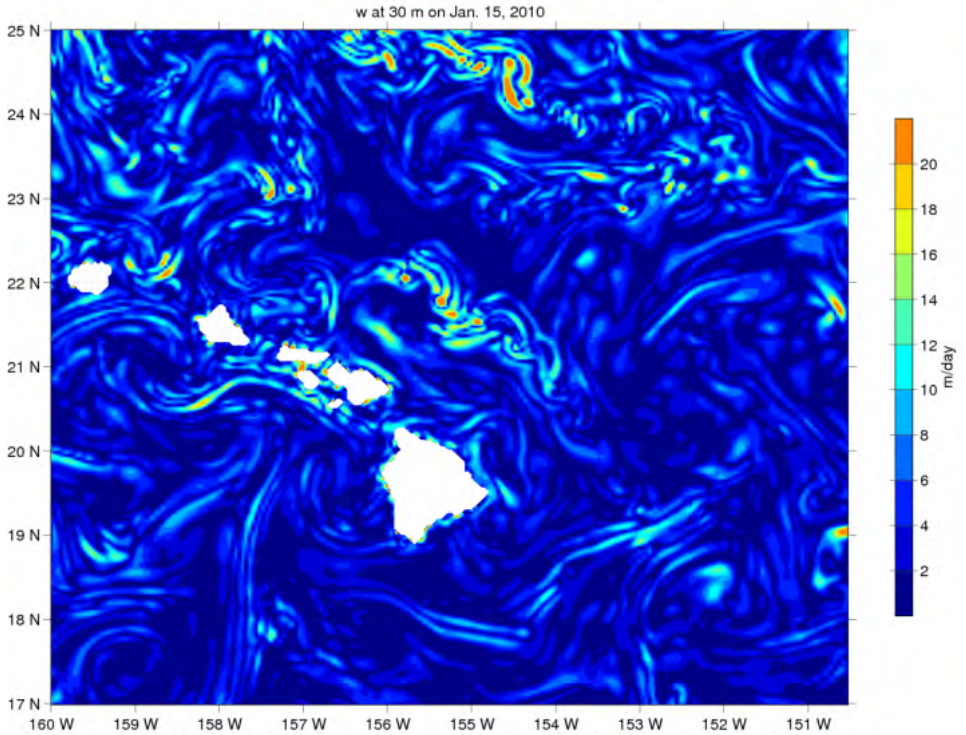

Figure 1. Vertical component of velocity, w, at 30m depth on January 15, 2010, taken from the results of a high-resolution regional ocean model.

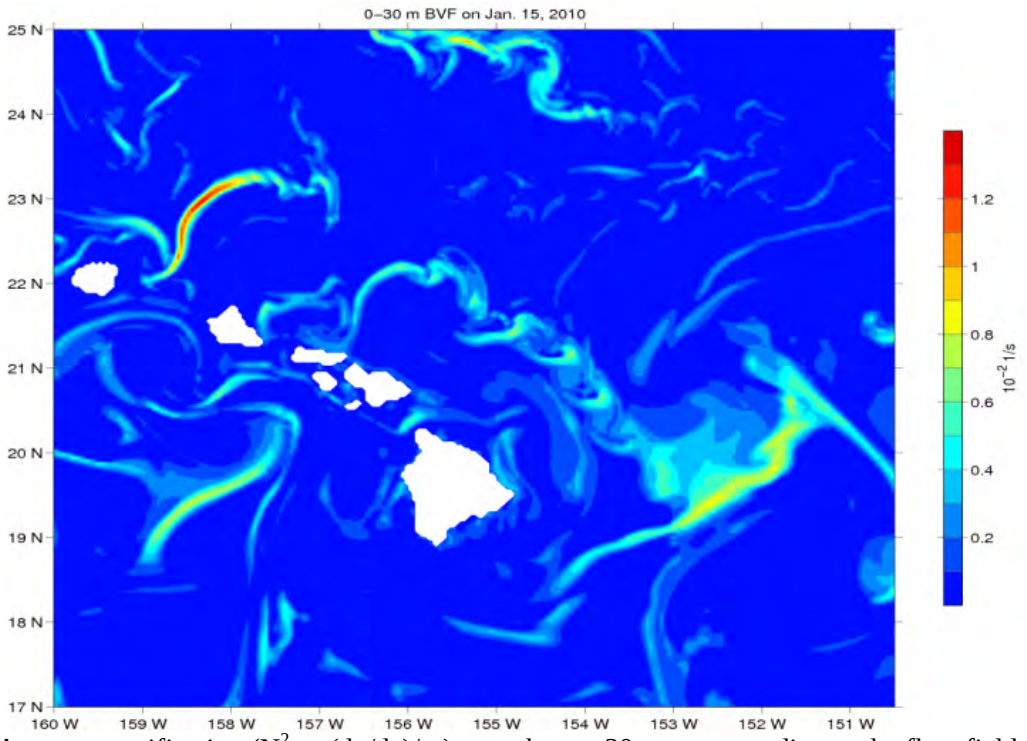

Figure 2. Average stratification ($N^2=-g(d\rho/dz)/\rho_0$) over the top 30m corresponding to the flow field shown in Figure 1.

Despite the winter conditions producing a relatively deep surface mixed layer sub-mesoscale processes have restratified a significant fraction of the ocean.

We find the strong vertical motions associated with the submesoscale frontal structures are confined to the surface mixed layer. In later winter/early spring the depth of mixed layer is close to that of the nutricline. Episodic high nitrate events, at this time of year, seen in data from floats with a nitrate sensor may well be caused by submesoscale activity. At other times the nutricline is well below the surface mixed layer. In addition we see a large seasonal variation in submesoscale activity with diminished activity in late spring early summer, suggesting little impact on biological production during this time of year.

So, what will happen under global warming? Attention has focused on a more stratified upper ocean reducing primary production. We speculate that sub-mesoscale activity will also be suppressed under warmer conditions with the potential of further reducing productivity. The degree to which this will happen will depend on the impact of sub-mesoscale activity under present conditions as well as future changes to that activity. Both will depend on local conditions. There is a need, therefore, to quantify the impact of sub-mesoscale activity on biological productivity for present day and future conditions on a region-by-region basis.

Effect of eddies in the Southern Ocean ventilation

Hajoon Song, John Marshall

Department of Earth, Atmospheric and Planetary Sciences
Massachusetts Institute of Technology, Cambridge, Massachusetts, USA
E-mail: hajsong@mit.edu

What are CFCs and why they are important?

Chlorofluorocarbons (CFCs) are anthropogenic gases and they were first introduced to the atmosphere in 1930s (Fig. 1). Since then, they have been absorbed by the ocean through air-sea gas exchanges and, as inert passive tracers, advected and diffused by ocean circulation. During the 1990s, CFCs concentrations in the global ocean were measured under the program called World Ocean Circulation Experiment (WOCE), the Joint Global Ocean Flux Study (JGOFS), and the Ocean Atmosphere Carbon Exchange Study (OACES), and the data were released as the Global Ocean Data Analysis Project (GLODAP). Since there were no CFCs prior to 1930s, the global map of CFCs distribution provides us better understanding of the ocean ventilation processes for anthropogenic gases that is one of the key steps for predicting future climate accurately.

The CFCs data also provides a great testbed for evaluating the ocean ventilation processes in the global ocean models. Comparisons between observed CFCs' concentrations and model simulations should reveal the model biases, which could be reflected in the analysis of simulation of other anthropogenic gases in the ocean model. Dutay et al. [2002] compare the ocean ventilation processes in 13 global ocean models using CFC-11 and show different ventilation processes not only between models but also parameterizations for unresolved sub-grid scale eddy activities. The differences between model are more obvious in the high latitudes such as the Southern Ocean, where Subantarctic Mode Water (SAMW) and Antarctic Bottom Water (AABW) are formed.

In this study, we evaluate the ventilation process in our global ocean model, MITgcm, with pCFC-11 observations from the GLODAP, and explore how the mesoscale eddies affects the ocean ventilation processes in the eddy-resolving regional ocean model over the Southern Ocean. ¶

Ventilation in the global ocean model

Tracers are advected by residual current, but global oceanic model cannot resolve that.)

In the Antarctic Circumpolar Current, passive tracers are carried by the residual circulation that arises from the balance between meridional Eulerian circulation and eddy-induced circulation *[Marshall and Radko, 2003]*. Thus, the ventilation processes cannot be accurately simulated withoug considering the circulation by mesoscale eddies. General global ocean models were limited to resolve eddies due to their coarse resolution. Instead, they often employ eddy parameterization of sub-grid eddy features. To take the effect of eddies into account, MITgcm was integrated with Gent and McWilliams eddy parameterization [Gent and McWilliams, 1990] and Redi isopycnal diffusion parameterization . These parameterization schemes estimate the eddy-induced advection and isopycnal diffusion based on the gradient of isopycnal scaled by

coefficients. Global ocean model whose horizontal resolution is roughly 1 degree was integrated for 97 years from 1911 to 2008, and the model results during 1990s were analyzed for this study.

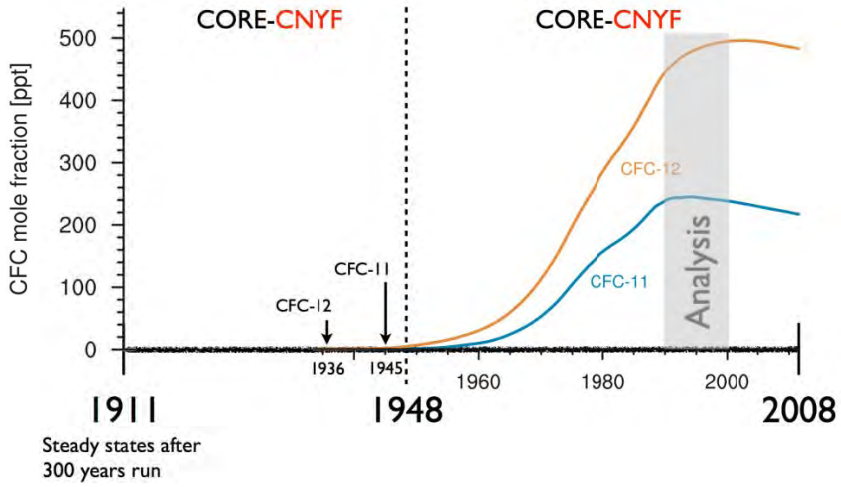

Figure 1. Atmospheric CFC-11 (blue) and CFC-12 (orange) concentration in 20th century. The global ocean model (MITgcm) was integrated for 97 years with two different surface forcing data sets : CORE-CNYF (no interannual variability) and CORE-CNYF (interannual variability). The model results in 1990s were analyzed and compared with GLODAP pCFC-11 whose measurements were made in 1990s.

The global ocean model simulates the pCFC-11 column inventory similar to the observations (Fig. 2). Regions with high pCFC-11 inventory are the North Atlantic and Southern Ocean where deep water forms. These areas are characterized with cold winter sea surface temperature and fast vertical mixing. Since the solubility of CFC-11 increases with decreasing temperature, these high latitude regions are characterized as high pCFC-11 concentration. Although the inventory of pCFC-11 in the model captures big spatial patterns in the observations, the model shows lower level of inventory, especially in the regions of high uptake. Lower level of pCFC-11 inventory in the North Atlantic Ocean indicates that the meridional overturning circulation is not strong enough to correctly represent the ocean ventilation. In the Southern Ocean, on the other hand, inaccurate parameterization of eddy-induced advection and isopycnal mixing is possible explanation of lower pCFC-11 inventory in the model.

.

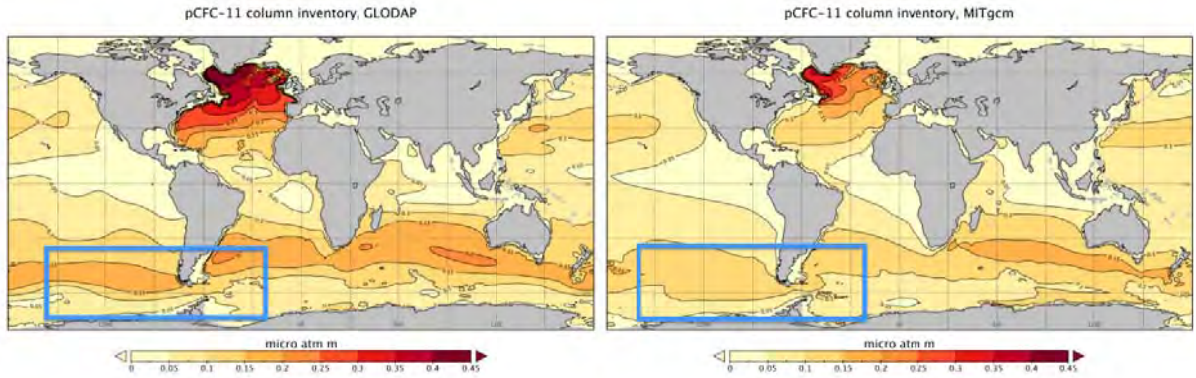

Figure 2. Column inventory of pCFC-11 in the observations (left) and MITgcm (right). Light blue square represent the regional model domain.

Ventilation in the eddy-resolving regional ocean model

In order to investigate the effect of eddies in the Southern Ocean ventilation, we set up a eddy-resolving regional model over the Southern Ocean (Fig. 2) with 0.25 degree horizontal resolution. The model was integrated for 5 years starting from 1990 and last three years were analyzed for this study.

Although the model domain covers 140 degree in zonal direction, this region is highly energetic area with eastward Antarctic Circumpolar Current, and it takes roughly 2 years for signals to go through from western to eastern open boundary. It indicates that here might be not enough time for eddies to be fully developed in the regional model. However, the eastern part of Drake passage shows improvement in simulating pCFC-11. In particular, the pCFC-11 inventory is significantly increased in the east of South America. This region is characterized with high eddy kinetic energy in both satellite observation and model simulations. Thus high eddy activities promotes more uptake of CFC-11.

More detailed analysis will come and be presented in the meeting.
(What is going to be analyzed)

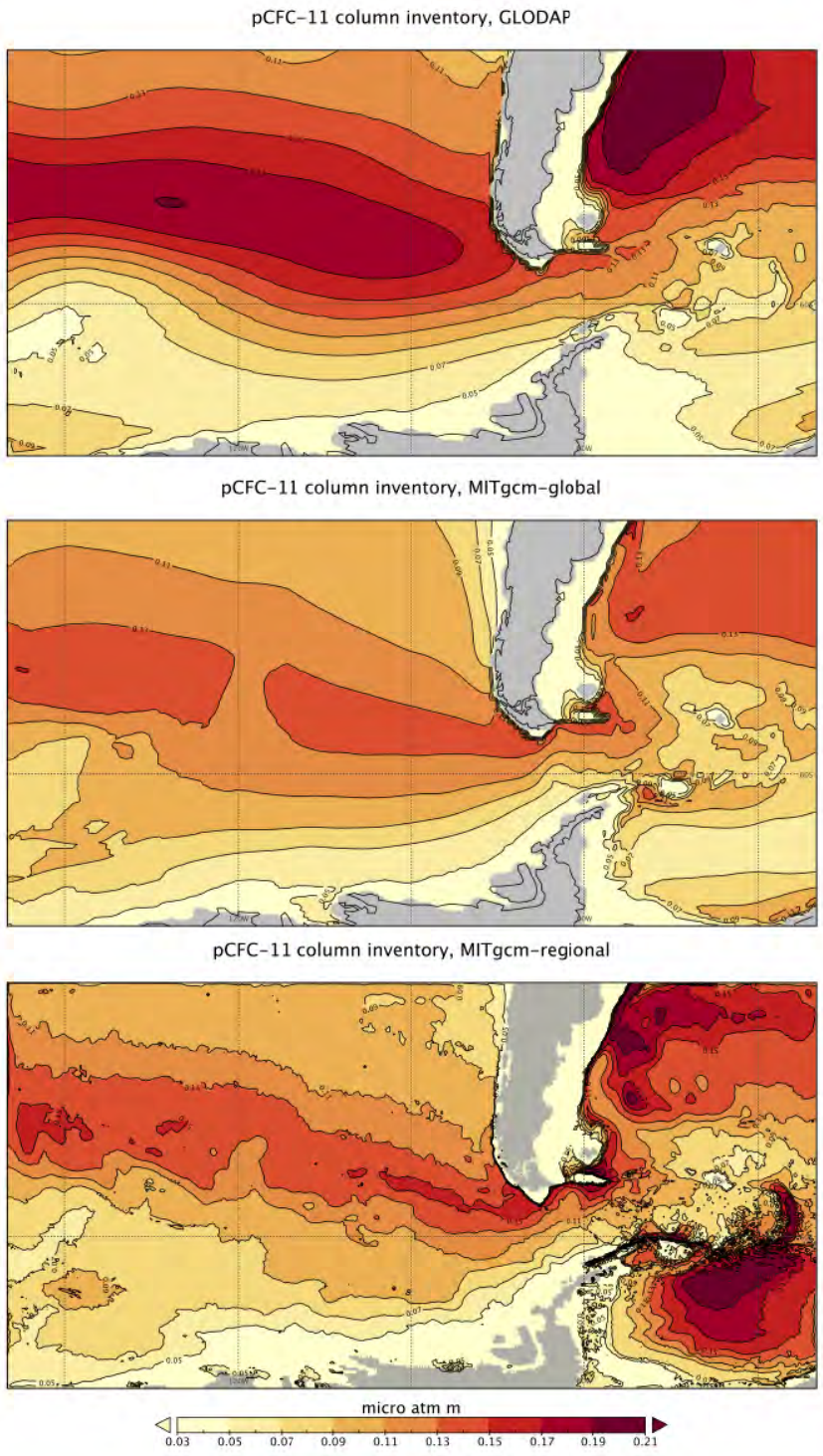
pCFC-11 column inventory, GLODAP
pCFC-11 column inventory, MITgcm-global
pCFC-11 column inventory, MITgcm-regional
micro atm m
0.03 0.05 0.07 0.09 0.11 0.13 0.15 0.17 0.19 0.21

Figure 3.

Bibliography

1. J. C. Dutay, J. L. Bullister, S. C. Doney, J. C. Orr, R. Najjar, K. Caldeira, J.-M. Campin, H. Drange, M. Follows, Y. Gao, N. Gruber, M. W. Hecht, A. Ishida, F. Joos, K. Lindsay, G. Madec, E. Maier-Reimer, J. C. Marshall, R. J. Matear, P. Monfray, A. Mouchet, G.-K. Plattner, J. Sarmiento, R. Schlitzer, R. Slater, I. J. Totterdell, M.-F. Weirig, Y. Yamanaka, A. Yool, (2002), Evaluation of ocean model ventilation with CFC-11: comparison of 13 global ocean models, *Ocean Modell., 4*, 89-120.
2. Gent, P. R., and J. C. McWilliams (1990), Isopycnal mixing in ocean circulation models, *J. Phys. Oceanogr., 20*, 150-155.
3. Marshall, J. C., and T. Radko (2003), Residual mean solutions for the Antarctic Circumpolar Current and its associated overturning circulation, J. *Phys. Oceanogr., 33*, 2341-2354.
4. Redi, M. H., Oceanic isopycnal mixing by coordinate rotation (1982), *J. Phys. Oceanogr., 12*, 1154-1158.

Eddy statistics in the East/Japan Sea based on satellite altimetric data and numerical model

Kyung-Jae Lee, Kyung-Il Chang

School of Earth Environmental Science, Seoul National University, Korea
E-mail: kichang@snu.ac.kr

1. Introduction

Ocean's mesoscale variability on spatial and temporal scales of about 50-500 km and 20-150 days (Wyrtki et al., 1976) is largely attributed to eddies of those scales (Chelton et al., 2007). Because the mesoscale eddies play an important role in transporting heat and extracting energy from the large-scale flow, it is crucial that climate models represent these processes correctly either through parameterization or resolving eddies explicitly (Bishop and Bryan, 2013). Current global ocean climate models do not resolve mesoscale eddies although some of them are eddy-permitting, but regional climate models can be eddy-resolving. However, the fidelity of high-resolution regional models needs to be evaluated whether or not they correctly represent important regional processes including eddy variability and eddy heat fluxes. Validation of the eddy-resolving models is not an easy task because of poor spatiotemporal resolutions of ocean observations, although some comparison has been successfully made (e.g., McClean et al., 2006). In the East/Japan Sea (EJS), meaoscale eddies cause intraseasonal variability of upper and deep currents on timescale of 2-60 days (Takematsu et al., 1999; Chang et al., 2002; Senjyu et al., 2005), triggers locally generated topographic Rossby waves (Kim et al., 2013), play an important role in marine ecosystem (e.g., Hyun et al., 2009). Although attempts have been made to understand the generation, kinematics, movement, and decay of eddies in the EJS (e.g., Gordon et al., 2002; Shin et al., 2005), spatio-temporal characteristics of the mesoscale eddies in the EJS are not fully described and understood.

This study applies automatic eddy detection algorithms to satellite altimetric data and results from an eddy-resolving numerical model to describe the eddy statistics in the EJS and to compare the data- and model-derived eddy statistics.

The numerical model results from 1998 to 2009 used in this study were provided by Prof. Naoki Hirose at Kyushu University. The numerical model is called the Research Institute for Applied Mechanics Ocean Model (RIAMOM) which is a three-dimensional, z-coordinate, primitive equation model with a free surface and with grid resolution of 1/12° in the horizontal and 36 levels in the vertical. The model assimilates the sea surface height based on the Kalman filtering. Details on the model configuration and parameterizations can be found in Hirose et al. (2007).

2. Automatic eddy detection algorithms

Two automatic eddy detection algorithms are applied to the long-term 1/4° gridded satellite altimeter data (SSH: sea surface height) to reveal the statistical characteristics of the mesoscale

eddy field in the EJS. The two algorithms used include the recently documented VG (Vector Geometry-based) algorithm based on the geometry of the current vectors (Nencioli et al., 2010), and the widely used WA (Winding-Angle) algorithm (Sadarjoen and Post, 2000). Compared to other algorithms, the advantage of the VG algorithm lies in its rapidity in detecting eddies, and higher (lower) success (excess) detection rate. On the other hand, the developer of the VG method did not recommend applying the algorithm to low resolution data such as gridded AVISO SSH data. Rather it is more suited to high-resolution data as it was originally applied to numerical model result with 1 km spatial resolution (Nencioli et al., 2010). In this study, the 1/4° SSH data is linearly interpolated onto the 1/32° grid size, and then geostrophic currents are calculated from the interpolated SSH field to apply the VG algorithm to the 1/32° interval current vectors. Among the detected eddies, those with diameter smaller than 1/4° are regarded as artificial eddies derived from the interpolation, and they are discarded in the analyses.

Result from the two algorithms are validated by comparing number of eddies from the two algorithms with those identified by the manual detection method from 100 SSH maps (Fig. 1). Both algorithms are satisfactory in terms of the success and failure rates. The VG algorithm shows slightly better performance with relatively higher success and lower failure rates as compared to those from the WA method. While, the WA algorithm is superior to the VG algorithm as it identifies more real eddies than the VG algorithm.

3. Spatial and temporal eddy statistics

Applying the two algorithms to 19 years of the SSH data from 1993 to 2011, the spatio-temporal variability of the mesoscale eddy field in the EJS is analyzed. Number and radius of eddies detected by the VG algorithm from weakly-basis SSH data range from 10 to 30, and from 0.2°~0.38°, respectively. Seasonal variation of eddy properties commonly identified from the two algorithms is characterized by the maximum number of eddies in spring (March~May) and minimum number in fall (September~November) (Fig. 2). On the other hand, the eddy radius is minimum in spring and maximum in fall and winter. The intensity of eddies also shows minimum in spring and maximum in fall.

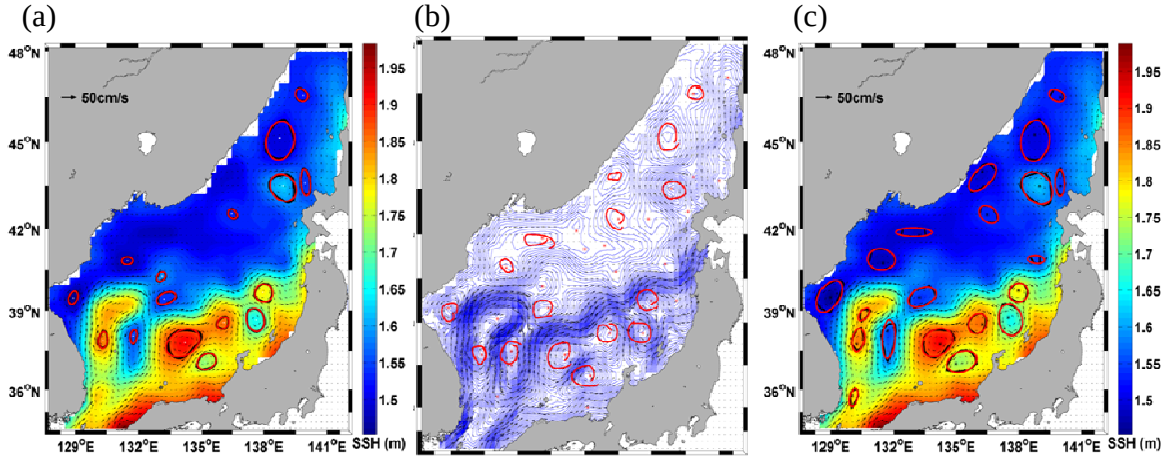

Figure 1. A snapshot of SSH (color) and geostrophic current distribution together with mesoscale eddies with diameter larger than 1/4° detected by (a) the VG algorithm, (b) manual detection, and (c) the WA algorithm.

The eddy intensity of an eddy is defined by the eddy kinetic energy divided by the area enclosed by an eddy following Chaigneau et al. (2008). In spite of an increase in eddy radius in fall, the eddy intensity is the maximum in fall indicating the strengthening of the swirl velocity in fall. The volume transport of the Tsushima Warm Current (TWC) entering the EJS is maximum in fall (e.g., Fukudome et al., 2011) suggesting the possible strengthening of eddies due to the increase in the volume transport of the TWC. The southern EJS is mainly affected by the TWC, and anticyclonic eddies are prevalent in the southern EJS. The eddy intensity of the anticyclonic eddies, however, becomes maximum in winter (nor shown). Instead, cyclonic eddies become the most intense in August and September.

Anticyclonic eddies are less in their numbers but they are larger and more intense as compared to those for cyclonic eddies (not shown). The probability of the emergence of eddies is higher west of 136°E, and appears to be associated with the bottom topography (Fig. 3). Anticyclonic (cyclonic) eddies are more prevalent in the southern (northern) EJS.

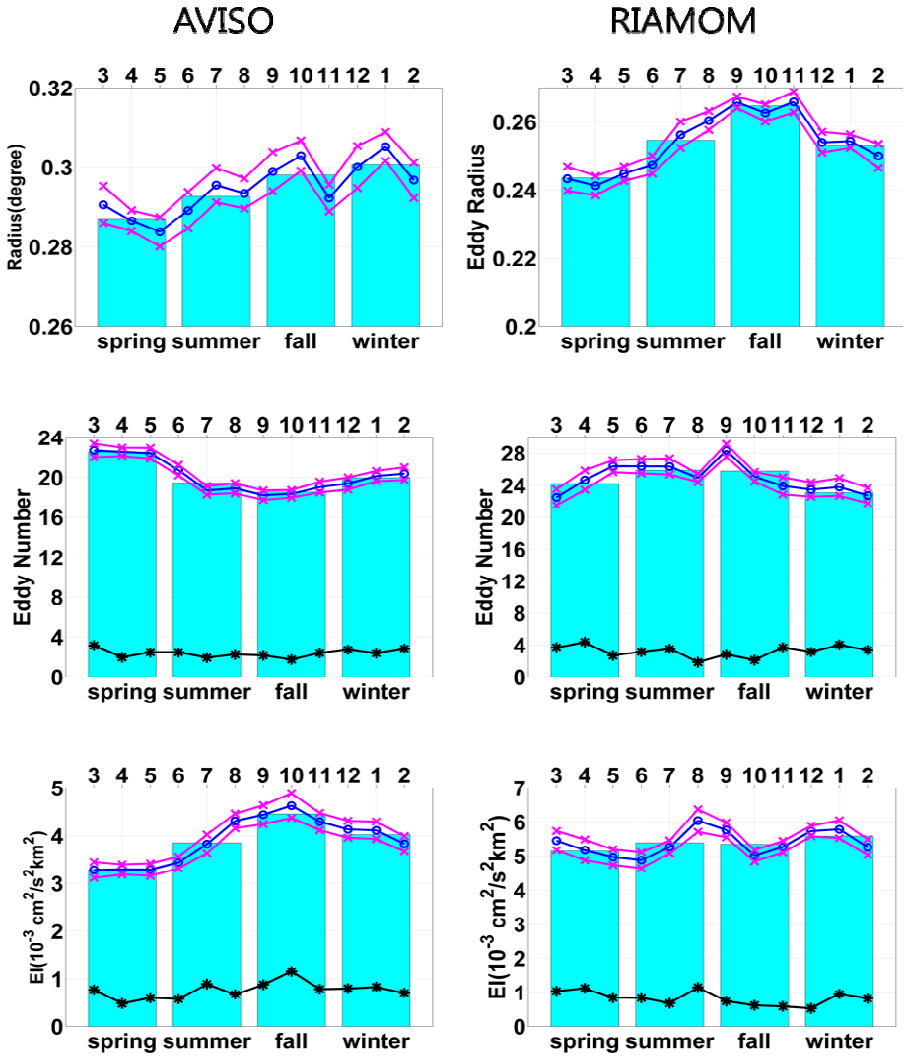

Figure 2. Seasonal variations of radius (upper panel) and number (middle panel) of eddies, and eddy intensity (lower panel) derived from satellite altimetric data (left panel) and the numerical model (right panel)

4. Eddy statistics in the numerical model

The VG algorithm is applied to the 10-year model results. As we interpolated the original 1/4° SSH field onto 1/32° resolution to apply the VG method, the model results are also interpolated onto 1/36° before applying the VG algorithm. Then the number, radius, and intensity of eddies are calculated to compare their seasonal variations with those from the SSH field (Fig. 2). Also the eddy probability maps based on the altimetric data and numerical model are also compared.

Model-produced eddies are smaller in size, larger in number, and more intense as compared to eddies detected from the altimetric data (Fig. 3). The seasonal variation of eddy properties based on the RIAMOM is characterized by the maximum size in fall (September ~November), the maximum number of eddies in summer and fall, especially in September, and the maximum eddy intensity in August and September. In general, the seasonal variation of the number of eddies and eddy intensity from the model is less pronounced as compared to those from the satellite data.

The eddy probability map based on the model results compares well with the map based on the satellite data. They show common regions of frequent eddy occurrence, the Ulleung Basin, western Yamato Basin, and the East Korean Bay. One difference is that while the eddy probability derived from the satellite data is high in the western Japan Basin, it is indistinct in the model-derived map. The high eddy probability region in the western Japan Basin corresponds to the dipole structure of wind stress curl in winter, and also the region of highest eddy kinetic energy for deep flow at 800 m (Park and Kim, 2013).

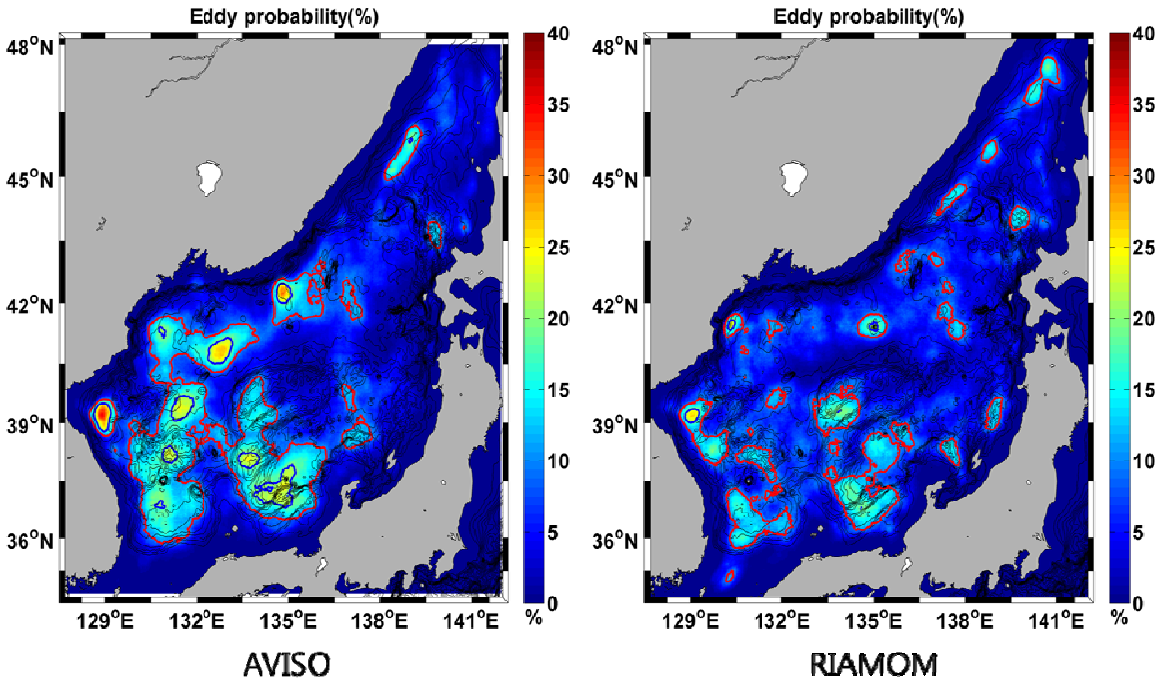

Figure 3. Eddy probability maps derived from the satellite altimetric data (left) and numerical model (right). Red and blue lines denote 10% and 20% probability, respectively.

References

1. Bishop, S.P. and Bryan, F.O. (2013) Mesoscale eddy heat fluxes from observations and a high-resolution ocean model simulation of the Kuroshio.
2. Chaigneau, A., Gizolme, A., and Grados, C. (2008) Mesoscale eddies off Peru in altimeter records: Identification algorithms and eddy spatio-temporal patterns. Progress in Oceanography, 79, 106-119.
3. Chang, K.I., Hogg, N.G., Suk, M.S., Byun, S.K., Kim, Y.G., and Kim, K. (2002) Mean flow and variability in the southwestern East Sea. Deep-Sea Res. I. 49:2261–2279
4. Chelton, D.B., Schlax, M.G., Samelson, R.M., and de Szoeke, R.A. (2007) Global observations of large oceanic eddies. Geophys. Res. Lett., 34, doi:10.1029/2007GL030812.
5. Gordon, A., Giulivi, C., Lee, C., Furey, H.-H., Bower, A., and Talley, L. (2002). Japan/East Sea intrathermocline eddies. Journal of Physical Oceanography, 32, 1960-1974.
6. Hirose, N., Kawamura, H., Lee, H.J., and Yoon, J.-H. (2007) Sequential forecasting of the surface and subsurface conditions in the Japan Sea. Journal of Oceanography, 63, 467-481.
7. Hyun, J.H., Kim, D., Shin, C.-W., Noh, J.-H., Yang, E.-J., Mok, J.-S., Kim, S.-H., Kim, H.-C, and Yoo, S. (2009) Enhanced phytoplankton and bacterioplankton production coupled to coastal upwelling and an anticyclonic eddy in the Ulleung Basin, East Sea, Aquatic Microbial Ecology, 54, 45-54.
8. Kim, Y.B., Chang, K.I., Park, J.H., and Park, J.J. (2013) Variability of the Dokdo Abyssal Current Observed in the Ulleung Interplain Gap of the East/Japan Sea. Acta Oceanologica Sinica, 32, 12-23.
9. McClean, J.L., Maltrude, M.E., and Bryan, F.O. (2006) Measures of fidelity of eddying ocean models. Oceanography, 19, 104-117.
10. Nencioli, F., Dong, C., Dickey, T., Washburn, L., and McWilliams, J.C. (2010) A vector geometry-based eddy detection algorithm and its application to a high resolution numerical model product and high-frequency radar surface velocities in the Southern California Bight. J. Atmos. Oceanic Technol., 27, 564-579.
11. Park, J.J. and Kim, K. (2013) Deep currents obtained from ARGO float trajectories in the Japan/East Sea, Deep-Sea Res. II. 85:169-181
12. Sadarjoen, I.A., and Post, F.H. (2000) Detection, quantification, and tracking of vortices using streamline geometry. Comput. Graphics, 24, 333-341.
13. Senjyu, T., Shin, H.R., Yoon, J.H., Nagano, Z., An, H.S., Byun, S.K., and Lee, C.K. (2005) Deep flow field in the Japan/East Sea as deduced from direct current measurements. Deep-Sea Res. II, 52, 1726–1741
14. Shin, H.-R., Shin, C.-W., Kim, C., Byun, S.-K., and Hwang, S.-C. (2005) Movement and structural variation of warm eddy WE92 for three years in the western East/Japan Sea. Deep-Sea Res. II, 52, 1742-1762.
15. Takematsu, M., Ostrovskii, A.G., and Nagano, Z. (1999) Observation of eddies in the Japan Basin interior. J. Oceanogr., 55, 237-246.
16. Wyrtki, K., Magaard, L., and Hager, J. (1976) Eddy energy in the oceans. J. Geophys. Res., 81, 2641-2646.

Session II
Regional Climate & Ecosystem Projections

Prescription of Uncontaminated Open Boundary Conditions for Regional Ocean Model Simulations of Future Climate

Kwang-Yul Kim

School of Earth Environmental Science, Seoul National University, Korea
E-mail: Kwang56@snu.ac.kr

Open boundary conditions for regional ocean models are prescribed typically by using observational data or a model output. For future climate simulations using regional ocean models, we have to rely on general circulation model simulations for open boundary conditions. General circulation model output contains not only climate change signal but also internal variability or chaotic response of the climate system. Open boundary conditions, as a result, are contaminated by internal variability, which varies from one simulation to another. Therefore, we often take ensemble average of multiple simulations in order to alleviate contamination by internal variability. Such a process requires a large number of simulations and henceforth is costly and time consuming.

In this study, a new way of prescribing open boundary conditions based on CSEOF analysis is addressed. Given a future simulation of a general circulation model, climate change signal can be separated from natural internal variability produced by the model. Thus, open boundary conditions for a regional ocean model can be obtained without contamination by internal variability of the model in which the regional ocean model is nested. This eliminates the need for a large ensemble of GCM simulations for ocean regional models. Therefore, the new method of prescribing open boundary conditions is very efficient and cost-effective.

Given a future climate simulation of a general circulation model, say, for the A1B scenario, the data can be decomposed into

$$T(r,t) = \sum_n B_n(r,t) T_n(t), \qquad (1)$$

where $B_n(r,t)$ are cyclostationary loading vectors (CSLVs) and $T_n(t)$ are corresponding principal component (PC) time series. Unlike EOF loading vectors, CSLVs are periodically time dependent. That is,

$$B_n(r,t) = B_n(r,t+d), \qquad (2)$$

where d is called nested period. The nested period is the period of covariance statistics and is typically set to be one year. Each CSLV represents space-time evolution of a physical process and corresponding PC time series denotes the amplitude of the corresponding physical evolution. For an A1B scenario, for example, MIROC (Model for Interdisciplinary Research On Climate) temperature simulations, the climate change signal is extracted as the first CSEOF mode aside from the seasonal cycle (see Figure 1). As should be expected, the corresponding PC time series depicts “near-linear” amplification of 300 hPa air temperature according to the A1B scenario of radiative forcing.

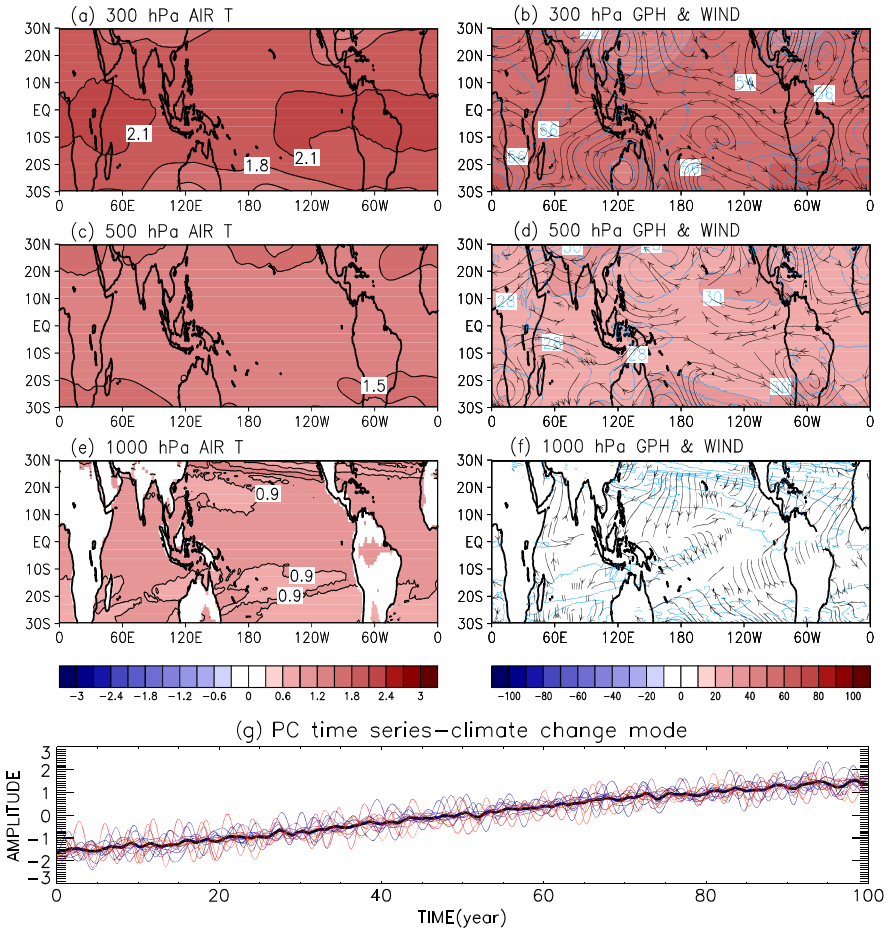

Figure 1. The second CSEOF mode of MIROC3.2-hires data (upper) and the corresponding PC time series (lower). This mode represents the climate change (warming) signal. Other AR4 models depict similar climate change. In the lower panel, the bold black line denotes the average of all (normalized) PC time series from different model datasets (thin colored lines).

It is important to extract the space-time patterns of other variables in a physically consistent way. This is done via regression analysis in CSEOF space. First, CSEOF analysis is conducted on a predictor variable (say, 1000 hPa wind), i.e.,

$$P(r,t)=\sum_n C_n(r,t)P_n(t), \qquad (3)$$

where $C_n(r,t)$ is the CSLV of the predictor variable, and $P_m(t)$ is the PC time series of the predictor time series. Then, regression between the two sets of PC time series yields

$$T_n(t)=\sum_{m=1}^{M}\alpha_m^{(n)}P_m(t)+\varepsilon^{(n)}(t), \qquad n=1,2,... \qquad (4)$$

where $\{\alpha_m^{(n)}\}$ are the regression coefficients, $\varepsilon^{(n)}(t)$ is the regression error time series, and M is the number of predictor time series used in the regression. The regression coefficients are determined such that the variance of regression error time series is minimized. A new loading vector of the predictor variable is determined by

$$D_n(r,t)=\sum_{m=1}^{M}\alpha_m^{(n)}C_m(r,t), \qquad (5)$$

where $C_m(r,t)$ is the CSLV of the predictor variable. Then, the predictor variable can be rewritten as

$$P(r,t) = \sum_n D_n(r,t)T_n(t). \quad (6)$$

As a result of regression analysis, the entire variables can be written as

$$Data(r,t) = \sum_n \{T_n(r,t), U_n(r,t), V_n(r,t), Z_n(r,t), ...\} T_n(t), \quad (7)$$

where the terms in the curly braces represent physical evolutions as manifested in different physical variables. Figure 1 shows the regressed patterns of predictor variables.

Figure 2 shows the regressed CSLVs of predictor variables averaged over a one-year period. Figure 3 shows the patterns obtained by subtracting the first 10-year average from the last 10-year average of the same predictor variables. As can be seen, the two sets of patterns are fairly similar yielding pattern correlations of (a) 0.97, (b) 0.96, (c) 0.99, and (d) 0.96. The patterns in Figure 3 are slightly smaller in magnitude than those in Figure 2. As the length of averaging increases, pattern correlation increases while the underestimation of the patterns becomes more serious. Thus, the 10-yr or 20-yr differences yield nearly identical spatial patterns with the patterns extracted via CSEOF analysis. An important difference, however, is the lack of detailed evolution history of the signal in the conventional method of subtracting long-term averages. Further, the length of averaging to remove natural variability sufficiently is not obvious.

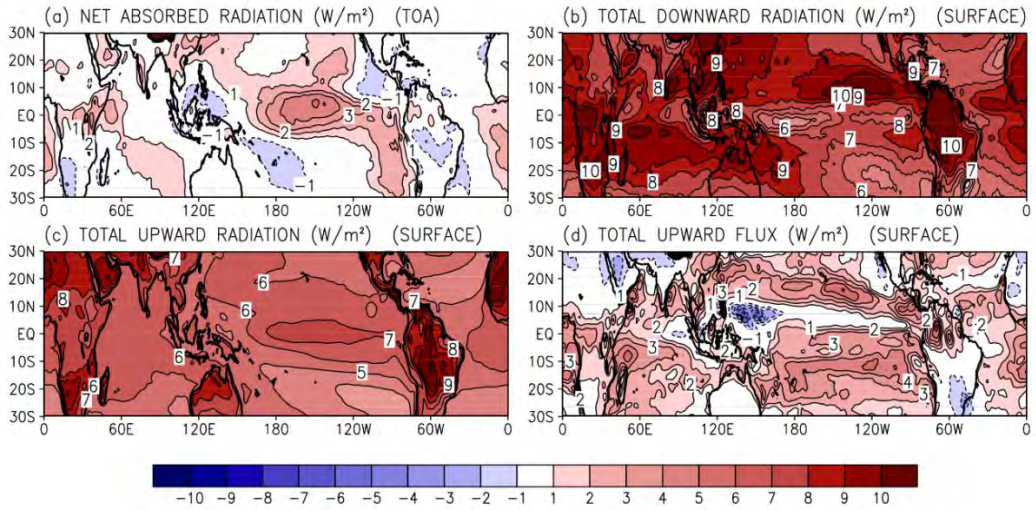

Figure 2. Annual average pattern of (a) net absorbed radiation at top, (b) total downward radiation at surface, (c) total upward radiation at surface, and (d) total upward heat flux in association with the climate change mode. The amplitude (PC) time series is shown in Figure 1.

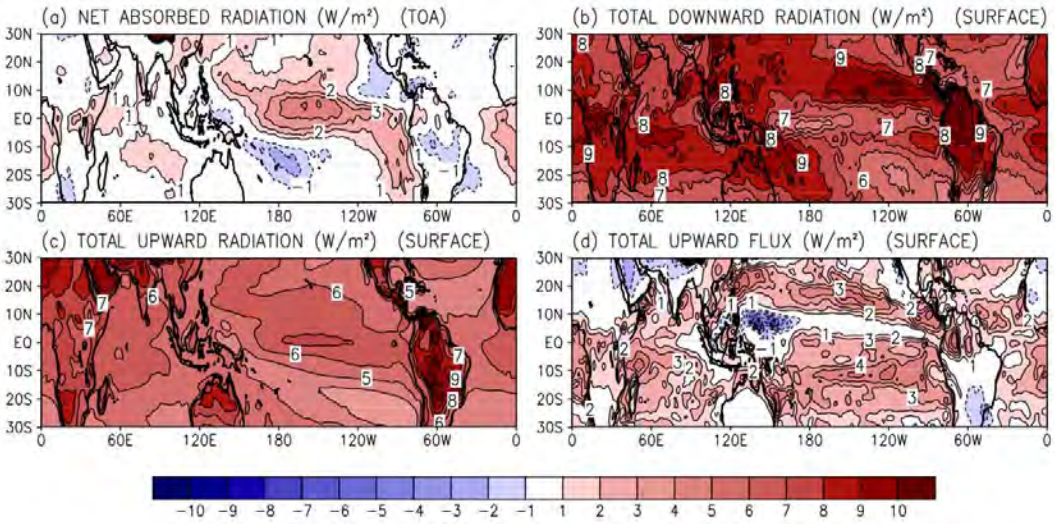

Figure 3. Patterns of (a) net absorbed radiation at top, (b) total downward radiation at surface, (c) total upward radiation at surface, and (d) total upward heat flux obtained by subtracting the first 10-year average from the last 10-year average of the respective variable.

Once the CSLVs of the climate change mode are identified from all variables as in (7), open boundary condition (OBC) for a control simulation with no climate change can be modified as

$$BC_{new}(r,t) = BC_{cntrl}(r,t) + BC_{ccs}(r,t), \tag{8}$$

where $BC_{new}(r,t)$ is the new boundary condition, $BC_{new}(r,t)$ is the boundary condition for a control simulation, and

$$BC_{ccs}(r,t) = \{B_2(r,t), U_2(r,t), V_2(r,t), Z_2(r,t), ...\} T_2(t) \tag{9}$$

is the change in the OBC due to the climate change signal (the second CSLV for MIROC3.2-hires model). This approach differs from a conventional approach

$$BC_{cnv}(r,t) = \sum_n \{B_n(r,t), U_n(r,t), V_n(r,t), Z_n(r,t), ...\} T_n(t). \tag{10}$$

The difference between the new and the conventional methods is

$$\begin{aligned} &BC_{new}(r,t) - BC_{cnv}(r,t) \\ &= BC_{cntrl}(r,t) - \sum_{n\neq 2} \{B_n(r,t), U_n(r,t), V_n(r,t), Z_n(r,t), ...\} T_n(t), \end{aligned} \tag{11}$$

which is generally non-zero and varies from one simulation to another due to the chaotic nature of the climate response. By taking an ensemble average of a large number of simulations

$$\langle BC_{new}(r,t) - BC_{cnv}(r,t) \rangle \doteq 0. \tag{12}$$

On the other hand, $BC_{ccs}(r,t)$ does not change from one simulation to another in any significant manner. Therefore, contamination by natural variability is nearly negligible in a regional ocean model simulation with the OBC in (8).

Regional Ocean Climate Model Projections for the British Columbia Continental Shelf

M.G.G. Foreman, W. Callendar, J. Morrison, D. Masson, I. Fine

Institute of Ocean Sciences, Fisheries and Oceans Canada, P.O. Box 6000, Sidney B.C., V8L 4B2, Canada
E-mail: mike.Foreman@dfo-mpo.gc.ca

The recent development of an ocean circulation model for the British Columbia continental shelf (Masson and Fine, 2012; henceforth MF12) and its application to realistically hindcasting water properties and flow fields for the period of 1995 – 2008 has created an unique opportunity to investigate future conditions in this same region (Fig 1). Numerous global and regional projections of the future oceanic and atmospheric fields that would be needed to force and initialize such a simulation are available from archives associated with recent Assessment Reports of the Inter-governmental Panel on Climate Change (IPCC). In this study we downscale forcing and initial fields from the Coupled Model Intercomparison Project phase 3 (CMIP3)

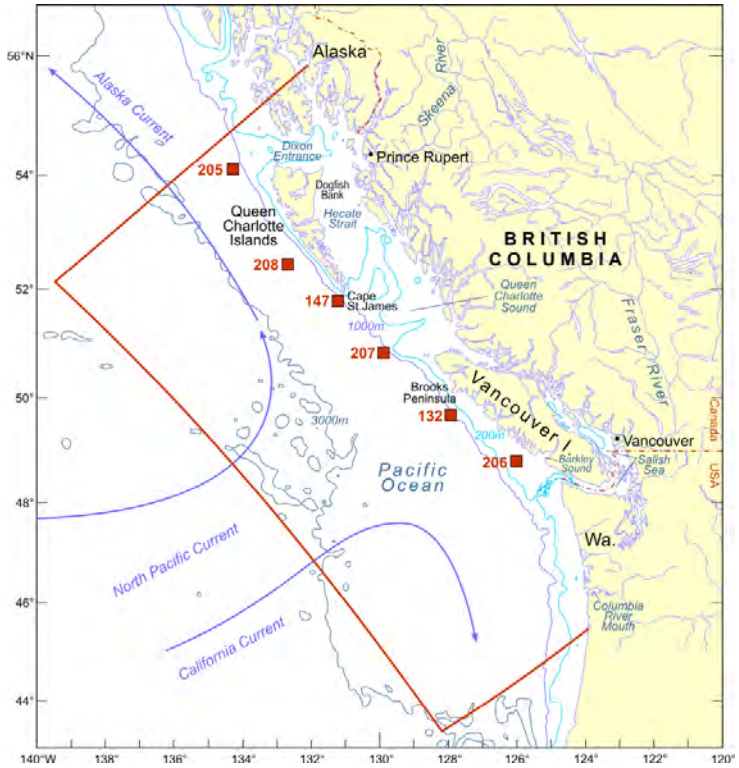

Figure 1. Map of the British Columbia continental shelf. Solid red lines denote the outer boundary of the regional shelf model and red boxes denote the Environment Canada (EC) buoys for which contemporary and projected winds are shown in Fig 2.

(http://cmip-pcmdi.llnl.gov/cmip5/data_description.html) and the North American Regional Climate Change Assessment Program (NARCCAP, http://www.narccap.ucar.edu/) and rerun the MF12 simulation to estimate circulation and water properties for the period of 2065-2078.

Though NARCCAP offers several model outputs and thus the possibility of forming ensemble statistics of future projections, computational and personnel limitations meant that only those from coupling the Canadian Global Climate Model 3 (CGCM3) and Canadian Regional Climate Model (CRCM) were used to force the simulations whose results are presented here. However, Morrison et al. (2013) do demonstrate the "representativeness" of this ensemble member. The NARCCAP projections were not used directly, as a comparison of winds over the contemporary period of 1970-1999 with re-constructed observations at buoys along the BC shelf revealed systematic biases in the timing of the spring and fall transitions and in particular, of the upwelling season (Fig. 2). As the CRCM/CGCM3 future winds generally displayed the same behaviour, employing them to directly force our future simulation would produce incorrect upwelling conditions and erroneous conclusions of their impact on future marine ecosystems.

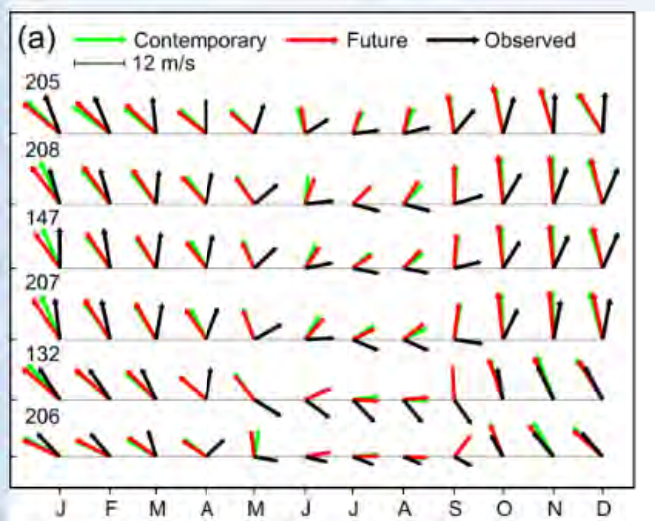

Figure 2. Mean monthly winds at the six EC buoys shown in Fig 1; observed means over the period of 1970-1999 (black), CRCM/CGCM3 means for the same period interpolated to the buoy locations (green), interpolated CRCM/CGCM3 means for 2040-2069 (red).

So instead, our future simulations were initialized and forced with fields that were the summation of those employed in the MF12 contemporary hindcast and the future-minus-contemporary NARCCAP anomaly fields. This "pseudo-global-warming" (PGW) approach has been employed before (e.g., Hara et al., 2008) and basically allows a climate comparison of present and future PGW years, where the latter is similar to the former in terms of inter-annual variations but includes future climatology.

Morrison et al. (2013) present numerous anomaly fields that were added to their MF12 counterparts but as an example, Figure 3 shows the monthly-averaged precipitation anomalies. January and February are projected to be notably wetter along the entire coast while October also shows significant increases along the north coast. The July anomaly is generally drier along the

entire coast while August, November and December are projected to be drier along the south coast. The average annual change over the entire region is approximately +0.5 mm/day.

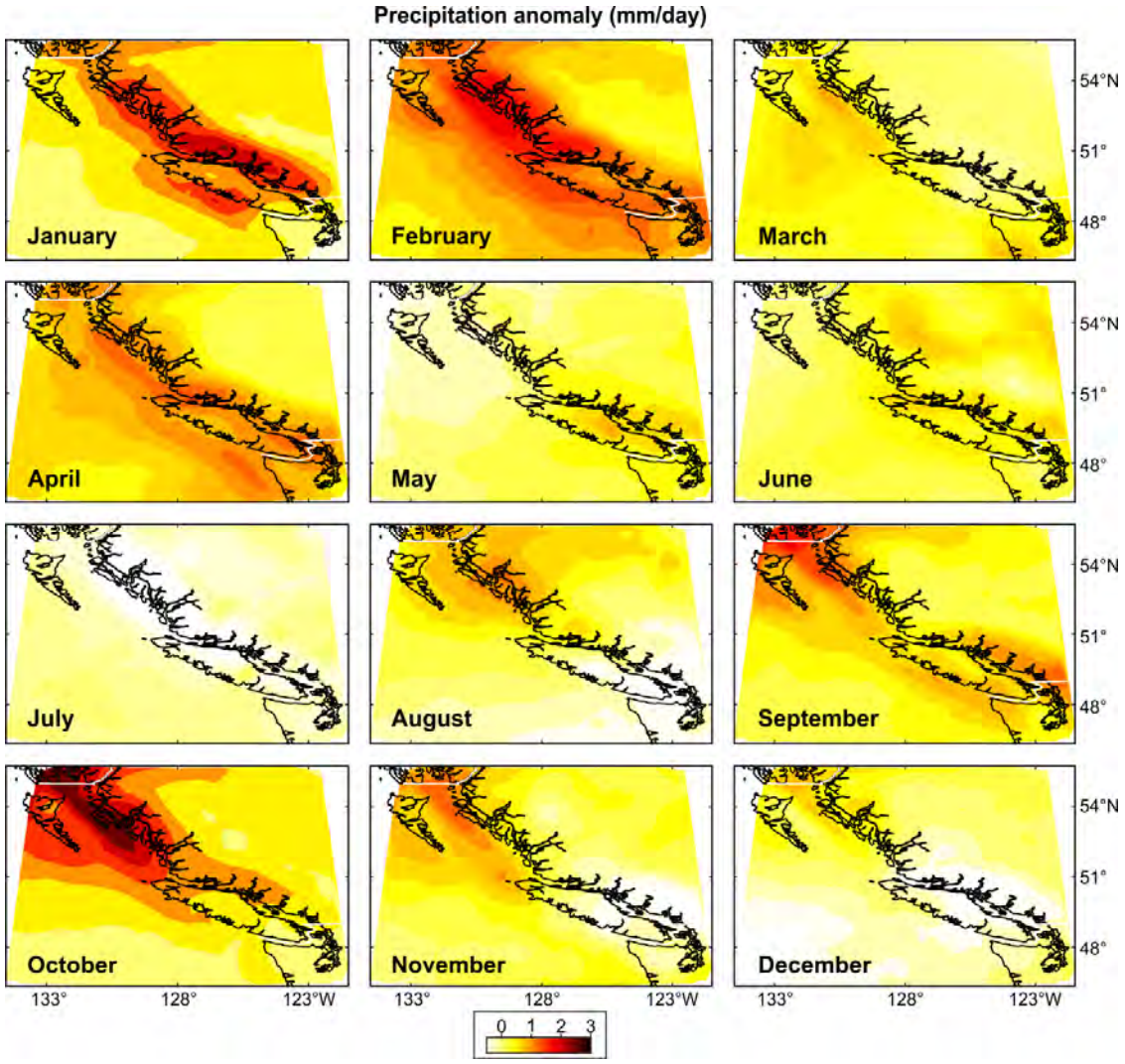

Figure 3. NARCCAP CRCM/CGCM3 monthly-averaged precipitation anomalies (mm/day) for the period of 2040-2069 minus 1970-1999.

Our future simulation was simply a rerun of MF12 with new initial and forcing conditions. Foreman et al. (2013) present and analyse numerous output fields of which two examples are presented here. Figure 4 shows contemporary and future eddy kinetic energy (EKE) within the model domain. Future higher values off the west coast of the Queen Charlotte Islands (Fig. 1) and northwest Vancouver Island (VI) are predominantly winter features that arise from stronger northwestward winds. Haida Eddies are generated when counterclockwise flows around Hecate Strait exit past Cape St James while similar flow separation arises when the northwestward Davidson Current passes Brooks Peninsula, the large (15km) promontory that crosses the VI continental shelf. Haida Eddies export coastal waters carrying nutrients and larvae offshore so changes in their magnitude may have important ecosystem consequences.

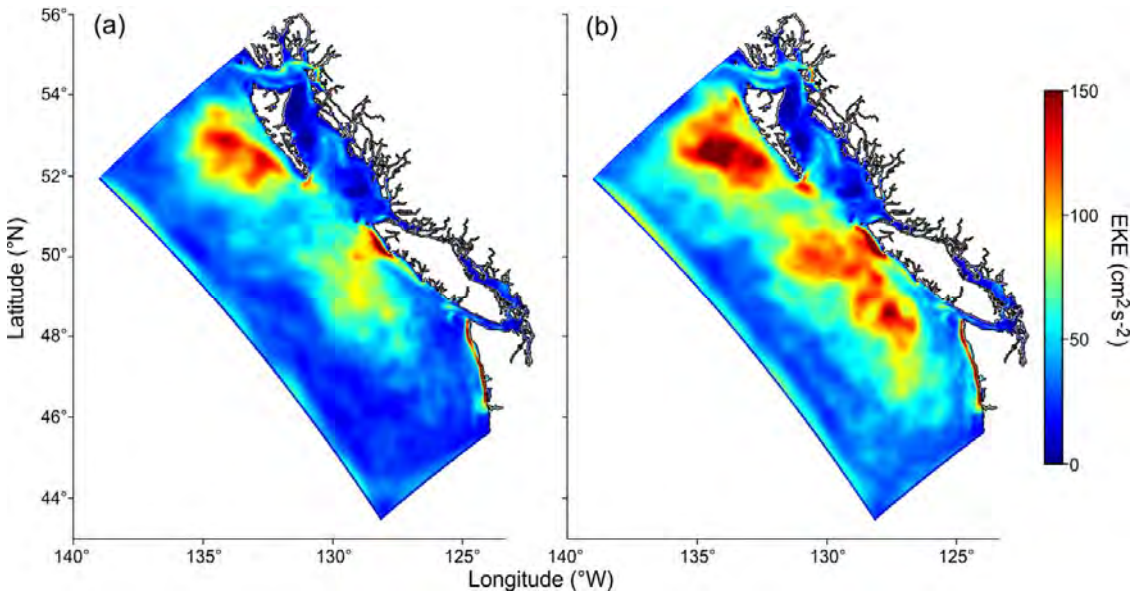

Figure 4. Annually-averaged eddy kinetic energy (cm^2s^{-2}) for the contemporary (from MF12) and future simulations.

Figure 5 shows contemporary and future seasonal alongshore currents, isotherms and isohalines along a transect crossing the mid VI shelf. Though some seasonal changes are seen in the five main currents in this region, the Jun-Aug panels show little change in the isotherm (e.g., 10°C in contemporary versus 11°C in future) and isohaline (e.g., 32.5 psu) contours near the shelf break. So small increases in the southeasterly wind stress near this transect (Morrison et al., 2013) are not accompanied by appreciable changes in upwelling.

Future work is planned to include the downscaling of forcing fields from other regional/global combinations in the NARCCAP archive and from analogous IPCC AR5 models that are now becoming available through the Coordinated Regional climate Downscaling Experiment (CORDEX, http://www.meteo.unican.es/en/projects/CORDEX). These fields will be used to initialize and force other simulations so that ensemble averages and estimates of uncertainty can be computed. Work has also begun on coupling the present circulation model to a biogeochemical model in order to investigate the impacts that the afore-mentioned physical changes will have on future marine ecosystems.

References

1. Foreman, M.G.G., W. Callendar, D. Masson, J. Morrison, and I. Fine. 2013. A Model Simulation of Future Oceanic Conditions along the British Columbia Continental Shelf, Part II: Results and Analyses. Submitted to *Atmosphere-Ocean*.
2. Hara, M., T. Yoshikane, H. Kawase, and F. Kimura. 2008. Estimation of the impact of global warming on snow depth in Japan by the pseudo-global-warming method, *Hydrological Research Letters*, 2, 61-64.
3. Masson, D., and I. Fine. 2012. Modeling seasonal to inter-annual ocean variability of coastal British Columbia, *Journal of Geophysical Research*, 117, C10019, doi: 1029/2012JC008151.

4. Morrison, J., W. Callendar, M.G.G. Foreman, D. Masson, and I. Fine. 2013. A Model Simulation of Future Oceanic Conditions along the British Columbia Continental Shelf, Part I: Forcing Fields and Initial Conditions. Submitted to *Atmosphere-Ocean*.

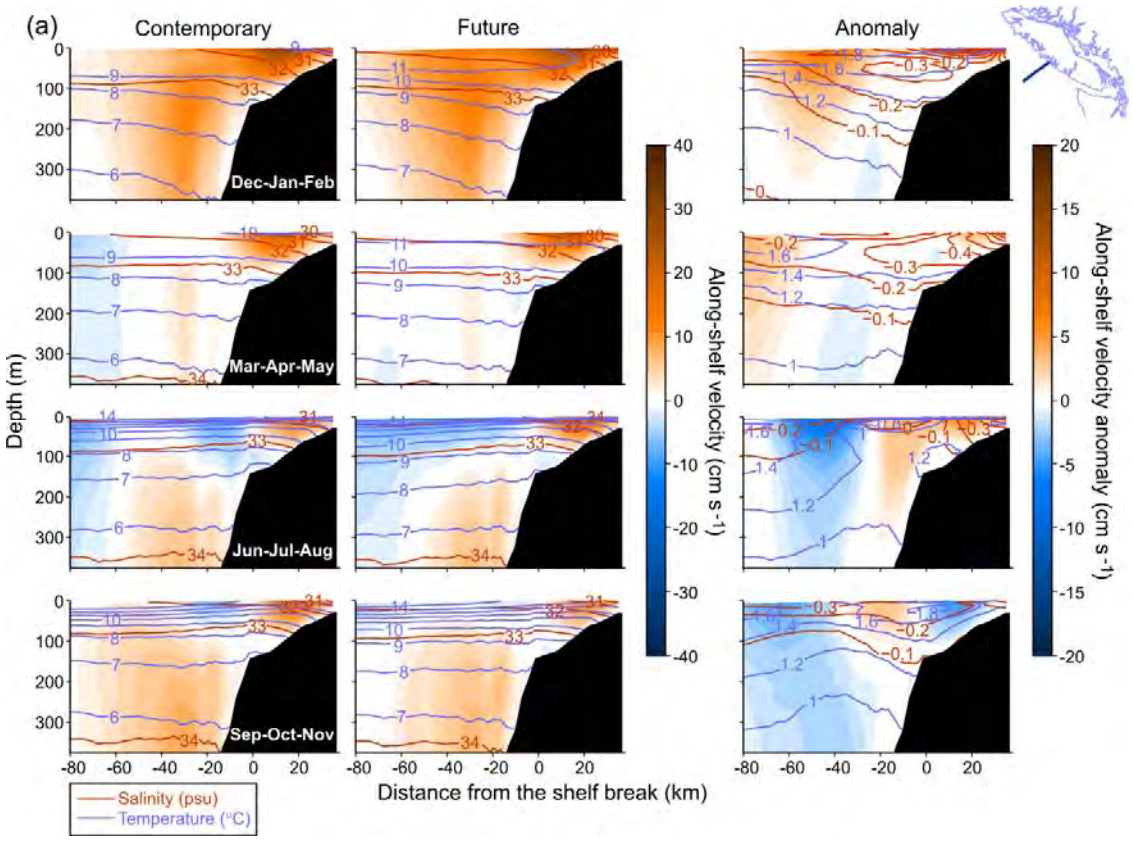

Figure 5. Along-shelf currents crossing, and temperature (blue) and salinity (red) contours along, a transect off the mid Vancouver Island shelf (Fig 1). Redder (positive) shaded areas indicate greater flow to the northwest while darker blue regions indicate greater flow to the southeast.

Multi-scale modeling of eastern boundary currents

***Enrique Curchitser*[1], *R. Justin Small*[2], *Kate Hedstrom*[3], *Brian Kauffman, Bill Large, Jim Hurrell*[2], *Mike Alexander*[4]**

[1]Rutgers University, [2]NCAR, [3]U. Alaska, [4]NOAA-ESRL

E-mail: enrique@marine.rutgers.edu

A well known problem with many global climate models is that they have too warm surface temperatures in the major upwelling systems, off the US west coast, the Chile-Peru coast, and south-west Africa (Fig. 1-1, see also Davey et al. 2002). The bias is exacerbated by cloud-radiation-SST feedbacks, such that over warm SST the stratocumulus cloud cover is less (Klein and Hartmann 1993) and hence more solar radiation can warm the surface. Earlier studies have suggested that the solar radiation bias is the main contributor to the SST bias (Ma et al. 1996) but recent studies have indicated the situation is more complex, with some compensation between shortwave and longwave errors, and the additional influence of latent heat flux errors being important (deSzoeke et al. 2010).

Other potential sources of errors include poor representation of wind stress near the coast, insufficient ocean upwelling, and errors in ocean surface currents and advection. Gent et al. (2010) found a reduction in warm SST bias in the Peru/Chile upwelling region when the atmospheric component of the NCAR-CCSM4 global climate model was changed from 2° to 0.5° They suggested that better, more alongshore coastal winds (partly due to the higher resolution of coastal topography) led to increased upwelling. Grodsky et al. (2012) used a set of low and high-resolution ocean models to investigate the bias off south-west Africa, and noted that a good representation of surface currents led to reduced SST bias. Many of the models exhibited equatorward currents (Benguela current) that were too weak or extended insufficiently northwards, and hence the lack of cold advection contributed to the warm bias.

Reduction of SST errors in the upwelling regions may lead to improvements elsewhere in global climate simulations. The results of Large and Danabasoglu (2006) suggest that if a global ocean model is forced to a true (observed) solution at the narrow coastal upwelling zone, ocean advection allows cooling to spread towards the equator and consequently affect the equatorial SST and hence the ITCZ. Another possibility for the spreading of cool SST anomalies from enhanced upwelling zones towards the equator is via air-sea turbulent heat fluxes, in a manner similar to that proposed by Chiang and Bitz (2005) for the spread of SST cooling in so-called water hosing experiments. In that case it is proposed that cool SST anomalies in high latitudes propagate towards the equator via Wind-Evaporation-SST (WES, Xie et al 1999) feedbacks. In addition to direct effects from equatorial SST, improved coastal upwelling and cooling may lead to improved stratocumulus cloud cover (see above), important to maintenance of the meridional asymmetry of the Pacific ocean (Philander et al. 1996), possibly reducing the double-ITCZ issue.

In this presentation, we show the effect of embedding a high resolution ocean model in a

global climate model. In contrast to traditional downscaling approaches, we allow for feedback from the regional model to the global model, which could be called “upscaling”. The focus of this presentation is the upwelling region off the US West Coast and the associated California Current System.

The main modeling system and coupling framework used for this work is CCSM4 (Gent et al. 2011). CCSM4 comprises the Community Atmosphere Model version 4 (CAM4: Neale et al. 2013), Community Land Model version 3.5 (CLM3.5, Oleson et al. 2008), Community Ice Code version 4 (Hunke and Lipscomb 2008), and the Parallel Ocean Program version 2 (Smith et al. 2010). CAM4 and CLM3.5 are on 1° grids with 27 vertical levels in CAM. POP2 is on a nominal “1°” grid (actually 1.11° in zonal direction and between 0.27° (at equator) and .54° at higher latitudes). It has 60 vertical levels, with 10m grid spacing in upper 100m.

The two-way embedded high-resolution ocean model is ROMS (Shchepetkin and McWilliams 2005), which has been configured for the California Current System (the domain is shown in Fig. 1a as a dashed line). ROMS is a free-surface terrain-following coordinate ocean model employing split-explicit timestepping. Three of the boundaries are open and use the Marchesiello et al. (2001) schemes. There is no explicit horizontal viscosity except in sponge layers near the open boundaries. As with POP2, ROMS employs the KPP scheme. The horizontal grid spacing is 7km, and there are 50 vertical levels which are stretched to give better vertical resolution in the surface and boundary layer.

Here, we present results that show that the SST bias is reduced off California due to a combination of more vigorous upwelling and equatorward surface currents in ROMS. We discuss the response to the alongshore wind stress and wind stress curl and we also look at the feedbacks on SST associated with the modulation of low level cloud and the air-sea fluxes. An upper ocean heat budget is performed to explain the reduction in SST bias. Finally, we show indications of a large-scale response to the improved SST biases in the coupled model.

References

1. Chelton, D. B., M. G. Schlax, and R. M. Samelson 2007. Summertime coupling between sea surface temperature and wind stress in the California Current System. J. Phys. Oceanogr., 37, 495-517.
2. Davey MK et al (2002) STOIC: a study of coupled model climatology and variability in tropical ocean regions. Clim Dyn 18:403–420
3. deSzoeke, S. P., C. W. Fairall, D. E. Wolfe, L. Bariteau and P. Zuidema, 2010. Surface flux observations on the southeastern tropical Pacific Ocean and attribution of SST errors in coupled ocean-atmosphere models. J. Clim., 23, 4152-4174.
4. Gent, P. R., S. G. Yeager, R. B. Neale, S. Levis and D. A. Bailey, 2010. Improvements in a half degree atmosphere/land version of the CCSM. Clim. Dyn., 34, 819-833.
5. Gent, P. R. and 12 co-authors, 2011. The Community Climate System Model version 4. J. Clim., 24, 4973-4991.
6. Grodsky, S. A., J. A. Carton, S. Nigam and Y. M. Okumura, 2012. Tropical Atlantic biases in CCSM4. J. Clim., XXX.

7. Klein, S. A., and D. L. Hartmann, 1993. The seasonal cycle of low stratiform clouds. J. Climate, 6, 1587-1606.
8. Large, W. G., and G. Danabasoglu, 2006. Attribution and impacts of upper-ocean biases in CCSM3. J. Climate, 19, 2325-2346.
9. Ma, C.-C., Mechoso, C. R., Robertson, A. W., and A. Arakawa, 1996. Peruvian stratus clouds and the tropical Pacific circulation: a coupled ocean-atmosphere GCM study. J. Clim., 9, 1635-1645.
10. Marchesiello, P., J. C. McWilliams and A. Shchepetkin, 2001. Open boundary conditions for long-term integration of regional oceanic models. Ocean Modelling, 3, 1-20.
11. Neale, R. B., J. Richter, S. Park, P. H. Lauritzen, S. J. Vavrus, P. J. Rasch, and M. Zhang, 2013. The mean climate of the Community Atmosphere Model (CAM4) in forced SST and fully coupled experiments. Accepted, J. Climate.
12. Oleson, K. W., et al., 2008. Improvements to the Community Land Model and their impact on the hydrological cycle. J. geophys. Res., 113, G01021, doi:10.1029/2007JG000563.
13. Philander, S. G. H., D. Gu, D. Halpern, G. Lambert, N.-C. Lau, T. Li and R. C. Pacanowski, 1996. Why the ITCZ is mostly north of the Equator. J. Clim., 9, 2958-2972.
14. Shchepetkin, A.F. and J.C. McWilliams (2005) The Regional Ocean Modeling System (ROMS): A split-explicit, free-surface, topography-following coordinates ocean model. Ocean Modelling 9, 347-404.
15. Xie, S.-P., 1999. A dynamic ocean-atmosphere model of tropical Atlantic decadal variability. J. Clim., 12, 64-70.

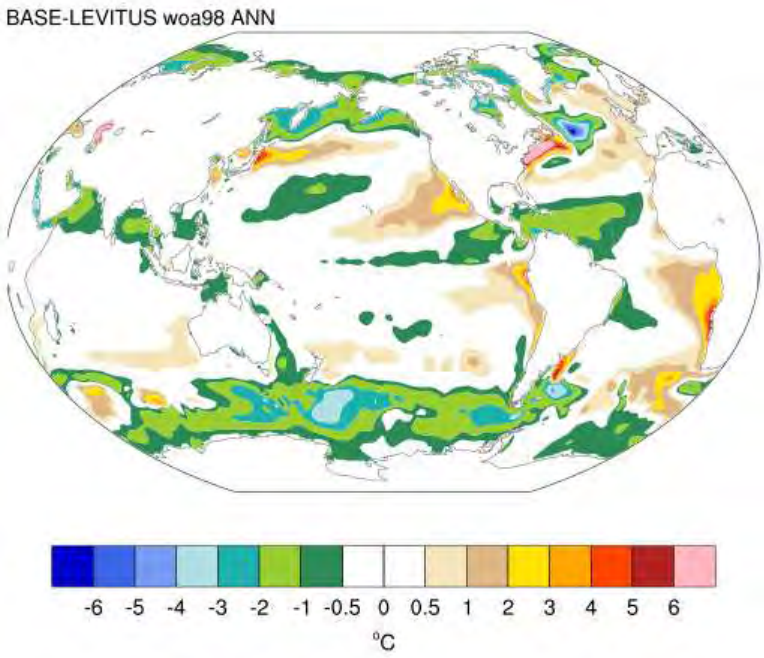

Figure 1. The bias in SST relative to Levitus WOA98 observational climatology. For the standard CESM (CCSM4) 1850 run, long-term (150 year) annual mean.

Towards reliable climate impacts projections of shelf and coastal sea ecosystems

Jason Holt[1], Sarah Wakelin[1], Jonathan Tinker[3], Momme Butenschon[2], Yuri Artioli[2], James Harle[1], Icarus Allen[2], Jason Lowe[3]

[1]National Oceanography centre, Liverpool, UK

[2]Plymouth Marine Laboratory, UK, [3]Met Office Hadley Centre, UK

E-mail: jholt@pol.ac.uk

Introduction

Across the whole marine environment, it is in the coastal and shelf sea that the impacts of climate change are likely to be most acutely felt. It is here that society interacts most directly with the marine environment, for example through the extraction of Living Marine Resources, and so the need to identify and ensure 'Good Environmental Status' is most pressing. It is well established that the Ocean-Atmosphere General Circulation Models (OA-GCMs) used in the CMIP and IPCC processes are primarily designed to provide reliable information at an ocean-basin to global and decadal to centennial scale. Hence, to provide information at the regional and local scales, some process of downscaling is required. This can be either statistical or dynamical, but given we are dealing with a complex non-linear and inter-connected system, and regional coupled hydrodynamic ecosystem models are reaching an increasing state of maturity, it is natural to opt for the dynamical approach. Moreover, a different range of physical and ecosystem processes tends to be important in shelf seas compared with the open ocean, such as tides, mixing at multiple boundary layers, benthic exchanges, complex optics, and variable stoichiometry. Hence, the downscaling process tends to involve a change in complexity (usually an increase) in the model system, particularly when more intricate biogeochemical and ecosystem/ecological process are of concern.

The ultimate goal of downscaled climate impacts studies is to provide reliable projections into the future to, for example, aid policy decisions or inform the public debate on the need for mitigation action. Many studies have now started to investigate this, but are generally still in the domain of 'sensitivity' studies (e.g. Holt et al., 2012; Skogen et al., 2011): they provide dynamically consistent views of the future, but have difficulty ascribing likelihood to these views. The challenge of moving to a more probabilistic predictive approach is immense, as we are dealing with a multiply coupled system consisting of scenario, global GCM, regional physical model, and region ecosystem model. If each model component has axes of uncertainty of model structural and parameter uncertainty, and natural variability, we have a 9-dimensional uncertainty space, before we even consider scenario uncertainty. It is difficult to see how this can be comprehensively covered using probabilistic approaches (to build a PDF) without resorting to statistical methods, such as emulators. These, however, are not appropriate here as our basic process understanding is still developing. Providing a partial view of uncertainty is also potentially misleading. Hence, alternative approaches are needed and for these we draw on process understanding and analysis, with the aim of at least robustly identifying the sign of

possible change, if not definitively quantify this.

In this paper we consider practical ways in which we can move from the sensitivity study arena to providing more reliable evidence for future change. The robustness of the information that can be provided is largely rooted in the diverse range of drivers and responses, how they are represented by models, and this in turn in the numerical experiment design. Here we draw on the experience of the UKCP09 (Holt et al., 2010; Lowe et al., 2009) and MEECE (www.meece.eu) projects, the continuing work from these and the lessons learned. We focus on the northwest European continental shelf, and on primary production as the engine that drives the marine ecosystem (Figure 1; see (Holt et al., 2012).

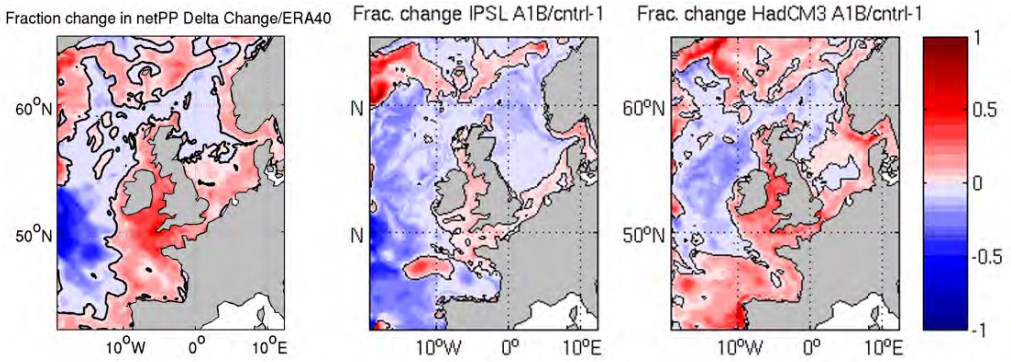

Figure 1. Fractional change in netPP from three POLCOMS-ERSEM simulations. Left: Delta change (IPSL-CM4 with ERA40 reference); Centre: Direct forced (IPSL-CM4; Holt et al 2012); Right: Direct forced (HadCM3).

Figure 1 shows the fractional change in primary production from three time slice experiments. These show the difference between mean annual conditions representative of 1980-2000 and 2080-2100. Two experiments are driven by the IPSL-CM4 model but with different forcing approaches, and one by the HADCM3 model. These are dynamically consistent sensitivity studies, and while they show some similarities, they differ qualitatively and quantitatively in many regions. So the key question is how do we move from this rather confused picture to apposition where we can provide reliable evidence about future change? First we must consider what the driving processes are and how they relate to external forcing.

The Driving processes

How global scale climate change might impact coastal and shelf seas is far from straightforward. A myriad of physical processes can potentially act as vectors transferring the larger scale oceanic and atmospheric variability and change to regional sea physics, biogeochemistry, lower trophic level ecosystems, and so up the foodweb. These processes act on a wide range of time scales, being strongly dependent on the prevailing conditions of an individual regional sea basin. The response of the coupled physical-lower trophic level ecosystem system to climatic drivers depends on three paradigms of biophysical interaction:

i. Transport processes that set the elemental budget (of carbon, nitrogen etc) of a particular region

ii. Seasonal and mesoscale processes that mediate the nutrient (re-)supply and the phyoplankton's exposure to light

iii. Direct physiological response to the environment (e.g. temperature)

If we wished to consider the ecosystem at the species level we would have to add to these detailed changes in transport timing, rates and patterns (e.g. the 'connectivity' of regions), but this is not considered further here. The distinction between i and ii relates to time scales of the transport relative to the biogeochemical processes. They are short in ii : biology and chemistry responds on the time scale of the transport, and long in i: generally advective transport sets the background conditions independent of the more rapid biogeochemical processes. Processes mediating ii tend to be diffusive, but two important exceptions are coastal upwelling (e.g. at the Eastern Margins of ocean basins) and coastal currents (e.g. near river inflows) where advective processes dominate at the seasonal time scale. Sea ice processes more naturally fit within ii. These paradigms need to be considered in the appropriate geographic context, notably the mixing regime, the presence/absence of sea ice and the time scale of exposure to wider oceanic conditions. Hence our understanding of how these processes can drive ecosystem change should inform our downscaling experiment design and so simplify the treatment of uncertainty by indentifying, which axis is important and which less so.

To explore the relative importance of the various external drivers, a series POLCOMS-ERSEM experiments is considered, building on the work published by Holt et al (2012). The approach we adopt is to start with the self consistent set of future forcing (from the OA-GCM) and systematically remove aspects of the climate change signal by swapping in the corresponding present day forcing, with the year order randomised. This differs from a more conventional sensitivity experiment (e.g. Skogen et al., 2011) in the treatment of non-linearities. Here we aim to identify the effects of a driver and all non-linearities associated with it under future conditions. In the alternative approach the non-linearities are associated with present day conditions, so the non-linear climate response is missing.

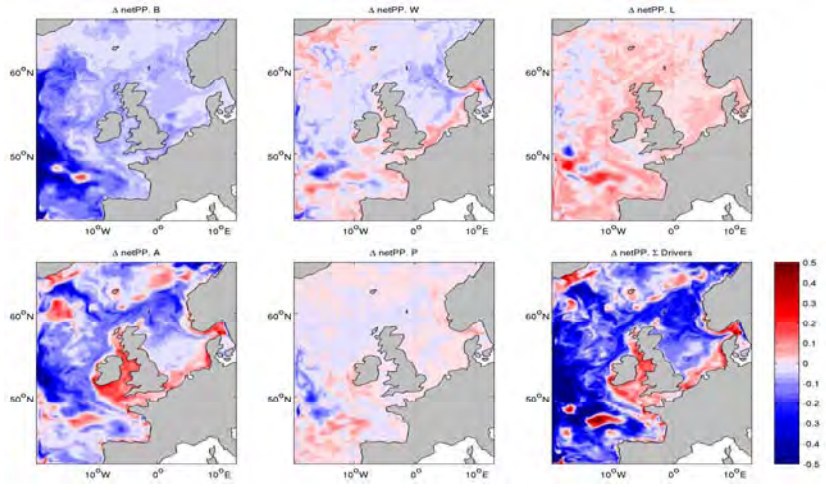

Figure 1. Driver experiments with POLCOMS-ERSEM. Fractional change in netPP associated with five external drivers and their non-linear interactions: boundary nutrients (B); wind (W); short wave radiation (L); air temperature (A); precipitation (P). Also shown is the sum of these components.

Here we consider five driver experiments, each an 18-year simulation following 5-years of spin up, for: wind (W), short wave radiation (L), air temperature (A), boundary nutrients (B) and precipitation (P). The change in net primary production associated with each of these is shown in Figure 4. This shows boundary nutrients, wind, and air temperature all conspire to reduce net primary production in the central and northern North Sea. Air temperature, SWR and wind effects dominate in the Celtic Seas giving an increase in net primary production. It is apparent from these results that changes in air temperature and wind can both increase and decrease netPP. The former acts through physiological and stratification effects, whereas the latter acts through growing season and mixing effects. It is the balance of these competing processes, often driven by elements of the climate model that are themselves highly variable, that leads to the complex spatial variability in response seen in these shelf seas.

It is insightful to consider how these driver experiments add up: linearly, synergistically or antagonistically. The difference between the sum of the driver experiments (Figure 4) and full model simulation (figure 1, centre panel) can be interpreted as being due to the non-linearity in the system.

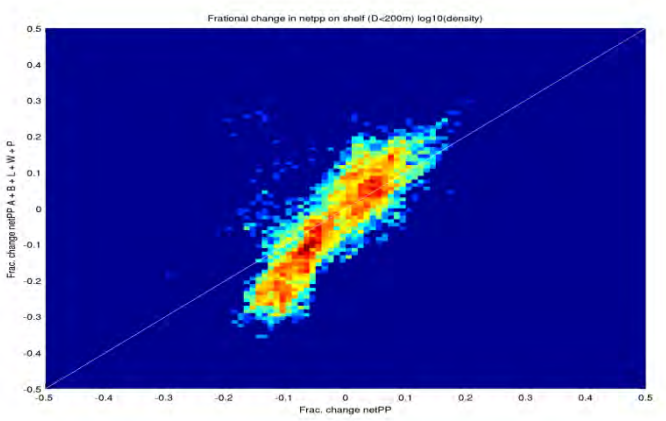

Figure 2. A density plot (proportion of number of grid cells in each bin) of fraction change in netPP from the full model and the sum of the driver experiments.

Comparing the full model change in netPP and the sum of these experiments, the two are seen to qualitatively agree well. This can be confirmed with a density plot (Figure 3), which demonstrates a large proportion of the system (on-shelf) is close to linear and the sign of the change is well represented. There is, however, a distinct tendency towards damping: the full model has a weaker response than the combined driver experiments. This is particularly apparent in the negative regions, which are substantially less impacted than the combined experiments would suggest. Of particular interest is the increase in netPP in the Irish Sea, Celtic Sea and northern English Channel, especially evident in the air temperature component; again with a damped effect. These regions are characterised by weak transport and a similar (positive) effect is also seen in the air temperature effect on total nitrogen (sum of pelagic, benthic, inorganic and organic components).

Taken together, this demonstrate a complex interaction between drivers, biogeochemistry and

ecosystem response. Behind the picture described by Holt et (2012) of an overall increase in primary production in coastal regions and decrease in regions exposed to ocean shelf exchange are larger changes in the timing of production, a more detailed analysis also shows stronger spring blooms, weaker summer growth and a shift to towards diatoms in the community composition.

Downscaling experiment design

Choosing how to run downscaling experiments to give reliable results with a practical number and length of simulations is a challenging business. Issues relating to experiment design include the future scenario and the treatment of natural variability, the choice of OA-GCM and specific driving variables, the approach to driving the regional model and the experiments themselves and their analysis. Central to this design are two concepts that define the timescale of the problem: first the need to distinguish between natural variability and anthropogenic climate change, and seconds the time scale of the adjustment of the system to external forcing. The first is made more complex by the fact that OA-GCM are not generally constrained to the observed phase of natural variability and this is compounded by the fact that some of the important modes are not short compared with the time scales of interest (e.g. PDO, AMO). Hence, care is needed both validating the models (the observational base is inevitably biased to a particular phase of variability) and interpreting the results of the future projection; some degree of 'contamination' by natural variability is difficult to avoid. This is tensioned against the policy drivers to provide information on as short a time horizon as possible, and has led to the evolution of coupled assimilative models.

The issue of the adjustment time of the system relates to the choice between running transient and time slice experiments. In the former, the model is simply run into the future, forced by the OA-GCM to provide sea surface and open ocean boundary conditoins. In the latter the model is run, forced by the OA-GCM, for a future period and a present day control, and mean conditions between the two compared; this is an approach common to many impacts studies (as above). The issue of adjustment is less marked for transient simulations (after an initial 'spin-up' period), but is a particular consideration for timeslice experiments. In the shelf sea context communication with the atmosphere is relatively rapid (seasonal) and the adjustment largely relates to ocean-shelf exchange (Holt et al., 2012). For deeper regional basins (e.g. Baltic and Black Sea), adjustment to atmospheric conditions for depths below the seasonal mixed layer is considerably slower and timeslice experiments need to be considered with the caveat that the system is not fully adjusted. The same is also true for the benthic system, where the adjustment can take many decades.

Hence, timeslice simulations are very useful because of their computational cheapness, the easy of manipulating the forcing data (e.g. imposing bias corrections) and using delta change approaches, which require less complete forcing information (e.g. a monthly rather than sub-daily frequency). However, the issues of adjustment from initial conditions and separation of climate change signal from natural variability means their results can be misleading unless considered in conjunction with a transient experiment. For example, the temperature in the 30-year timeslices in Figure 2 adjusts sufficiently rapidly to give an acceptable climate change difference compared with the transient. In this case both future and past time slices happen to show a similar pattern of natural variability. However, a timeslice around 2050, would not and so would probably over estimate the climate change signal. This would be very difficult to identify if the transient simulation had not been run.

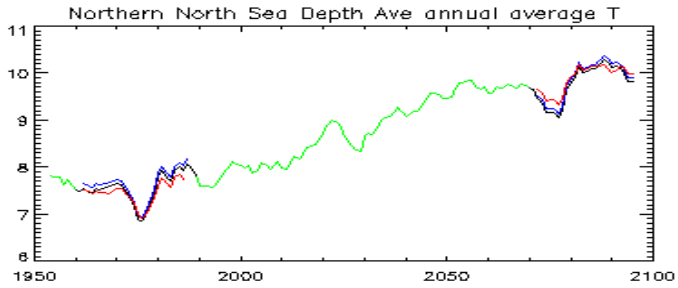

Figure 3. Mean North Sea temperature in a HADRCM3 forced POLCOMS simulations run in both transient and time slice mode.

The question remains: how we move from these single simulations to gauge the range of possible future outcomes? The natural approach is to run ensembles of simulations. From a forcing point of view these could be multi-model (MME) or perturbed parameter (PPE) ensembles, or both. Figure 3 shows an example of a 6-member ensemble derived from perturbing parameters in the driving regional climate model (see Lowe et al., 2009). While this starts to show differences in spread for different regions and time periods, it only gives a partial picture of the uncertainty: scenario uncertainty and uncertainty in the regional model are not considered. These maybe positively or negatively correlated, and so may broaden or narrow the spread. The model uncertainty is a particular issue as we move from physics only simulations (as here) to include the ecosystem, and so increase the inherent uncertainty in the model (Allen et al., 2007). As noted above, treating this in a probabalistic sense rapidly becomes intractable.

Hence there is a need for a practical framework that allows a small ensemble to be prescribed that 'envelopes' the uncertainty in a maximum and minimum sense. If our focus is to be on the internal uncertainty of the coupled hydrodynamic ecosystem model, then we need a method of selecting driving OA-GCMs or RCMs (MME or PPE) that give a 'high' and 'low' response of a particular variable. Given, the complex, heterogeneous response seen in Figure 1, this is not so straightforward, and is not well constrained by a simple parameter such as the global or regional climate sensitivity. Instead a detailed process analysis is required.

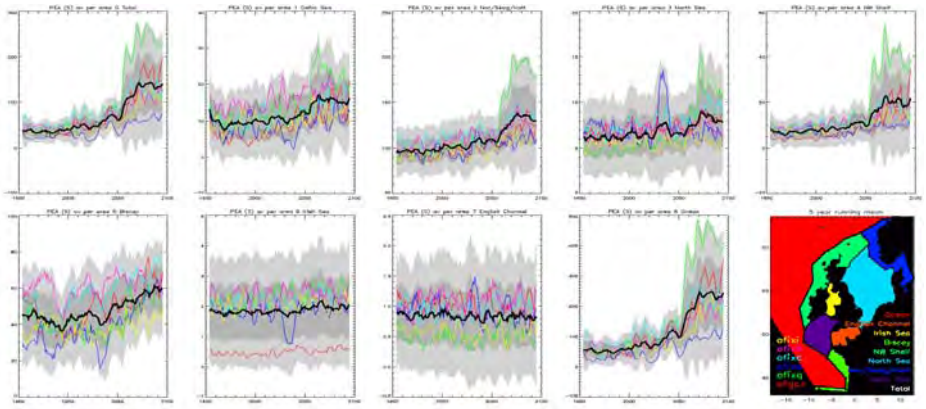

Figure 4. Six member ensemble of a physics only model (Holt et al., 2010) forced by the PPE of HADRM3. Variable shown is the potential energy anomaly averaged over 8 regions and the

total. The black line shows the ensemble mean and the coloured lines the members.

The next steps

The driver experiments described above could be used to select forcing OA-GCMs that are likely to give a high and a low change in net primary production (or other diagnostic). Simplistically, a model with low (high) boundary nutrients and low (high) light levels, could be selected over those with different air temperatures and wind as the response to these is more regionally dependent. However, this would benefit from a more detailed biogeographical analysis to make the selection. The selected models should also need to be be judged on their fidelity in reproducing basic regional atmospheric and ocean properties, such as the North Atlantic Storm Track and Gulf Stream positions, (as in Overland and Wang, 2007 for the Arctic).

Uncertainty in the physical model can be most straightforwardly captured by using models of very different formulation. Hydrodynamic models have only a few free parameters, so structural uncertainty is likely to dominate in this case. One choice would be to use an unstructured mesh finite volume and an structured mesh finite difference model, noting that care would be needed to ensure substantially different subgrid scale parameterisations are used. Uncertainty in the ecosystem model can be captured by both different parameter sets and models of different complexity. In selecting different hydrodynamic and ecosystem models, care is needed that all are configured with a similar degree of care and expertise, and give comparable validation against contemporary observations. On this basis, their selection is likely to be made on practical grounds. In terms of ecosystem model parameter selection, this could be done using automatic tuning approaches such as generic algorithms, and they could be tuned to give ‘high’ and ‘low’ response by partitioning the training data. For example, we can presume primary production is related to chlorophyll observations and so could produce two model parameter sets, one tuned to the upper quartile of the observations and the other to the lower quartile.

Hence this simple framework would lead to a, tractable, 16-member ensemble, for a single emissions scenario. While this would not be comprehensive and would have some subjective elements, it would cover many aspects of the uncertainty and so be an important first step.

Conclusions

To conclude, climate impacts in shelf seas ecosystems are a complex interplay between competing drivers and processes, often with different signs. Hence, identifying the sign of expected change with some confidence is an important and useful step forward. The high level of spatial heterogeneity in shelf seas means that the lessons learnt in global models do not directly translate to these regions. The scale problem is as much about process representation as geographic detail. Moving away from sensitivity studies to treat uncertainty, requires a framework for simulations that can encompasses as many aspects of this uncertainty as possible. Here, we propose a simple approach, based on process analysis and a selection of high and low cases for each component.

References

1. Allen, J.I., Holt, J.T., Blackford, J.C., Proctor, R., 2007. Error quantification of a high-resolution coupled hydrodynamic-ecosystem coastal-ocean model: Part 2. Chlorophyll-a, nutrients and SPM. *Journal of Marine Systems*, 68, 381-404.

2. Holt, J., Butenschon, M., Wakelin, S.L., Artioli, Y., Allen, J.I., 2012. Oceanic controls on the primary production of the northwest European continental shelf: model experiments under recent past conditions and a potential future scenario. *Biogeosciences*, 9, 97-117.
3. Holt, J., Wakelin, S., Lowe, J., Tinker, J., 2010. The potential impacts of climate change on the hydrography of the northwest European Continental shelf. *Progress in Oceanography*, 86, 361-379.
4. Lowe, J.A., Howard, T.P., Pardaens, A., Tinker, J., Holt, J., Wakelin, S., Milne, G., Leake, J., Wolf, J., Horsburgh, K., Reeder, T., Jenkins, G., Ridley, J., Dye, S., Bradley, S., . 2009. UK Climate Projections science report: Marine and coastal projections. *Chaos*. Met Office Hadley Centre, Exeter, UK. .
5. Overland, J.E., Wang, M., 2007. Future regional Arctic sea ice declines. *Geophysical Research Letters*, 34, L17705, doi:17710.11029/12007GL030808.
6. Skogen, M.D., Drinkwater, K., Hjollo, S.S., Schrum, C., 2011. North Sea sensitivity to atmospheric forcing. *Journal of Marine Systems*, 85, 106-114.

Future climate change projection of northwestern Pacific marginal seas by dynamical downscaling of the GCMs

Yang-Ki Cho[1], Gwang-Ho Seo[1] , Byoung-Ju Choi[2], Kwang-Yul Kim[1], Bong-guk Kim[1]

[1]School of Earth Environmental Science, Seoul National University, Korea
E-mail: choyk@snu.ac.kr, seogwangho@gamil.com
[2]Department of Ocean Science and Engineering, Kunsan National University, Korea
E-mail : bjchoi@kunsan.ac.kr

Abstract: This study introduces the future climate change projection in the northwestern Pacific marginal seas by dynamical downscaling global climate model (GCM)s. To study the detailed features of future climate change, Northwest Pacific model with horizontal grid spacing of 0.1° was set up. We used the Regional Ocean Model System (ROMS) together with the SRES A1B simulation for the period 2001–2100 with the Miroc-3.2(hire), Ukmo-hadgem1 and MPI-echam5 climate models for the northwestern Pacific. We calculated warming trends from the GCMs future projections using Cyclostationary Empirical Orthogonal Function analysis (CSEOF). CSEOF decomposes space-time data into cyclo-stationary loading vectors. The warming trends from 2010 to 2100 are added to the present surface forcing and open boundary data for the regional climate projection. Although the projection from the NWPS is generally in agreement with that of GCMs, the former results in substantial regional details, transports, and improving the mean seasonal temperature. Downscaling regional model shows relatively rapid temperature increments in the Bohai Sea and northern East/Japan Sea. Volume transport and heat transport through the Korea Strait are likely to increase under the global warming condition. We calculate volume and heat transport through Korea Strait for the period 2010 to 2100 from downscaling regional model. The annual mean volume transports and heat transports in the Korea Strait were 2.4 + 0.2 Sv and 0.18 + 0.02 PW.

Keywords: Climate change projection, northwestern Pacific, Marginal Seas, ROMS

1. INTRODUCTION

The northwestern Pacific (NWP) marginal seas have different physical and biological characteristics. Fine topography and shelf processes like tidal current and river are important in realistic simulation in each marginal seas. Global climate models (GCM) have coarse resolution and do not yet typically include the relevant shelf processes (figure 1). The relatively coarse resolution of global climate model results in isolation of the marginal seas from large open ocean basins or unreasonable large or small transport in the straits (figure 2). Exchanges of water between the semi-enclosed marginal seas and the open ocean are important to simulate regional climate change and what in nature involves the straits

Great efforts have been made to improve the understanding and predictability of the NWP circulation by using numerical models (Cho et al., 2009, Cho et al., 2013, Kim et al., 2013, Seo et al., 2013). Several global climate models have provided global future projections of large scale distribution of heat and salt and changes in oceanic processes (Stock et al. 2011). Due to the coarse resolution of GCM, changes in coastal and shallow water regions and marginal seas were not well investigated. Also the simple spatial interpolation cannot solve changes of coastal and shallow region (Jones et al., 1995). So we used dynamic downscaling method to simulate the

regional climate at higher resolution. Dynamical downscaling using regional climate model (RCM) obtains more detailed local scale climate change information.

This study applies ocean dynamical downscaling to investigate the impact of climate change on the boundary currents in the NWP marginal region. We are downscaling global climate models for future regional climate projection in the marginal seas of NWP to examine changes in temperature and transport

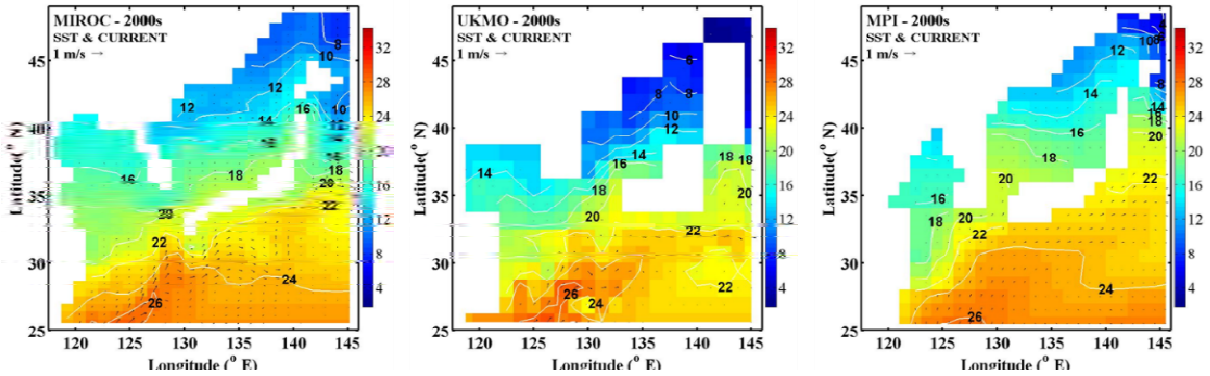

Figure 1. Surface temperature and current of GCMs (left) MIROC, (middle) UKMO and (right) MPI in the 2000s. Color indicates sea surface temperature and vectors surface currents.

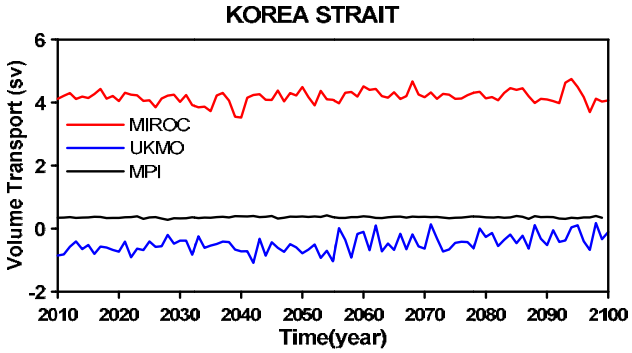

Figure 2. Volume transports of GCMs (red line) MIROC, (blue line) UKMO and (black line) MPI from 2010 to 2100 in the Korea Strait

2. MODEL

2-1. Global climate models

The SRES A1B scenario of the 4th assessment report of the International Panel on Climate Change (IPCC) was selected for this experiment. We evaluated global climate models based on the observed current and temperature and selected three global models for the regional downscaling. These models are the UKMO HadCM2 of the Hadley Centre in Reading (Johns et al. 1997), the ECHAM5 of the Max Planck Institute for Meteorology in Hamburg (Roeckner et al.

2003) and Miroc-3.2(hire) of Center for Climate System Research in Tokyo (K-1 Developers. 2004). Time-dependent warming forcing from GCM simulations is added to the surface and lateral boundaries of the regional model.

2-2. Regional climate model

We use Regional Ocean Modelling System (ROMS) (Shchepetkin and McWilliams 2005) for the projection of climate change in the NWP marginal seas. ROMS is a free-surface, terrain following, primitive equation ocean model employing the Arakawa-C staggering in the horizontal. The model domain is the north western part of the Pacific (18°N to 49°N, 118°E to 155°E) (Figure 3). The horizontal grid spacing is approximately 10 km, with 20 vertical levels.

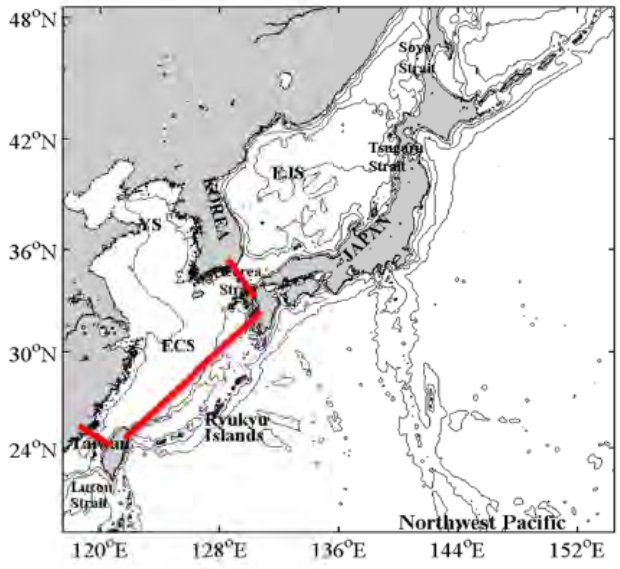

Figure 3. Pacific model domain for the regional down-scaling. The thick solid line represents the section monitoring transport in the Korea Strait. Contour lines are water depths in meter.

We calculated warming trend from the GCMs outputs using cyclostationary Empirical Orthogonal Function analysis (CSEOF; Kim et. al.,1996) to resolve accurate temporal evolution of climate change. The CSEOF technique is useful for extracting physically evolving spatial patterns. Time-space data P(r, t) are written as decompose the climate data into a set of independent modes LVn(r, t) and their principal component (PC) time series, PCn(t)

$$P(r,t) = \sum_n LV_n(r,t)PC_n(t) \quad (1)$$

Where n, r, and t represent the mode number, space and time,

The second mode of CSEOF from GCM projection results represents global warming trend for the projected period. PC time series of the second mode represents the long-term trend of climate change.

Three GCMs show similar temperature increase, although they are using different numerical models and resolutions. Climate change signals are estimated from each GCM projection using CSEOF analysis and the climate change signals from each GCM projection were added to the surface forcing and open boundary values of year 2001, present atmospheric and oceanic condition, for the future regional climate projection.

Future atmospheric forcing (t) = present atmospheric forcing (2001) + GCMs CSEOF warming trend (second mode) x monthly climate change PC time series (t), t = 2002, … , 2100. (2)

3. Results

Climate projections with the NWP model were produced for the next 100 years. In presenting our results, we focus on the similarities and differences between the GCMs and regional models in NWP. The Tsushima Current (TC) is a prominent ocean current in the NWP marginal seas. However, probably because of GCM's coarse horizontal resolution, spatial distributions of the SST and current speed from GCMs (UKMO, ECHAM5, MIROC) do not well define the TC (Figure 4). Downscaled regional model retained the well-defined TC both in summer and winter (Figure 5). In summer, some coastal regions in the Yellow Sea attain a maximum temperature of 30-32°C.

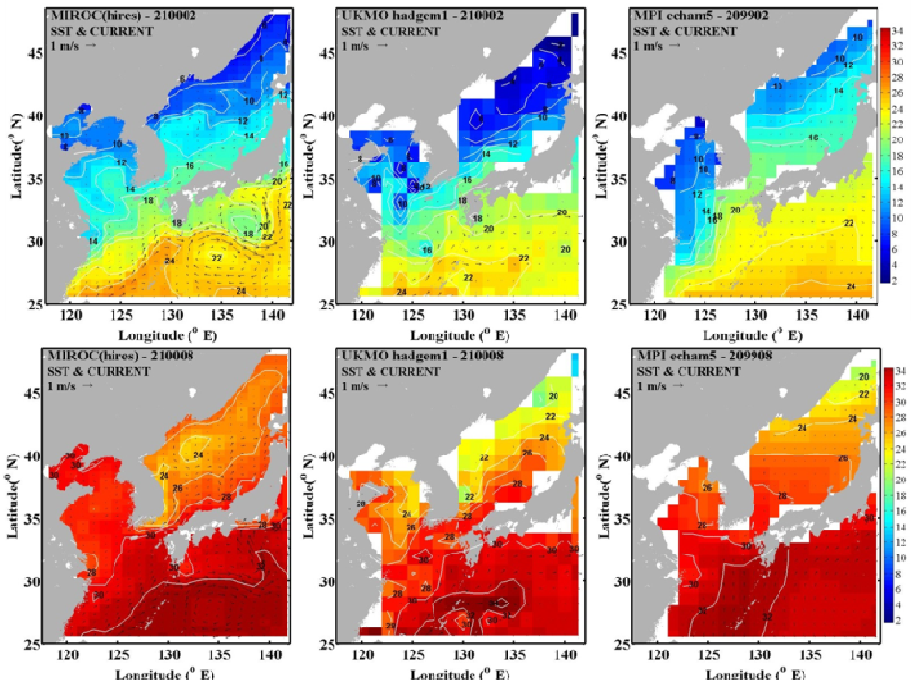

Figure 4. Surface temperature and current of GCMs (left) MIROC, (middle) UKMO, and (right) MPI. Upper panel is for February 2100 and lower panel for August 2100. Color indicates sea surface temperature and vectors surface currents.

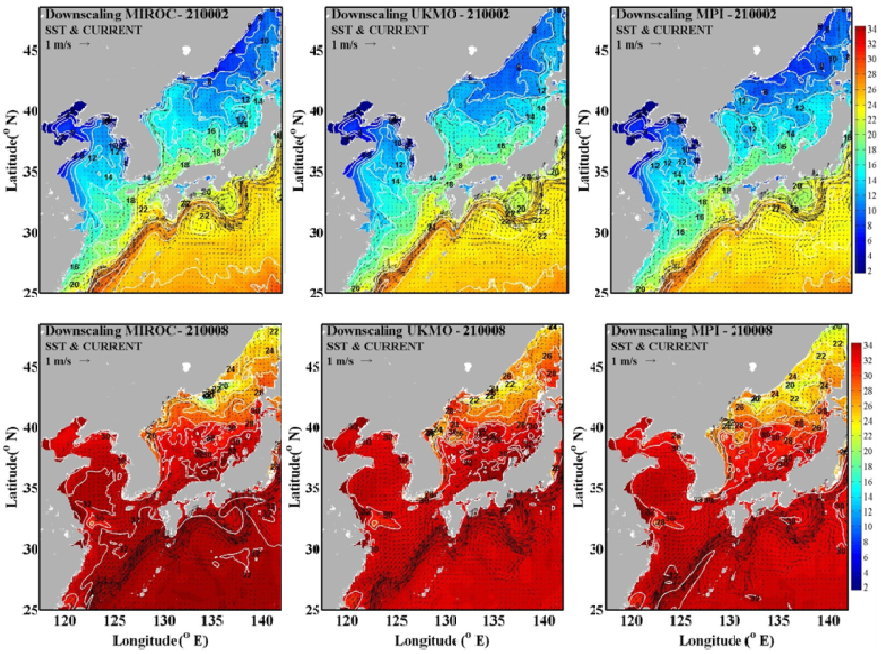

Figure 5. Surface temperature and current using down scaling regional models from GCMs: (left) MIROC, (middle) UKMO, and (right) MPI. Upper panel is for February 2100 and lower panel for August 2100. Color indicates the sea surface temperature and vectors surface currents.

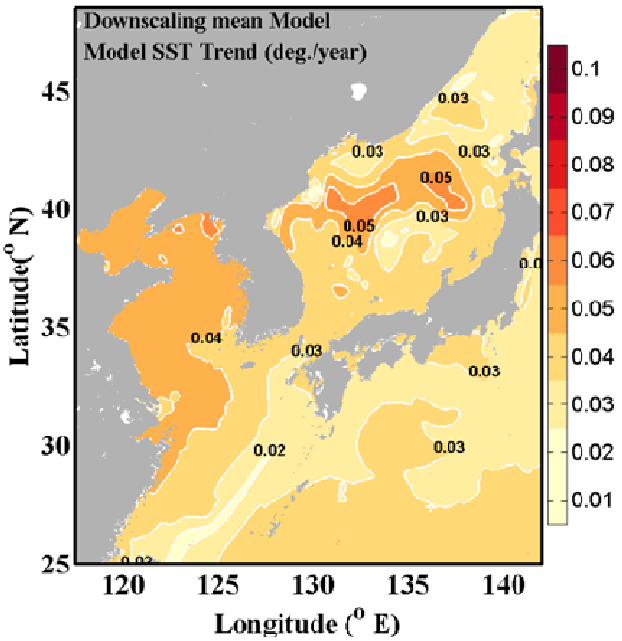

Figure 6. Sea surface temperature warming trend of downscaling simulation from ensemble mean during 2010-2100

Ensemble mean of surface temperature calculated by regional model using GCM forcing was calculated (Figure 6). Downscaling regional climate model result shows relatively rapid temperature increments in the Yellow Sea and northern EJS, and slow increment of temperature along the Kuroshio path.

The GCMs are limited in simulating a regional ocean circulation and transport through narrow straits. After the downscaling, more detailed changes in transport through the Korea Strait, onshore flux and Taiwan Strait were estimated. Especially the volume transport passing the Korea Strait is important because it might determine the distribution of warming trend in the EJS. Understanding the variation of the transport in the Korea Strait is a key factor to identify the circulation and warming in the marginal seas of the Northwest Pacific. Yearly mean volume transport and heat transport through Korea Strait, onshore flux and Taiwan Strait were calculated from the ensemble mean of the downscaling models (Figure 7). Volume transport through the Korea Strait and onshore flux are likely to increase under the global warming condition. However, volume transport of the Taiwan Strait is a little smaller. The variability of Korea Strait volume transport is generally equal to the difference of transport between the Taiwan Strait and Onshore flux variability. This variation was quite similar with the heat transport.

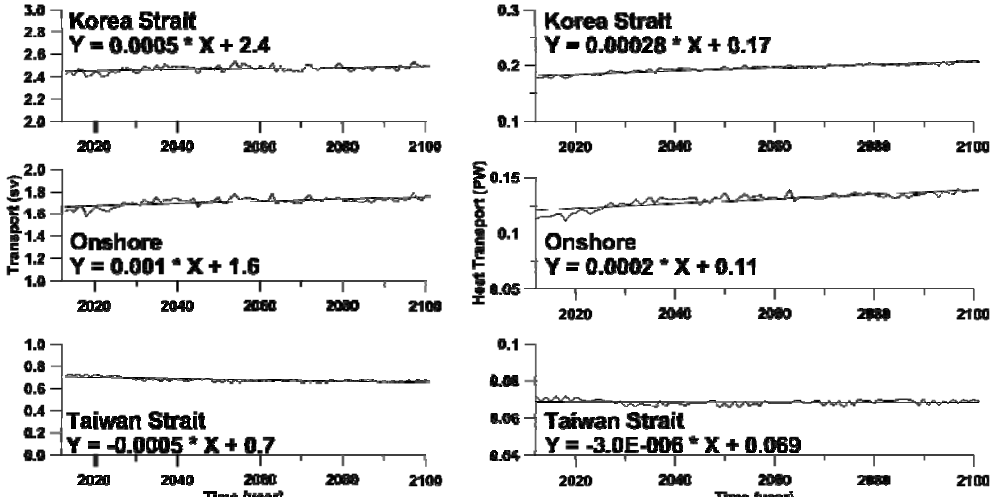

Figure 7. Yearly mean (left) volume transports and (right) heat transport of downscaling simulation from ensemble mean in the Korea Strait (up), Onshore (middle), Taiwan Strait (down).

4. Discussion and Conclusion

The present study seeks to quantify the response of the NWP SST, the Korea Strait, Onshore and Taiwan Strait in particular, to climate change using ocean dynamical downscaling. Downscaling regional climate model reveals detail responses to climate changes in the marginal seas of the NWP, whereas GCMs cannot well resolve coastal phenomena and currents through narrow straits which connect marginal seas. Regional climate model shows relatively rapid temperature increments in the Yellow Sea and northern EJS, and slow increment of temperature along the Kuroshio path. Volume transport and heat transport through the Korea Strait are likely to increase under the global warming condition. The increase may play a significant role in the warming trend of EJS.

REFERENCES

1. Cho, Y.-K., G.-H Seo, C-S Kim, B.-J Choi, DC Shaha. (2013), Role of wind stress in causing maximum transport through the Korea Strait in autumn, J. Mar. Syst., http://dx.doi.org/10.1016/j.jmarsys.2013.02.002
2. Cho, Y.-K. G.-H. Seo, B.-J. Choi, S. Kim, Y. Kim and E.P. Dever, (2009). Connectivity among straits of the Northwest Pacific Marginal Seas. *Journal of Geophysical Research*. 114. 2008JC005218
3. Johns TC, Carnell RE, Crossley JF, Gregory JM, Mitchell JFB, Senior CA, Tett SFB, Wood RA (1997) The second Hadley Centre coupled ocean-atmosphere GCM: model description, spinup and validation. Clim Dyn 13:103–134
4. Kim, C-S, Y-K Cho, B-J Choi, K-T Jung, SH You, (2013),Improving a prediction system for oil spills in the Yellow Sea: Effect of tides on subtidal flow. Mar. Pollut. Bull., http://dx.doi.org/10.1016/j.marpolbul.2012.12.018
5. Kim, K. Y., North, G. R., & Huang, J. (1996). EOFs of one-dimensional cyclostationary time series: Computations, examples, and stochastic modeling. Journal of the atmospheric sciences, 53(7), 1007-1017.
6. K-1 Developers. 2004. K-1 coupled model (MIROC) description. K-1 Technical Report 1, Hasumi H, Emori S (eds.); Center for Climate System research, University of Tokyo: Tokyo, Japan; 34 pp.
7. Roeckner, E., and Coauthors, (2003). The atmospheric general circulation model ECHAM 5. Part I: Model description. MPI Rep. 349, 127 pp.
8. Shchepetkin, A. F., & McWilliams, J. C. (2005). The regional oceanic modeling system (ROMS): a split-explicit, free-surface, topography-following-coordinate oceanic model. Ocean Modelling, 9(4), 347-404..
9. Stock, C. A., and Coauthors, 2011: Onthe use of IPCC-class models to assess the impact of climate on living marine resources. Prog. Oceanogr., 88, 1–27, doi:10.1016/j.pocean.2010.09.001.
10. JONES, R. G.; MURPHY, J. M.; NOGUER, M. Simulation of climate change over europe using a nested regional‐climate model. I: Assessment of control climate, including sensitivity to location of lateral boundaries. *Quarterly Journal of the Royal Meteorological Society*, 1995, 121.526: 1413-1449.

Frontal-scale air-sea interactions along the Gulf Stream simulated by a convection-resolving/eddy-resolving coupled regional climate model

Jen-Shan Hsieh[1], Xiaohui Ma[2,3], Ping Chang[1,2,3] and R. Saravanan[1]

[1]Department of Atmospheric Sciences, Texas A&M University, College Station, TX, USA
[2]Department of Oceanography, Texas A&M University, College Station, TX, USA
[3]Physical Oceanography Laboratory, Ocean University of China, Qingdao, China
E-mail: ping@tamu.edu

The Gulf Stream and Kuroshio provide a significant source of heat and moisture that can potentially affect the overlying atmosphere along the warm SST front. Although the precise air-sea coupling mechanisms along these western boundary regimes are still not well understood, it is anticipated that synoptic-scale winter storms may play a critical role in air-sea exchanges in these region, because the North Atlantic/Pacific storm tracks align with the SST fronts, allowing cold air outbreaks (CAOs) to interact with the underlying warm SST.

To understand and quantify interactions between CAOs and warm SST fronts, we first present a study of boreal winter (NDJFM) latent and sensible surface heat fluxes based on 6-hourly NCEP-CFSR (1979-2009), NCEP-NCAR (1948-2009) and NOAA 20th Century (1910-2009) reanalysis data sets (Ma et al. 2013). Following a recent study by Shaman *et al.* (2010), we separate the winter-season latent and sensible heat flux carried by CAOs from the total winter latent and sensible heat flux and show that extreme surface heat flux events associated with CAOs, defined by daily latent and sensible heat flux greater than 80 percentile value, contribute to more than 80% of the total variance of winter surface turbulent heat fluxes in the Gulf Stream region (GSR) and Kuroshio Extension region (KER) (Fig 1). This result suggests that interannual-to-decadal boreal winter surface turbulent heat flux (THF) variability in these regions is predominately controlled by synoptic-scale winter storm systems. Furthermore, a close relationship between the CAOs over KER and the Pacific Decadal Oscillation (PDO) is found with more frequent occurrence of the high flux events during a positive PDO phase and *vice versa*. A lag-composite analysis shows that the event-day storms have a preferred southeastward propagation path over the North Pacific, potentially contributing to a southward shift of the storm track over the eastern North Pacific basin during a PDO positive phase. In contrast, the nonevent-day storms prefer a northeastward propagation path, consistent with a northward shift of the downstream storm track during a PDO negative phase. These findings suggest that the coupling between synoptic winter storms and warm SST fronts may play a critical role in Northern Hemisphere mid-latitude climate variability.

To shed light on frontal-scale air-sea interactions in western boundary current regimes, we conducted a series of high-resolution coupled ocean-atmosphere model simulations of air-sea

interactions along the Gulf Stream. The coupled model consists of a convection-resolving two-way nested (up to 3km) Weather Research and Forecasting model (WRF) and an eddy-resolving (9km) Regional Ocean Modeling System (ROMS). The use of a convection-resolving and eddy-resolving coupled model over the GSR allows us to directly simulate interactions between synoptic winter storms and mesoscale oceanic eddies along the warm SST front with the use of cumulus parameterizations, reducing uncertainties associated with physics parameterizations.

The high-resolution numerical simulations provide new insights into coupling processes at frontal and meso-scales in the GSR. The model simulates ascending motions along the Gulf Stream front extending from PBL to mid troposphere with an astonishing imprint of Gulf Stream meanders and associated oceanic mesoscale eddies. Figure 2 shows a snapshot of a simulated cyclonic storm passing through the GSR, generating ascending motions that follow the meandering Gulf Stream in the weak of the storm. These events occur episodically and appear to be accompanied by the passage of strong fronts, particularly those associated with cyclonic storm systems. The intermittent atmospheric response to the warm SST suggests that the presence of the warm Gulf Stream front is only a necessary condition, but not a sufficient condition for strong air-sea interactions. To allow oceanic influence to penetrate into the deep atmosphere, a favorable atmospheric environment must exist. We hypothesize that atmospheric fronts associated with cyclonic storms, which can generate strong moisture convergence and ascending motions, are vital to trigger frontal-scale air-sea interactions along the warm Gulf Stream front. We will present observational evidence based on TRMM rainfall measurements to support this hypothesis.

Reference:

1. Shaman, J., R. Samelson, and E. Skyllingstad, 2010: Air-Sea Fluxes Over the Gulf Stream Region: Atmospheric Controls and Trends. *J. Climate*, **23**, 2651-2670.
2. Ma, X., P. Chang, D. Wu, X. Lin, R. Saravanan, L. Wu, 2013: Variability of Winter Extreme Flux Events in the Kuroshio Extension and Gulf Stream Extension Regions. *J. Climate, submitted.*

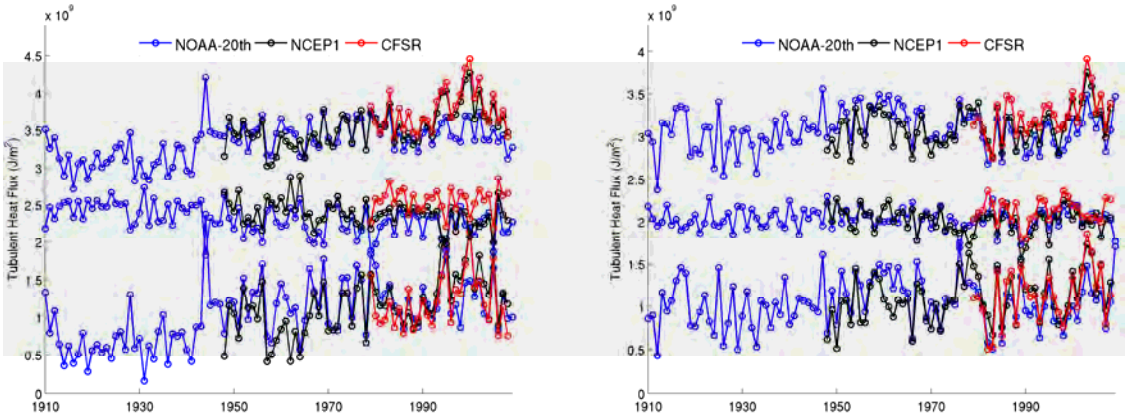

Figure 1. Winter (NDJFM) THF averaged over the KER (32°N-42°N and 140°E-160°E) (left) and GSR (30°N to 42°N, 70°W to 50°W) (right). In each panel, upper curves show the total winter THF, middle curves show the portion of THF during days without extreme storm and lower curves show the portion during extreme storm days. 6-hourly surface heat flux data from NCEP-CFSR (red), NCEP-NCAR Reanalysis (black) and NOAA 20th Century Reanalysis Version 2 (20CRV2) (blue) were used in the analysis. The storm-induced THFs are correlated with the total winter THF at above 0.9 in both the GSR and KER, and explain more than 80.0% of the total THF variance derived from NCEP-CFSR, NCEP-NCAR and 20CRV2.

On the effect of marginal sea SST variability on the North Pacific atmospheric circulation

Hyodae Seo[1], Young-Oh Kwon[1], and Jong-Jing Park[2]

[1]Woods *Hole Oceanographic Institution,* [2]*Kyungpook National University*
E-mail: hseo@whoi.edu

The purpose of this study is to investigate the quasi-steady large-scale response in the Northern Hemisphere atmospheric circulation to the winter SST variability in the semi-enclosed East/Japan Sea (EJS), one of the East Asian marginal seas. These marginal seas are influenced by the variability of the greater western boundary current system of the northwestern Pacific Ocean [e.g., Minato and Kimura 1980]. Located upstream of the climatological storm track, the air-sea interaction in these marginal seas is known particularly important for the downstream large-scale atmospheric circulation [Hirose et al. 2009], an aspect unique to the northwest Pacific. Empirical Orthogonal Function (EOF) analysis of the boreal winter (NDJFMA) EJS SST reveals the basin-wide warming and cooling with peak anomaly up to ±1°C near the subpolar front as its first mode, and the northeast-southwest dipolar pattern of the peak normalized anomaly up to ±0.5°C as the second (Fig. 1). The basin-averaged SST anomalies are moderate, ±0.3°C and 0°C for the first and second mode, respectively.

The scale-interaction of a marginal sea having such interannual to decadal variability with the circumglobal atmospheric circulation is represented by a hemispheric WRF atmospheric model with multiple embedded domains and two-way communications (Fig. 1a), permitting both downscaling effect from the large-scale and the upscaling effect from the marginal sea. Given the significant degree of internal variability in the winter atmosphere and the moderate amplitude SST anomalies typical of the marginal seas, the large ensembles (40) and extended-period (NDNFMA) simulations are used to assure robust signal detection. Climatological conditions lacking influence from the tropical interannual SST variability is imposed at the model's boundaries to aid in the straightforward detection of the mid-latitude atmospheric dynamics that shape the equilibrium response of our interest. Four perturbation experiments forced with dominant modes of SST variability in the EJS (Fig. 1b-f) are compared to otherwise identical CTL simulation driven by the climatological lateral and surface boundary conditions. Both the positive and negative pattern of each of two EOF modes are used as the SST anomaly forcing to examine the symmetric and anti-symmetric component of the equilibrium responses to polarity and amplitude of the EJS SST anomalies.

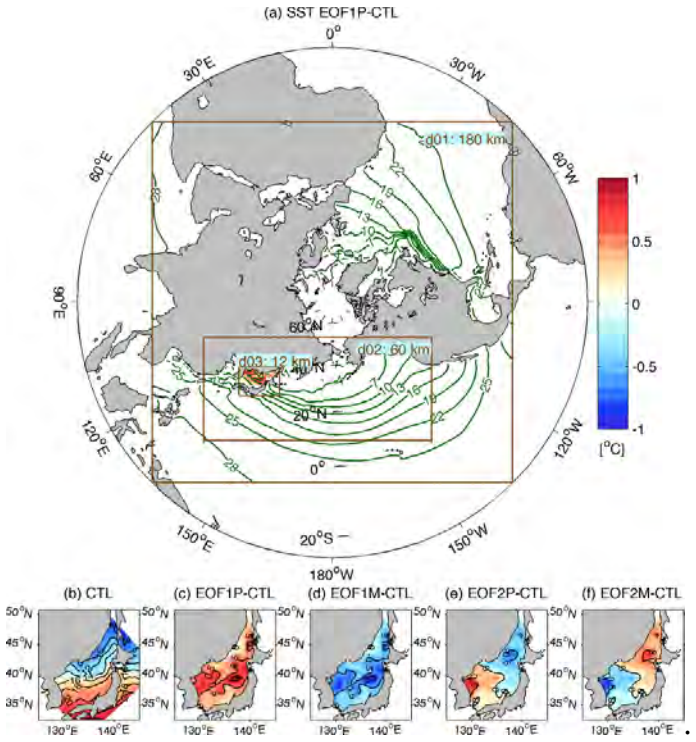

Figure 1. (a) Triple-nested WRF domain. Green contours represent the climatological NDJFMA SST prescribed. (b) shows the NDJFMA mean SST. (c-f) SST anomalies that are used in the subsequent SST perturbation simulations for (c) EOF1P, (d) EOF1M, (e) EOF2P and (f) EOF2M

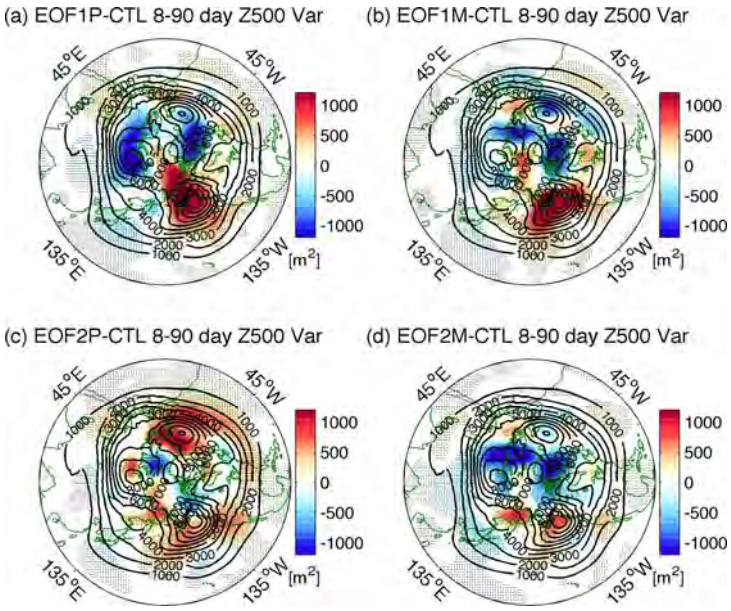

Figure 2. Equilibrium response (NDJFMA averages) in Z500 ([m], shading) overlaid with the mean CTL Z500 (black contours). Dots denote the significant response

The large-scale atmospheric circulation is significantly perturbed by the marginal sea SST anomalies. The evolution of the geopotential height response beyond the EJS for the initial 5 days is weakly baroclinic (not shown), which is rapidly replaced with an equivalent barotropic vertical structure with a hemispheric spatial extent and greater amplitude than the initial one. It is the common response pattern from all four SST perturbation experiments with the center of the ridge response in the Gulf of Alaska. These anomalous ridges have intraseasonal (8-90 days) time-scales (Fig. 2), suggesting that they have characteristics similar to blocking anticyclones.

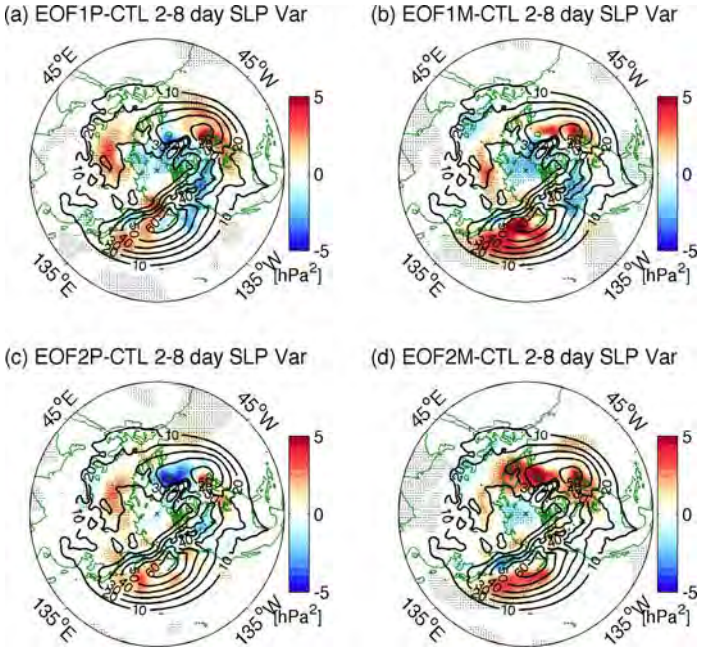

Figure 3. Response in variance of 2-8 day filtered SLP ([hPa^2]) overlaid with the variance of CTL NDJFMA 2-8 day SLP.

It has been suggested that the enhanced low-frequency blocking anticyclones in the downstream of the maximum climatological storm track are accompanied by the increased synoptic transient eddy activity in the upstream, suggestive of synergistic eddy-mean flow interactions [e.g., Nakamura and Wallace, 1990]. It was demonstrated that this enhanced baroclinic wave activity in the upstream is primarily a manifestation of deeper cyclones at the surface. The temporal evolution of the response in synoptic transient baroclinic wave activity and intraseasonal circulation anomalies composited according to the evolution of this blocking anticyclone (Fig. 4) consistently reveals the intensified transient baroclinic wave activity ahead of the emerging block in the Gulf of Alaska.

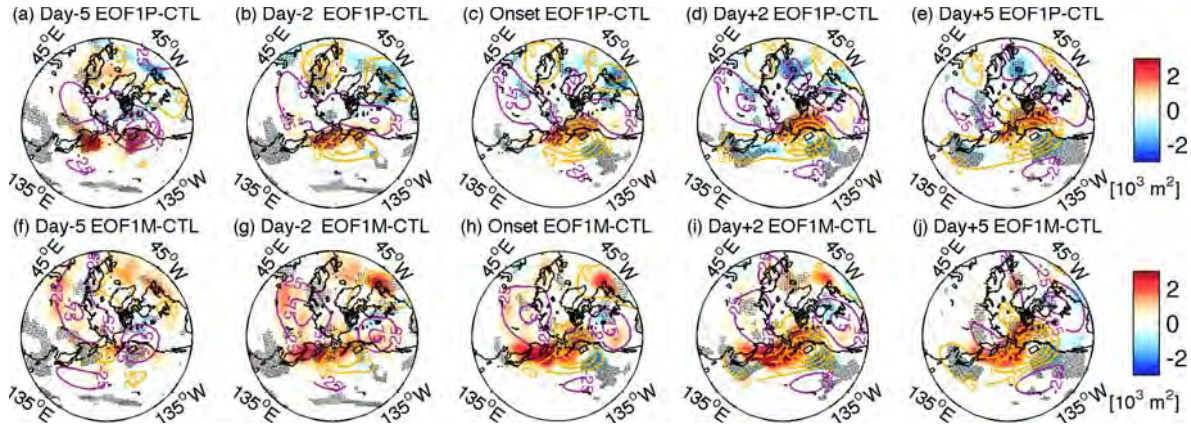

Figure 4. (top) Lead/lag composite evolution of the 2-8 day variance anomalies of the EOF1P-CTL (shading, [m^2]), overlaid with low-frequency (8-90 day) Z500 (contours, [m], CI=50). The composites are with respect to the onset of the positive blocking episode at 50°N, 140°W (block box). Negative (positive) days correspond to prior (after) the onset of blocking. (bottom) as in (top) but for EOF1P-CTL.

The nonlinear equilibrium response is likely associated with eddy vorticity flux turning the direct linear baroclinic response into an equivalent barotropic height tendency [Hoskins and Karoly 1981]. To quantify the role of synoptic eddy vorticity flux, the vertically integrated height tendency (Z_t) due to vorticity flux convergence by synoptic transient eddies is calculated from a quasi-geostrophic potential vorticity equation [e.g., Lau and Nath, 1990], i.e., $Z_t = (f/g)\nabla^{-2}\left[-\nabla(\overline{v'\zeta'})\right]$, where the subscript denotes the partial derivative, the primes represent the synoptic fields and the overbar indicates the winter mean. Z, v and ζ denote the geopotential height, meridional wind and relative vorticity, respectively. The RHS is calculated first at the individual levels and then vertically integrated between 1000 hPa and 100 hPa to form a barotropic geopotential height tendency (LHS). The spatial correspondence of the low-frequency circulation anomalies with the height tendency due to the synoptic eddy vorticity flux convergence in the Gulf of Alaska (Fig. 5) confirms the critical role of the synoptic transient eddy feedback in the maintenance of the low-frequency circulation anomalies.

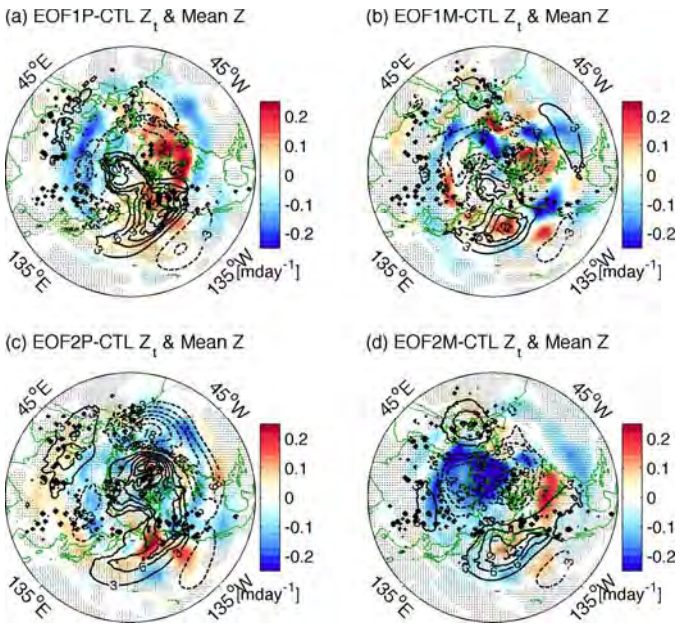

Figure 5. Response in vertically integrated Z_t (shading, [m day^{-1}]) overlaid with the response of vertically integrated geopotential height

Despite the much smaller spatial extent of anomalous surface boundary forcing, a significant large-amplitude response pattern emerges in the downstream circulation. This appears to be related to the fact that EJS is located in the vicinity of the North Pacific storm track, such that small perturbation in SST can effectively trigger a response in storm track variability. The similarity in equilibrium response irrespective of the properties of the diabatic forcing implies that the detailed structure of the marginal sea SST anomalies is perhaps not important in triggering such anomalous ridge non-linear responses, although it is of critical importance in determining regional precipitation pattern (not shown). Furthermore, the non-linear responses are excited with the spatial pattern and time scales closely tied to the internal atmospheric variability found in the control experiment.

The demonstrated sensitivity of the local and remote atmospheric circulation to the SST anomalies in the east Asian marginal seas motivates further studies on the processes leading to the SST anomalies in the East Asian Marginal Seas. The representation of the oceanic variability and air-sea interaction process within these marginal seas, under-represented in the contemporary climate and prediction models, may have far-reaching impact on the potential predictability of the extratropical atmospheric general circulation. In particular, the fact that the variability of the Tsushima Warm Current is associated with the changes in the open ocean large-scale atmospheric circulation and resulting Kuroshio Extension and East China Sea Kuroshio variability suggests a possible two-way coupling between the ocean and atmospheric circulation involving both the North Pacific and its marginal seas. As the ocean-to-atmosphere feedback in the Kuroshio-Oyashio Extension is often emphasized as a key component for the coupled ocean-atmosphere mode of decadal variability in the North Pacific, the impact of the marginal sea ocean-to-atmosphere feedback on the downstream KOE ocean-atmosphere interaction should be clarified further. Detail examination of the dominant paths for winter storms and the air mass modification

along their trajectory over the various parts of the east Asian marginal seas may shed a further light on their impact on the KOE ocean-atmosphere interaction and its role in the coupled atmosphere-ocean mode of decadal variability.

References

1. Hirose, N., K. Nishimura, and M. Yamamoto (2009), Observational evidence of a warm ocean current preceding a winter teleconnection pattern in the northwestern Pacific, Geophys. Res. Lett., 36, L09705
2. Hoskins, B. J., and D. J. Karoly (1981), The steady linear response of a spherical atmosphere to thermal and orographic forcing, J. Atmos. Sci., 38, 1179-1196.
3. Lau, N.-C. M. J. Nath (1990), A General Circulation Model Study of the Atmospheric Response to Extratropical SST Anomalies Observed in 1950-79, J. Clim., 3, 965-989.
4. Minato, S., and R. Kimura (1980), Volume transport of the western boundary current penetrating into a marginal sea, J. Oceanogr. Soc. Jpn., 36, 185 – 195.
5. Nakamura, H., and J. M. Wallace (1990), Observed changes in baroclinic wave activity during the life cycles of low-frequency circulation anomalies, J. Atmos. Sci., 47, 1100-1116.

Can a Regional Ocean-Atmosphere Coupled Model Improve the Simulation of the Interannual Variability of the Western North Pacific Summer Monsoon?

Liwei Zou and Tianjun Zhou

LASG, Institute of Atmospheric Physics, Chinese Academy of Sciences, Beijing, China
E-mail: zoulw@mail.iap.ac.cn

To improve the simulation of the Asian–Australian monsoon (AAM), a Flexible Regional Ocean–Atmosphere–Land System coupled model (FROALS) is developed through the OASIS3.0 coupler. The regionally coupled model consists of two regional atmospheric models and two oceanic components. The atmospheric component of FROALS contains two options. The first is a climate version of the Regional Eta Model (CREM) developed by LASG/IAP, and the other is the Regional Climate Model version 3 (RegCM3) developed by the International Centre for Theoretical Physics (ICTP) in Italy. The oceanic component of FROALS also contains two options. The first is POM2000 oceanic model developed by Princeton University, and the other is the LICOM2.0 Climate Ocean Model developed by LASG/IAP. The initial focus of FROALS is on the western North Pacific summer monsoon. The impacts of local air-sea interaction on the simulation of the interannual variability of the WNPSM are investigated through regionally ocean-atmosphere coupled and uncoupled simulations, with focus on the El Niño decaying summer. Compared with the uncoupled simulation, the regionally coupled simulation exhibits improvements in both the climatology and the interannual variability of rainfall over the WNP in terms of the spatial pattern of dominant mode and the associated temporal variation (Figure 1 and Figure 2). In the El Niño decaying summer, the WNP is dominated by an anomalous anticyclone, less rainfall, and enhanced subsidence, which lead to increases in the downward shortwave radiation flux, thereby warming sea surface temperature (SST) anomalies. Thus, the ocean appears as a slave to atmospheric forcing. In the uncoupled simulation, however, the atmosphere is a slave to oceanic SST forcing, with the warm SST anomalies located over east of the Philippines unrealistically producing excessive rainfall. In the regionally coupled run, the unrealistic positive rainfall anomalies and the associated atmospheric circulations over east of the Philippines are significantly improved, highlighting the importance of air-sea coupling in the simulation of the interannual variability of the WNPSM. One limitation of the model is that the anomalous anticyclone over the WNP is weaker than the observation in both the regionally coupled and the uncoupled simulations. This results from the weaker simulated climatological summer rainfall intensity over the monsoon trough.

References:

1. Zou, L., and T. Zhou, 2011: Sensitivity of a regional ocean-atmosphere coupled model to convection parameterization over western North Pacific. ***J. Geophy. Res.***, 116, D18106, doi: 10.1029/2011JD015844.

2. Zou, L., and T. Zhou, 2012: Development and evaluation of a regional ocean-atmosphere coupled model with focus on the western North Pacific summer monsoon simulation Impacts of different atmospheric components. ***Science China: Earth Science***, 55, 802–815.
3. Zou, L., and T. Zhou, 2013: Can a Regional Ocean-Atmosphere Coupled Model Improve the Simulation of the Interannual Variability of the Western North Pacific Summer Monsoon? ***Journal of Climate***, 26(7), 2353–2367.

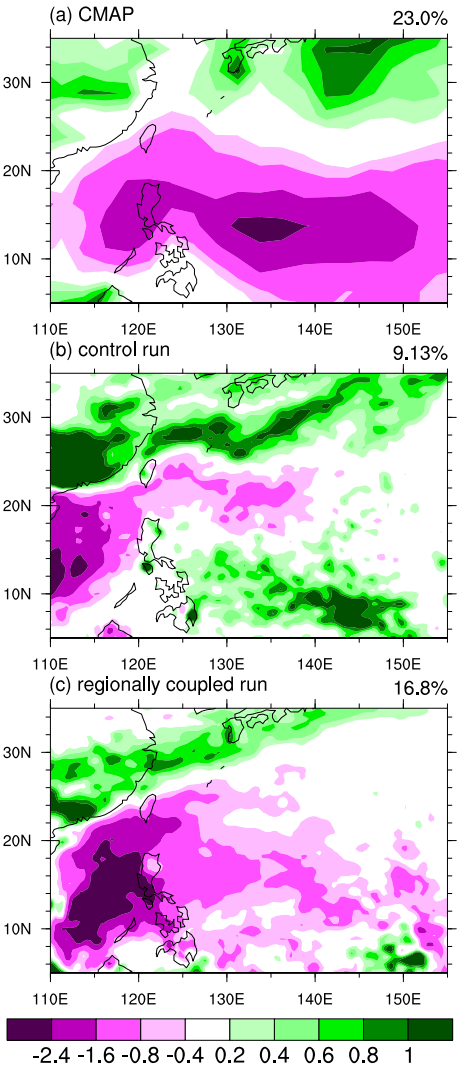

Figure 1. First leading mode of June–July–August (JJA) mean rainfall anomalies during 1983–2007 for (a) observation (Climate Prediction Center Merged Analysis of Precipitation, CMAP) and (c) the regionally coupled run. The third leading mode for (b) the control run is shown. The fractional variance of the Empirical Orthogonal Function (EOF) modes is shown in the top right corner. The pattern correlation coefficients were 0.20 in control run and 0.50 in regionally coupled run.

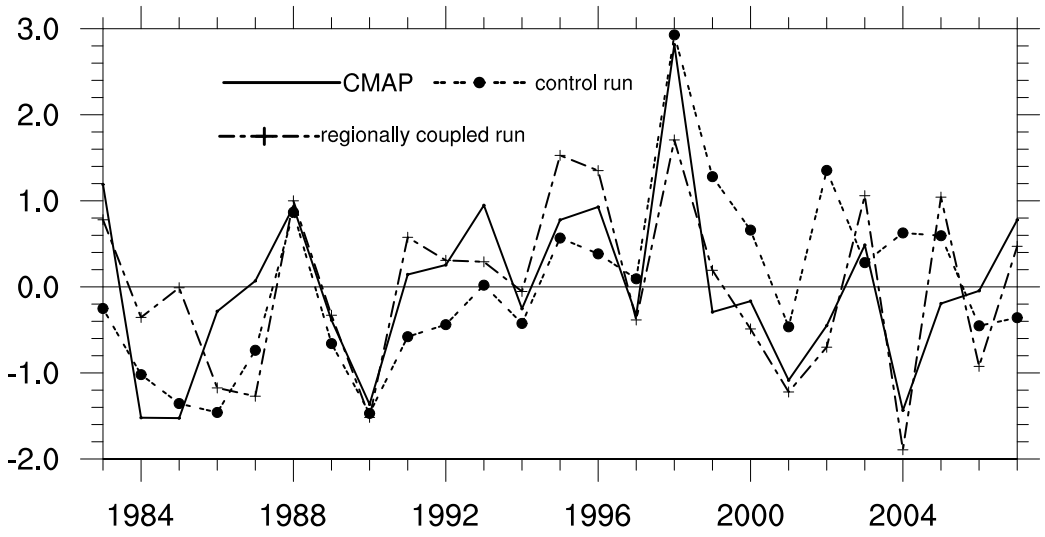

Figure 2. Normalized PC1 corresponding to the leading modes for observation (Climate Prediction Center Merged Analysis of Precipitation, CMAP) and the regionally coupled run. PC3 for the control run is shown. The temporal correlation coefficients were 0.58 in control run and 0.74 in regionally coupled run.

Session III
Climate Variability in the North Pacific

Regional influence of basin-scale wind stress variability via jet-trapped Rossby waves in the western North Pacific

Shoshiro Minobe[1], Yoshi N. Sasaki[1], N. Schneider[2], Yuji Miura[3]

[1]Graduate School of Science, Hokkaido University, Sapporo, Japan
[3]IPRC and department of oceanography, University of Hawaii at Manoa, Honolulu, USA.
[3]Geospatial Information Authority of Japan, Tsukuba, Japan
E-mail: minobe@mail.sci.hokudai.ac.jp

Introduction

One of important question on linkages between large-scale and regional scale variations is how basin-scale atmospheric variability influences local oceanic conditions. A popular theory for an agent that transmits information inputted by atmospheric variability to different regions is a linear Rossby wave propagation. This theory has been employed by a number of studies. Our recent studies (Sasaki Minobe and Schneider 2013 JPO, Sasaki Minobe and Miura submitted to JGR-O), however, suggest that jet-trapped Rossby waves, different kind of Rossby waves from linear long Rossby waves, play important roles. A jet-trapped Rossby wave arises from the potential vorticity conservation as a linear long Rossby wave, but associated with the sharp potential vorticity from of the jet rather than the planetary vorticity gradient. Jet-trapped Rossby waves theoretically propagate just along a thin-jet, whereas a long Rossby wave propagate zonally in regard less of a presence of mean current in a reduced gravity ocean model. The propagation speed of a thin-jet Rossby wave is the same as that of a linear long Rossby wave. In this presentation, we show important features of jet-trapped Rossby waves and their impact on region sea level variability.

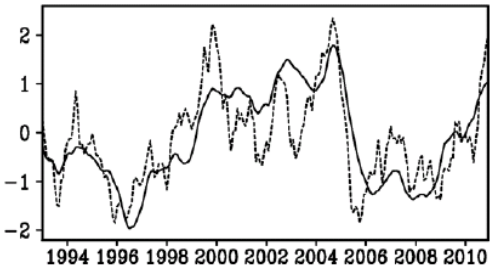

Figure 1. Normalized time series of the first SVD mode between SLAs of satellite data (solid line) and coastal tide-gauge data (dashed line) from January 1993 to December 2010. (Sasaki, Minobe and Miura, submitted to JGR-O)

Results

Jet-trapped Rossby waves propagate along the Kuroshio Extension westward, control Sea-Surface Heights (SSHs) on and around the Kuroshio Extension jet. Although the theory cannot

directly connect the wind forcings and the generation of jet-trapped waves, our analyses suggest that wind-stress anomalies in the central-eastern North Pacific excite jet-trapped Rossby waves with a three-year lag (winds leading). Jet-trapped Rossby waves also exert substantial impacts on sea-level variability along the Japanese coast as shown by Singular Value Decomposition (SVD) analysis between coastal Sea-Level Anomalies (SLAs) and satellite-derived SLAs for a period from 1993 to 2010 (Figs. 1-3). These results can be summarized as a schematic shown in Fig. 4.

Discussion

The jet-trapped Rossby waves in the western North Pacific have important implications on dynamical downscaling utilizing regional numerical models. For a reliable downscaling, a regional model must be able to properly reproduce these waves for the western North Pacific. This means that one needs a wide enough domain for the extent of jets, a fine enough resolution for proper presence of jets, with a long enough integration time for development of jets. For example, a reasonable domain, resolution and integration time may be the whole North Pacific between 25°N and 50°N, 0.1° resolution in latitude and longitude, and 20-30 year integration. This is not a light calculation using a moderate workstation available today. If one wants to conduct downscaling using multiple model outputs, for example, from CMIP5 archives, the computation amounts can be easily increased more than 10 times. Therefore, the importance of jet-trapped Rossby waves implies that reliable dynamical downscaling is still challenging.

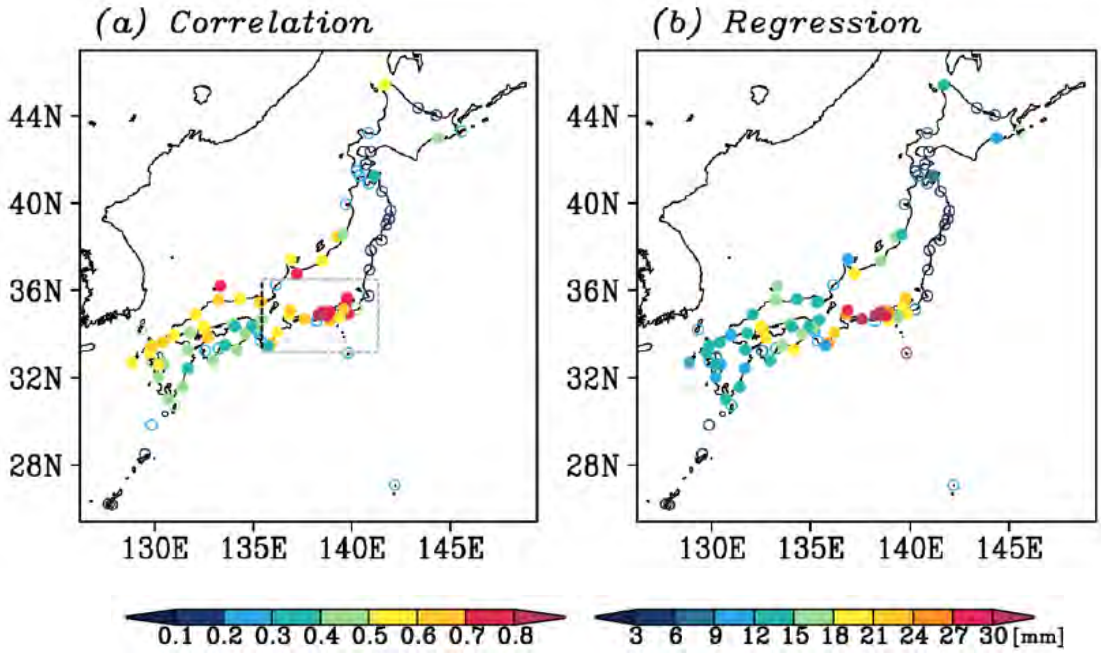

Figure 2. (a) Correlation and (b) regression coefficients of SLAs of the tide-gauge data onto the SVD time series of the satellite data. The closed and open circles denote that the correlation at that point is statistically significant or insignificant, respectively, at the 95% confidence level. (Sasaki, Minobe and Miura, submitted to JGR-O)

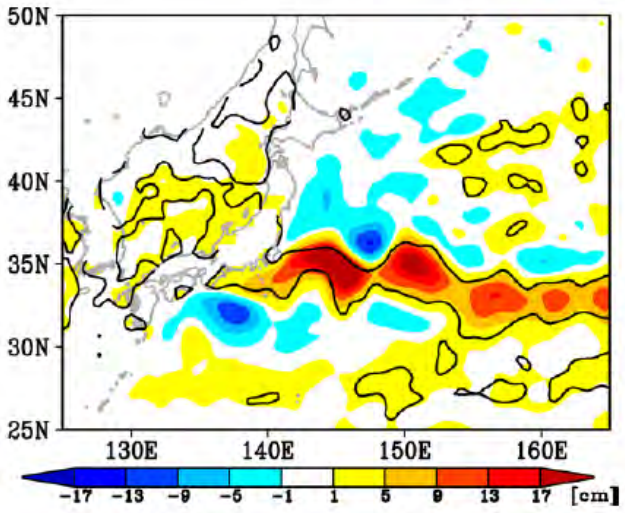

Figure 3. Regression coefficients of SLAs of the satellite data onto SVD time series of the satellite data. The contour indicates the regions where the corresponding correlations are significant at the 95% confidence level. (Sasaki, Minobe and Miura, submitted to JGR-O)

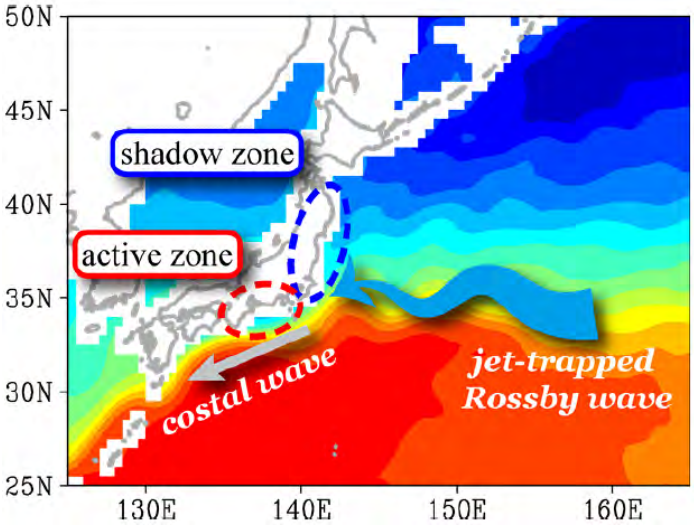

Figure 4. Schematic diagram illustrating the mechanism of the sea level changes along the Japan coast. The blue arrow denotes the incoming jet-trapped Rossby wave, and the gray arrow denotes coastal waves in response to the incoming jet-trapped Rossby wave. (Sasaki, Minobe and Miura, submitted to JGR-O)

Contribution of the Pacific Decadal Oscillation to Global Mean Sea Level Trends

B.D. Hamlington[1], R.R. Leben[2], K.-Y. Kim[3]

[1]*Cooperative Institute for Research in Environmental Sciences, University of Colorado, Boulder, CO, USA*

[2]*Colorado Center for Astrodynamics Research, University of Colorado, Boulder, CO, USA*

[3]*School of Earth and Environment Science, Seoul National University, Korea*

E-mail: hamlingt@colorado.edu

1. Introduction

Sea level is a measurement of considerable interest and importance for the study of climate because it reflects both the mass and heat storage changes in the global ocean. Since 1993, satellite altimetry has provided accurate measurements of sea level. The near-global coverage of the satellite altimeters has improved the understanding of how sea level is changing on regional and global scales [e.g. *Beckley et al.,* 2007*; Cazenave and Nerem,* 2004*; Leuliette et al.*, 2004*; Miller and Douglas,* 2007; *Nerem et al.,* 2010]. The modern altimetry record, however, spans only twenty years, making it difficult to separate longer-term secular trends and accelerations from natural climate variability [*Church et al.,* 2006; 2011*; Hamlington et al.,* 2011a; *Woodworth et al.,* 2009]. Sea level reconstructions provide a possible solution to the difficulties posed by the short altimeter record [*Chambers et al.,* 2002; *Church et al.,* 2004*; Hamlington et al.,* 2011b; *Hamlington et al.,* 2012; *Meyssignac et al.,* 2012]. Historical measurements of sea level from tide gauges extend back as far as the beginning of 19th century. While providing long records, the measurements of tide gauges are generally sparse, particularly before 1950. By combining the dense spatial coverage of satellite altimetry with the long record length of the tide gauges, however, it is possible to examine longer timescale climate signals and assess their contribution to sea level trends both regionally and globally. Furthermore, it is possible to determine whether the current rate and spatial pattern of sea level change are exceptional or instead are simply a recurrence of multi-decadal climate oscillations.

Identifying and explaining signals contributing to regional and global sea level variability and trends has been a frequently studied problem in recent years [e.g. *Bromirski et al.,* 2011*; Chambers et al,* 2012*; Feng et al.,* 2004; *Hamlington et al.,* 2011a; *Merrifield et al.,* 2012]. Through these studies and by subsequently attributing trends, both regionally and globally, to known climate signals, it is possible to improve our understanding of how sea level is rising as a result of the warming climate. Several studies have looked at the relationship between the Pacific Decadal Oscillation (PDO) [*Cummins et al,* 2005; *Mantua et al.,* 1997; 2002] and sea level in the Pacific [e.g. *Merrifield et al.,* 2012], but few have discussed how these signals contribute to trends on a global scale. Here, we analyze the twenty-year trends from sea level reconstructions using a data-driven technique to assess the variability of the spatial pattern of sea level rise over the past sixty years and its relationship to global mean sea level (GMSL). Through this study, we find the PDO has a significant impact on sea level trends not just regionally in the Pacific Ocean

but also globally. The PDO is a decadal-scale pattern of predominantly North Pacific climate variability, with the associated variability commonly tracked by computing the first empirical orthogonal function of the North Pacific sea surface temperature [*Mantua et al.* 1997; 2002]. Here, the PDO contribution to the trend in GMSL over the last twenty years is quantified, and by removing this contribution, a better estimate of the remaining secular trend in sea level can be obtained.

2. PDO Contribution to Sea Level Trends

While the satellite altimetry record alone is too short, it is possible to assess the contribution of decadal and multi-decadal scale signals to GMSL using sea level reconstructions. Twenty-year regional trend maps were computed using a least squares estimate of the trend from the sea level reconstruction dataset created using cyclostationary empirical orthogonal function (CSEOF) bases [*Hamlington et al.*, 2011b; 2012]. Empirical orthogonal functions (EOF) of the twenty-year trend maps from the sea level reconstruction were computed, and the contribution of the first three dominant (i.e. explaining the most variance) EOF modes to the twenty-year trends in GMSL was assessed by averaging the spatial component of the EOF (named the loading vector, following the terminology of *Hamlington et al.* [2011a]) and combining with the temporal component (the principal component time series, again following *Hamlington et al.* [2011a]). By averaging the loading vector globally and then combining this value with the principal component time series, a time series with units of mm/year was obtained that described the variation of the twenty-year GMSL trends associated with each of the first three EOF modes. Prior to computing the EOFs a trend of 1.54 mm/year was removed from the data. This trend is the average trend over the sixty-year sea level reconstruction, and by removing it, the data is centered before computing the EOFs. Furthermore, since we are interested in the twenty-year trends and their temporal variations, the sixty-year trend will just appear as a mean in the results and can thus be removed with significantly impacting the analysis.

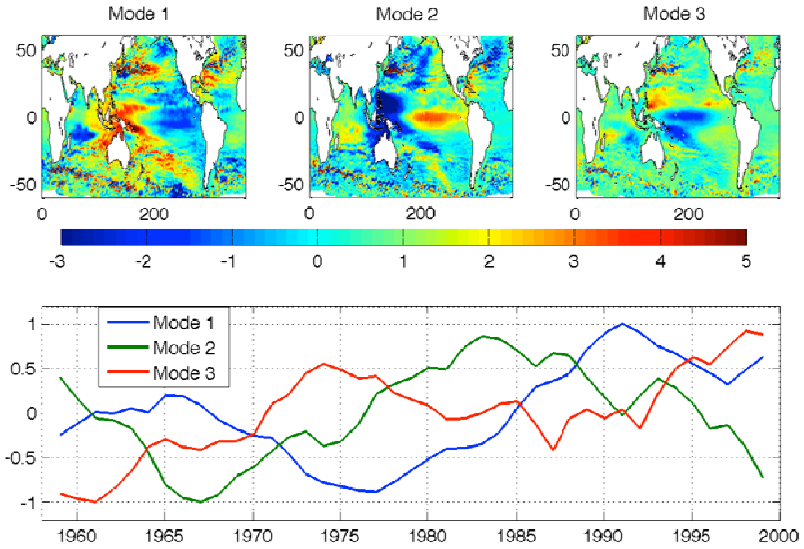

Figure 1. Loading vectors (top) and PCTS (bottom) for the EOF decomposition of twenty-year trends in the CSEOF reconstructed sea level dataset. The first three modes are shown, explaining 84% of the variance in the twenty-year trend patterns

The resulting first three modes from the EOF decomposition are shown in Fig. 1. The variance explained by the trend patterns of the first three EOFs is 41%, 30%, and 13%, respectively, with a total of 84% variance in these first three modes. Having extracted the three dominant twenty-year trend modes from the sea level reconstruction, the important question to be answered is whether any of these patterns (EOF modes) can be attributed to a specific climate process? To evaluate whether any of the modes are related to the PDO and by extension whether changes in the PDO affect the trends in global mean sea level, a twenty-year running trend is calculated for the PDO index, which is derived from sea surface temperature patterns in the north Pacific [*Mantua et al.*, 1997; 2002]. In the top panel of Fig. 2, the resulting twenty-year trends from the PDO index are compared to the first mode from the EOF decomposition. The negative of the PDO trends are shown, since the pattern of mode 1 in the north Pacific corresponds to the negative PDO phase in the PDO index. In addition to the agreement of the spatial patterns of mode 1 and the PDO in the north Pacific (see, for example, *Cummins et al*, [2005], the strong relationship between the two is demonstrated by a correlation of 0.96 between the twenty-year PDO trends and EOF mode 1 of the twenty-year trends from the reconstructed sea level dataset. In other words, the first EOF mode from the decomposition of the twenty-year trends in the sea level reconstruction appears to be closely linked to the PDO, both in terms of its spatial pattern and tempo

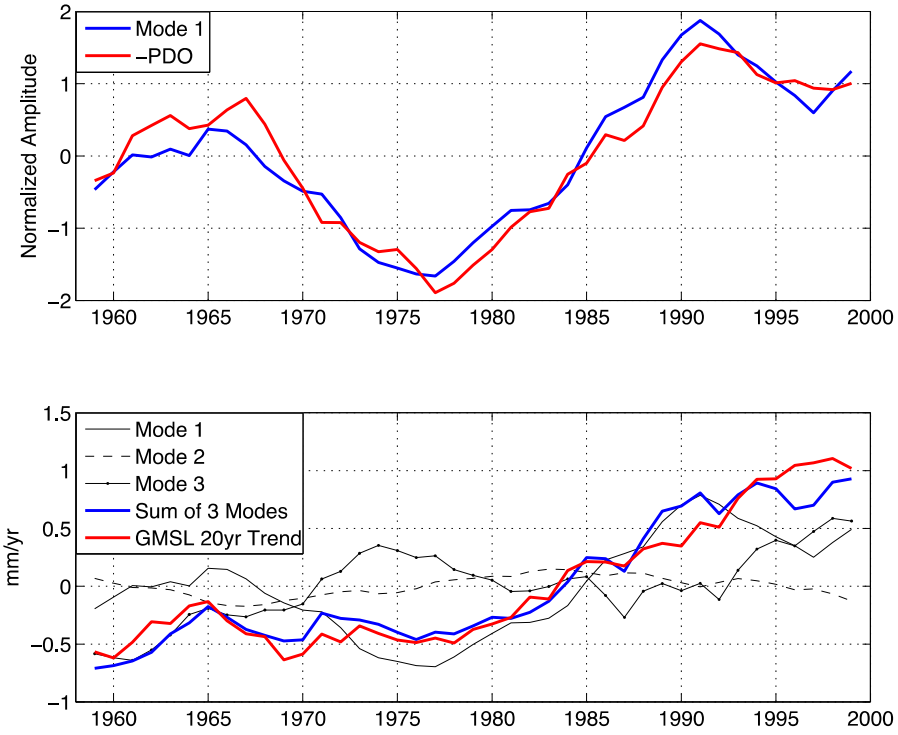

Figure 2. om the CSEOF reconstructed sea level dataset and twenty-year trends computed from the PDO index (shown with opposite sign for direct comparison). Bottom: Contribution of the first three EOF modes to the twenty-year trends in GMSL. For comparison, the twenty-year trends computed directly from the GMSL of reconstructed sea level data are shown with a mean value of 1.54 mm/year removed.

By multiplying the global average of each of the first three EOF loading vectors with the corresponding principal component time series, the contribution of each EOF mode to the twenty-year trends in GMSL can be calculated. In the bottom panel of Fig. 2, the contributions to the GMSL trends of the first three EOF modes are shown, in addition to the twenty-year trends in GMSL from the reconstructed sea level dataset. The average twenty-year trend of 1.54 mm/year (described in detail above) was removed from GMSL in order to make a direct comparison to the EOF decomposition results, which were obtained after this same trend was removed from the data. Given the high correlation (0.96) shown in Fig. 3 and the good agreement between the spatial patterns, the contribution of the PDO to twenty-year trends in GMSL can be evaluated directly from mode 1. Over the last sixty years, mode 1, and by extension the PDO, has contributed significantly to the twenty-year trends in GMSL during certain time periods. During the altimeter time period when the PDO went from generally positive to negative phase (as defined by *Mantua et al.*, [1997; 2002]), the PDO contributed 0.49 ± 0.25 mm/year to the trend in GMSL. From 1968 to 1987 when the PDO went from negative to positive phase, however, the PDO contribution lowered the trend in GMSL by 0.70 ± 0.26 mm/year.

With an estimate of the actual contribution of the PDO to the trends in GMSL, the influence of the PDO can be removed to gain a better understanding of the underlying secular trend in GMSL that may be associated with anthropogenic climate change. For example, during the satellite altimeter time period, removing a trend of 0.49 mm/year would lead to an estimate of the trend in PDO-corrected GMSL closer to 2.7 mm/year as compared to the estimate of 3.2 mm/year [e.g. *Mitchum et al*., 2010] from the total GMSL. The acceleration in the twenty-year trends in GMSL can also be calculated with and without the PDO. With the PDO contribution included, the acceleration of the twenty-year trends in GMSL is found to be 0.04 mm/year^2 over the full record, and an acceleration of approximately 0.08 mm/year^2 since the late 1970s. After removing the PDO contribution, the rate of increase of the twenty-year trends, and hence the acceleration in GMSL becomes 0.02 ± 0.005 mm/year^2 over the full record, and approximately 0.02 ± 0.0121 mm/year^2 since the late 1970s. While unlikely to have a significant impact on accelerations over a longer time period [*Church et al.*, 2011; *Woodworth et al*., 2009] the change in estimated acceleration has important implications for studying the secular trend in the satellite altimetry data as the record gets longer.

3. Discussion and Conclusion

Several studies have looked at the relationship between the PDO and sea level in the Pacific, but this paper is the first to attempt to quantify how much these signals contribute to trends on a global scale. Relying on the data and without making *a priori* assumptions about the climate signals driving sea level change, we have quantified the relationship between the PDO and GMSL trends at the twenty-year time scale. Removing the influence of the PDO from GMSL lowers the trend over the past twenty years and reduces the estimated acceleration in GMSL over the past sixty years, suggesting the observed increase in the underlying secular trend in GMSL is more linear than previously thought. With the short satellite altimeter record alone, it is difficult to assess the contribution of signals like the PDO to decadal – and longer – trends. The short record length combined with the red spectrum of sea level makes it a challenge to separate trends from low frequency climate variability. Leveraging the tide gauge record to create the reconstructed sea level datasets provides the opportunity to extract these climate signals from the sea level record. While questions can be raised regarding how well a tide gauge-based dataset captures GMSL variability, this study demonstrates the value of sea level reconstructions to

provide a plausible estimate of the influence of decadal-scale climate signals on GMSL derived solely from the data, something that has not been done to date. As climate models mature, this first estimate of the PDO influence on GMSL will provide an important check and comparison for model-based estimates. Determining exactly how the PDO affects and contributes to changes in GMSL is the subject of future study, but it is likely to be a combination of thermosteric and mass changes, driven in some part by related precipitation pattern changes. This study focuses primarily on the contribution of the PDO to GMSL, but the same results could be applied to the study of regional sea level trends. Combining the information from the loading vectors and principal component time series seen in Fig. 1 provides an estimate of the regional contribution of the PDO to sea level trends. As seen by the loading vector of mode 1, this has important implications for the study of sea level rise off both the west coast of the United States and throughout the tropical Pacific.

While identifying the climate signals and processes that contribute to regional and global sea level trends can provide insight into past and future sea level change, it is important to keep the magnitude of their contribution in context. The PDO contribution to the twenty-year trends discussed here is a significant fraction of the twenty-year trends in GMSL, but does not reverse the recent positive trend observed during the satellite altimeter time period. The PDO causes acceleration and deceleration in GMSL on decadal timescales, and also appears to have a significant impact on the patterns of regional sea level change. Nevertheless, the underlying secular trend in sea level is larger than the PDO contribution, and over the last sixty years, the twenty-year trends in GMSL have consistently been positive. With the results presented here, however, we can develop a better understanding of this underlying trend, particularly during the satellite altimeter era, and provide insight into how sea level may change in the coming decades.

References

1. Beckley, B.D., Lemoine, F.G., Lutchke, S.B., Ray, R.D., Zelensky, N.P. (2007), A reassessment of global and regional mean sea level trends from TOPEX and Jason-1 altimetry based on revised reference frame and orbits. *Geophys. Res. Lett.* **34**, L14607.
2. Bromirski, P. D., Miller, A.J., Flick, R.E., and Auad, G. (2011), Dynamical suppression of sea level rise along the Pacific Coast of North America: Indications for imminent acceleration. *J. Geophys. Res.* **116**, C07005.
3. Chambers, D.P., Melhaff, C.A., Urban, T.J., Fuji, D., Nerem, R.S. (2002), Low-frequency variations in global mean sea level: 1950-2000. *J. Geophys. Res.* **107**, 3026.
4. Chambers, D., Merrifield, M., and Nerem, R.S., (2012), Is there a 60-year oscillation in global mean sea level? *Geophys. Res. Lett.* **39**, 18.
5. Church, J.A., White, N.J., Coleman, R., Lambeck, K., Mitrovica. J.X. (2004), Estimates of the regional distribution of sea level rise over the 1950-2000 period, *J. Climate* **17**, 2609-2625.
6. Church, J.A., White, N.J. (2006), A 20th century acceleration in global sea level rise, *Geophys. Res. Lett.* **36**, L040608.
7. Church, J.A., White, N.J. (2011), Sea-Level Rise from the Late 19th to the Early 21st Century. *Surveys in Geophysics* **32-4**, 585-602.
8. Cummins, P.F., Lagerloef, G.S.E., Mitchum, G., (2005), A regional index of northeast Pacific variability based on satellite altimeter data, *Geophys. Res. Lett.*, **32**, L17607.
9. Feng, M., Li, Y., and Meyers, G. Multidecadal variations of Fremantle sea level: Footprint of climate variability in the tropical Pacific, (2004) *Geophys. Res. Lett*. **31**, L16302.

10. Hamlington, B.D., Leben, R.R., Nerem, R.S., Kim, K.-Y. (2011a) The effect of signal-to-noise ratio on the study of sea level trends, *J. Climate* **24**, 1396-1408.
11. Hamlington, B.D., Leben, R.R., Nerem, R.S., Han, W., Kim, K.-Y. (2011b), Reconstruction sea level using cyclostationary empirical orthogonal functions. *J. Geophys. Res.*, **116**, C12015.
12. Hamlington, B. D., Leben, R.R., and Kim, K.-Y. (2012), Improving sea level reconstructions using non-sea level measurements, *J. Geophys. Res*. **117**, C10025.
13. Mantua, N.J., Hare, S.R., Zhang, Y., Wallace, J.M., Francis, R.C. (1997), A Pacific interdecadal climate oscillation with impacts on salmon production, *Bull. of Amer. Meteor. Soc.*, **78,** 1069-1079.
14. Mantua, N. J., and Hare, S. R., The Pacific Decadal Oscillation, *J. Oceanogr*. (2002), **58**, 35–44.
15. Merrifield, M.A., Thompson, P., and Lander, M.. (2012) Multidecadal sea level anomalies and trends in the western tropical Pacific. *Geophys. Res. Lett.* **39**, 13.
16. Meyssignac B., Salas y Melia, D., Becker, M., Llovel, W., Cazenave, A. (2012), Tropical Pacific spatial trend patterns in observed sea level: internal variability and/or anthropogenic signature? *Clim. Past*, **8**, 787-802.
17. Mitchum, G. T., Nerem, R.S., Merrifield, M.A., and Gehrels, W.R. (2010), *Modern sea-level-change estimates, in Understanding Sea-level Rise and Variability*, edited by J. A. Church et al., pp. 122–142, (Wiley, Chichester, U. K.).
18. Woodworth, P. L., White, N. J., Jevrejeva, S., Holgate, S.J., Church, J. A., Gehrels, W. R. (2009), Evidence for the accelerations of sea level on multi-decade and century timescales, *Int. J. Climatol*. 29, 777–789.

MULTI-DECADAL VARIABILITY OF SEA LEVEL IN THE SOUTHEAST AND NORTHEAST ASIAN SEAS

R. R. Leben[1], M. Strassburg[1], B. D. Hamlington[2], and K.-Y. Kim[3]

[1]Colorado Center for Astrodynamics Research, Department of Aerospace Engineering Sciences, University of Colorado, Boulder, CO, USA

[2]Cooperative Institute for Research in Environmental Sciences, University of Colorado, Boulder, CO, USA

[3]School of Earth and Environmental Science, Seoul National University, Korea

E-mail: Robert.Leben@Colorado.edu

Since 1993 satellite altimetry has provided accurate measurements of sea level with near-global coverage. These measurements have led to the first definitive estimates of global mean sea level (GMSL) rise and have improved our understanding of how sea level is changing regionally at decadal timescales. The relatively short satellite record, however, does little to answer the question of how the current state of the ocean compares to previous states. Tide gauges, on the other hand, have measured sea level over the last 200 years, with some records extending back to 1807. While providing long records, the spatial resolution of tide gauges is poor, making studies of GMSL and the large-scale patterns of low-frequency ocean variability difficult. Sea level reconstruction overcomes the respective shortcomings of the tide gauge and satellite altimetry records by combining the shorter nearly global coverage provided by satellite altimetry with the longer sparsely distributed tide gauge dataset. In this paper and the presentation to follow, multi-decadal sea level variability in 25 East Asian seas is examined using satellite altimetry and sea level reconstructions to better understand long-term sea level trends in this region.

For this study, the 25 East Asian seas are grouped into two regions: Southeast Asian Seas (SEAS) and Northeast Asian Seas (NEAS) as identified in Figure 1 and Table 1. The bodies of water (seas, straits, and gulfs) are defined according to the Limits of the Ocean and Seas published in 1953 (IHO, 1953). The SEAS span the largest archipelago in the global ocean, the Indonesian Archipelago, and provide a complex oceanic pathway connecting the Pacific and Indian Oceans. This is the only existing tropical interoceanic through flow and is comprised of a total of 20 seas according to the Limits of the Ocean and Seas published in 1953. SEAS regional sea level trends are some of the highest observed in the modern satellite altimeter record that now spans two decades. In contrast, the five Pacific marginal seas that comprise the NEAS of the western North Pacific exhibit significantly lower trend rates with the exception of the Philippine Sea. Initial comparisons of global sea level reconstructions find that 17-year sea level trends over the past 60 years exhibit good agreement in areas and at times of strong signal to noise associated with multi-decadal variability forced by low frequency variations in Pacific trade winds.

Data and Methods

Satellite Altimetry: The satellite altimeter dataset used in this study was produced and distributed by the Archiving, Validation, and Interpretation of Satellite Oceanographic (AVISO;

http://www.aviso.oceanobs.com/) as part of the Ssalto ground-processing segment.

Tide Gauge Data: Each reconstruction uses tide gauge data from the Permanent Service for Mean Sea Level (PSMSL; http://www.psmsl.org). PSMSL supplies a wide range of tide gauge data, but availability depends highly on the region and timeframe in question. Each reconstruction uses different tide gauge editing and selection criteria depending on time-series length, data gaps, area weighting, etc., which can be found in the respective references for each of the reconstructions.

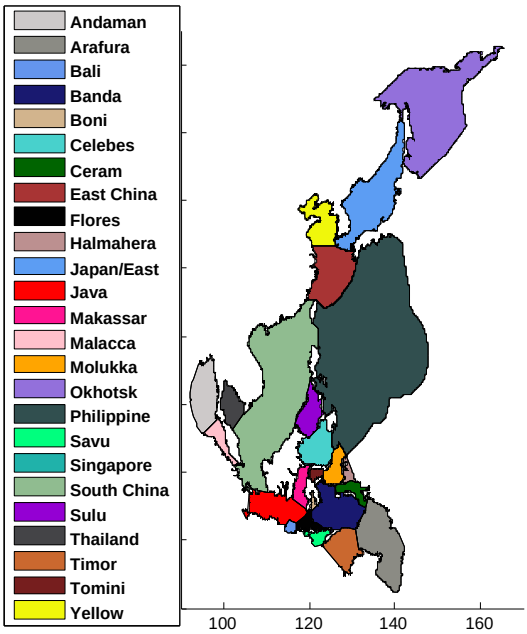

Figure 1. The 25 bodies of water (seas, straits, and gulfs) defined in the *Limits of the Ocean and Seas* (IHO, 1953) for the Southeast Asian Seas and Northeast Asian Seas regions.

Table 1.

SEAS Region	NEAS Region
Andaman Sea	East China Sea
Arafura Sea	Japan/East Sea
Bali Sea	Sea of Okhotsk
Banda Sea	Philippine Sea
Gulf of Boni	Yellow Sea
Celebes Sea	
Ceram Sea	
Flores Sea	
Halamahera Sea	
Java Sea	
Makassar Strait	
Strait of Malacca	
Molukka Sea	
Savu Sea	
Singapore Strait	
South China Sea	
Sulu Sea	
Gulf of Thailand	
Timor Sea	
Tomini Sea	

Sea Level Reconstruction Methods: Sea level reconstructions are created by decomposing the training data into basis functions to explain the variance in the original data, in this case satellite data and/or ocean model data. These basis functions are then interpolated back in time using in-situ measurements. Sea level measurements from tide gauges were used for the four univariate reconstructions. For the bivariate reconstruction, both sea level measurements from tide gauges and shipboard measurements of sea surface temperature measurements were used.

The reconstructions compared in this study use two basis function decomposition methods: empirical orthogonal functions (EOFs) and cyclostationary empirical orthogonal functions (CSEOFs). Both methods decompose the training data set into loading vectors (LVs) and principal component time series (PCTS) for each individual mode. CSEOFs differ from EOFs, however, in that time dependence is included in the LVs, allowing extraction of non-stationary cyclostationary signals. A subset of modes are selected, which explain a portion of the variance in the original training dataset, and are interpolated back in time to determine the PCTS to create the

reconstructed sea level dataset. The five different sea level reconstructions used in this analysis vary based on the training data and reconstruction method used. A summary of basic information concerning each reconstruction is given in Table 1. More details on the reconstruction are given in the following sections; however, if more desired information is desired about please refer to the corresponding references.

Table 1. Summary information on sea level reconstructions.

Reference	Abbreviation	Basis Function Method	Training Data	Observation Data	Training Data Time Period	Number of Modes	Percent of Variance	Reconstructed Time Period
Church et al. (2004); Church and White (2006)	*CW*	EOFs	Custom 1° by 1° monthly SSHA maps derived from TOPEX/ Poseidon, Jason-1 and OSTM (Jason-2) 10-day repeat altimetry using a 300 km Gaussian filter	Monthly sea level observations from 426 PSMSL tide gauge stations	1993 through 2009	20	84% of the non-annual signal	1950 through 2009
Hamlington, Leben, and Kim (2012)	*HLK/TG*	CSEOFs	AVISO weekly SSHA subsampled to ½° by ½°	Monthly sea level from 377 PSMSL tide gauge stations upsampled to weekly observations	1993 through 2009	11	80% of the non-annual signal	1900 through 2009
Hamlington, Leben, and Kim (2012)	*HLK/BV*	CSEOFs	•AVISO weekly SSHA subsampled to ½° by ½° •NOAA OISST weekly 1° by 1° SST	•Monthly sea level from 377 PSMSL tide gauge stations •Monthly SST ICOADS 2° by 2° observations	1993 through 2009	11	80% of the non-annual signal	1900 through 2009
Meyssignac et al. (2011)	*M/Alt*	EOFs	Annual Averaged AVISO	Annual averaged sea level observations from 91 PSMSL tide gauge stations	1993 through 2009	15	~ 88%	1950 through 2009
Meyssignac et al. (2011)	*M/Mean*	EOFs	•Annual Averaged AVISO •SODA 2.0 •Drakkar/NEMO model	Annual averaged sea level observations from 91 PSMSL tide gauge stations	1958 through 2007	15	??	1950 through 2009

Hamlington et al. (2012) Bivariate Reconstruction (HLK/BV): In addition to AVISO and PSMSL data, HLK/BV uses sea surface temperature (SST) to create a bivariate reconstruction. The SST training data are Optimal Interpolation SST (OISST; http://www.esrl.noaa.gov/psd/data/) data from NOAA, which are a combination of *in situ* and satellite measurements, as well as simulated SST values near sea ice. The historical *in situ* SST data come from the International Comprehensive Ocean-Atmosphere Data Set (ICOADS; http://icoads.noaa.gov/), averaged to a 2°x2° grid. To utilize SST measurements for a sea level reconstruction, basis functions of the SST training data are computed using CSEOFs. These basis functions are then transformed to have the same principal component time series as the SSH basis functions. The transformed SST basis functions and the SSH basis functions are then interpolated with the respective in-situ measurements to form a bivariate reconstruction. See Hamlington et al. (2012) for more details.

Church and White (2011) Reconstruction (CW): CW utilizes a custom satellite altimetry training dataset, merging and filtering data from 3 different satellites, as described in Church et al. (2004).

Meyssignac et al. (2011) Mean Reconstruction (M/Mean): Meyssignac et al. (2011) created a mean sea level reconstruction dataset by averaged a satellite altimetry reconstruction with two model data reconstructions made using sea level from the SODA 2.0 and Drakkar/NEMO ocean models.

Estimating Sea Level Trends: Prior to any comparison, each reconstruction was annually averaged for consistency. Linear trends were computed over a variety of time spans and the uncertainty of each trends was found using standard error estimates for the trend term determined from the least squares linear regression.

SEAS and NEAS Region Definition and Analysis: For the regional analyses, the region was subdivided into 25 separate bodies of water (Figure 1) defined according to the *Limits of the Oceans and Seas* (1953). For each dataset, all points within a given boundary were averaged to determine an areal averaged mean time series for each body of water. If no points were present in a dataset, the nearest point was used. Linear trends were found after the calculation of averages within each body of water.

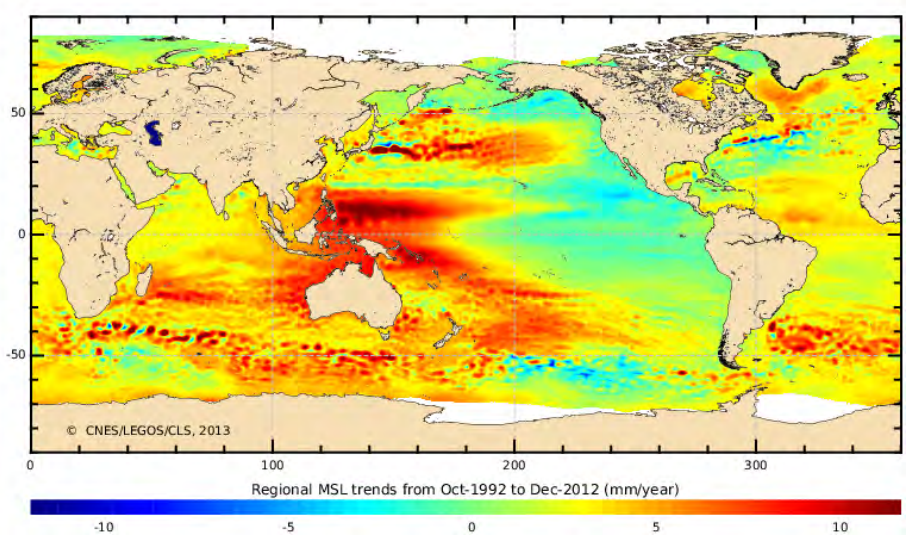

Figure 2. Regional sea level trends computed from October 1992 to December 2012 using AVISO SSH data.
(http://www.aviso.oceanobs.com/fileadmin/images/news/indic/msl/MSL_Map_MERGED_Global_IB_RWT_NoGIA_Adjust.png)

RESULTS: Sea level trends in the SEAS region and Philippine Sea are some of the largest observed in the modern satellite altimeter record (Figure 2). To highlight the trend variability over the longest time scale observed by the current 20-year record of altimeter observations, we performed the following global analysis of the sea level reconstructions:

1. Formed annual averaged full resolution spatial maps over the 1950 through 2009 record from each reconstructed sea level datasets.
2. Calculated 17-year linear trends from the annual averaged maps to produce 44 17-year trend maps from 1958 through 2001.

3. Performed a lagged correlation analysis (present versus past) of the 17-year trend time series for each sea level reconstruction dataset.

There are roughly three extrema in the lagged correlation analysis of the global sea level reconstructions associated with three independent 17-year time periods in the 60-year record: 1959-1975, 1976-1992, and 1993-2009, i.e. 17-year trends centered on 1967, 1984 and 2001, respectively. The 1959-1975 time period was correlated with 1993-2009 record, showing strong regional sea level trends in the western Pacific like those observed during the satellite record. Trends over 1959-1975 and 1993-2009 time periods are anti-correlated with the trend over 1976-1992. During 1976-1992 much smaller sea level trends were observed in the western Pacific than during the satellite record (Figure 3). NEAS trends tend to be attenuated and out of phase with SEASs trends (Figure 4).

What is driving these changes in the western Pacific sea level? Merrifield et al. (2012) showed that, when detrended by GMSL, the western Pacific sea level is correlated with the low-frequency variability of the Pacific Decadal Oscillation (PDO) and the Southern Oscillation Index (SOI). Thus, the equatorial sea level signal may be driven by anomalous decadal wind variability over the Pacific, which propagates through the SEAS archipelago along oceanic waveguides. Forcing of the sea level trends in the SEAS and NEAS regions, and possible coupling between the two regions will be discussed further in the presentation.

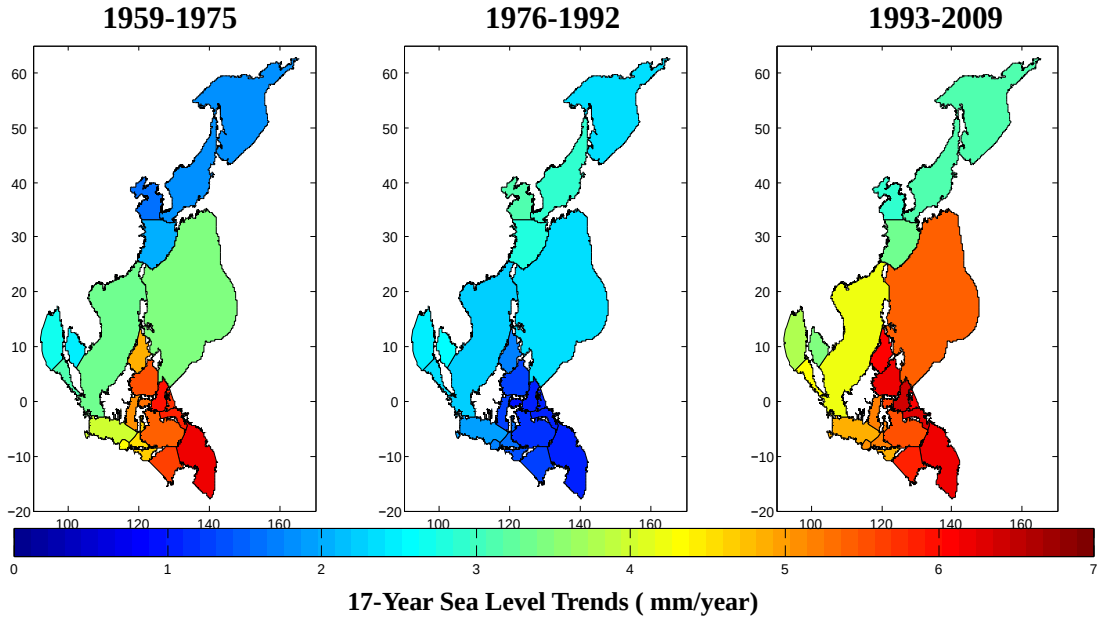

Figure 3. Sea level trends computed from the annual average in each of the Southeast and Northeast Asian Seas over the (a) 1959-1975, (b) 1976-1992, and (c) 1993-2009 time periods from the bivariate sea level reconstruction (Hamlington et al., 2012).

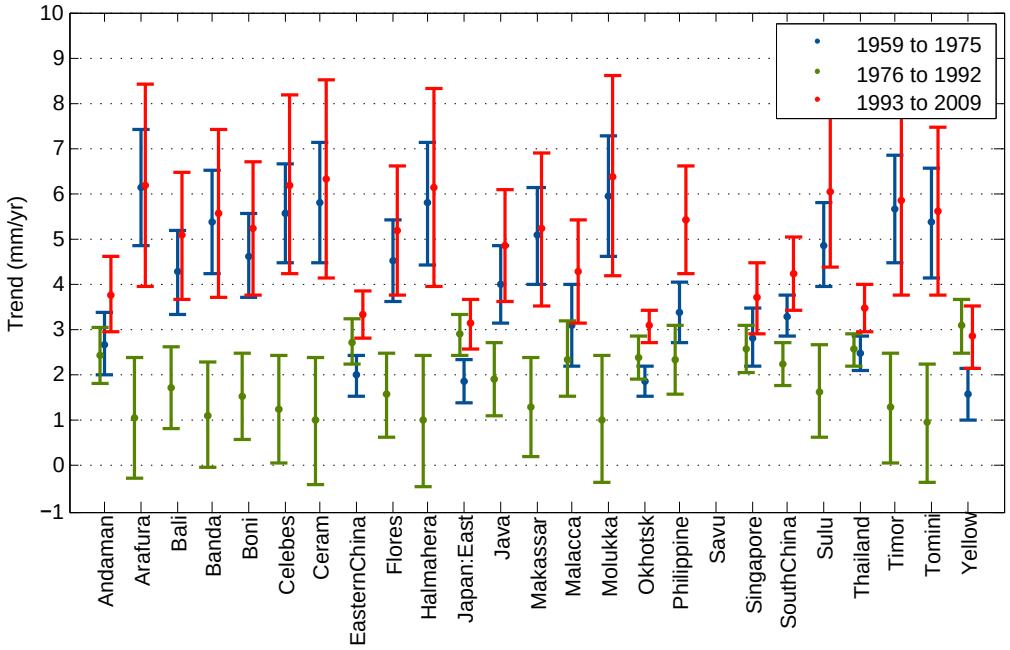

Figure 4. Average sea level trends with error bars for 25 east Asian seas over the 17-year time periods 1959-1975, 1976-1992, and 1993-2009 time from the bivariate sea level reconstruction (Hamlington et al., 2012).

References:

1. Church, J. A., N. J. White, R. Coleman, K. Layback, J. X. Mitrovica. (2004), Estimates of the regional distribution of sea level rise over the 1950-2000 period, J. Clim, 17: 2609-2625.
2. Church, J. A., N. J. White. (2011), Sea-Level Rise from the Late 19th to the Early 21st Century. Surv. in Geophys, 32-4:585-602.
3. Hamlington, B. D., R. R. Leben, R. S. Nerem, W. Han, and K.-Y. Kim, (2011). Reconstructing sea level using cyclostationary empirical orthogonal functions, *J. Geophys. Res.*, **116**, C12015, doi:10.1029/2011JC007529.
4. Hamlington, B. D., Leben, R. R., Kim, K.-Y., (2012). Improving Sea Level Reconstructions Using Non-Sea Level Measurements, *J. Geophys. Res., 117*, C10025, doi:10.1029/2012JC008277.
5. International Hydrographic Organization, (1953). Limits of Oceans and Seas, 3rd edition. Special Publication No. 23 (S-23). Monaco: International Hydrographic Organization.
6. Merrifield, M. A., P. R. Thompson, M. Lander (2012). Multidecadal sea level anomalies and trends in the western tropical Pacific. Geophys. Res. Lett., 39, L13602, doi:10.1029/2012GL052032
7. Meyssignac, B., M. Becker, W. Llovel, A. Cazenave, (2012). Assessment of twodimensional past sea level reconstructions over 1950-2009 based on tide-gauge data and different input sea level grids. Surv. Geophys. Doi:10.1007/s10712-011-9171-x.

Poster Session

A Comparison of Surface Turbulent Heat Fluxes over the East Asian Marginal Seas

Uk-Jae Jung, Kyung-Il Chang

School of Earth Environmental Science, Seoul National University, Korea
E-mail: ujjung@curl.snu.ac.kr

1. INTRODUCTION

Surface turbulent fluxes (THFs, latent heat flux (LHF) + sensible heat flux (SHF)) play a significant role in the exchange of heat and moisture at the air-sea interface, and an accurate determination of mean and variability of THFs is pivotal for understanding and modeling air-sea interactions (Taylor et al. 2001). The knowledge of THFs at the air sea interface is required to provide thermal boundary conditions to climate models and also to evaluate results from coupled ocean-atmosphere models. THFs are usually calculated by using bulk formula, which is parameterization of heat flux based upon Monin-Obukhov similarity theory (Fairall et al. 2003), with bulk variables such as skin sea surface temperature, wind at 10 m height , and specific humidity, and air temperature at 2 m height. These bulk variables are usually derived from reanalysis products.

There are several reanalysis products currently available. These products have different characteristics in terms of, for example, temporal and spatial resolution/coverage, observation data, parameterization, and data assimilation system (Zeng et al. 1998, Brunke et al. 2003). Lucas et al. (2008) tested model response to the thermal boundary conditions and addressed that even a very small perturbation of the atmospheric variables can lead to significant changes in THFs calculated and the ocean properties. Taylor et al. (2001) also reported that a flux of 10 Wm^{-2} over one year would, if stored in the top 500 m of the ocean, heat that entire layer by about 0.15C. Therefore, accuracy of flux should be a few Wm^{-2}. A number of comparative studies was carried out in specific regions of ocean (e.g., Taylor et al. 2001), and the results indicate that the factors causing the discrepancies among the reanalysis products can be different at different regions, indeed they are characterized by quite strong regional biases (Sun et al. 2003). Hence, even if successful validation was made in one place, careful evaluation is needed to quantify reanalysis flux data at new regions of interest. The purpose of this study is to compare TH**F**s derived from the reanalysis products with those calculated using bulk formula and variables measured from ocean flux buoys over the East Asian marginal seas. (Fig. 1)

2. DATA AND MATCHUP PROCESSING

The five reanalysis products and one blended product used in this comparison include the National Center for Environmental Prediction Reanalysis 1 and 2 (NCEP1 and NCEP2), the Climate Forecast System Reanalysis (CFSR), the Modern-Era Retrospective Analysis for Research and Applications (MEERRA), the ECMWF interim reanalysis (ERA-I), and the Objectively Analyzed Air-Sea Heat Fluxes (OAFlux). The observation data used here is listed on Table 1.

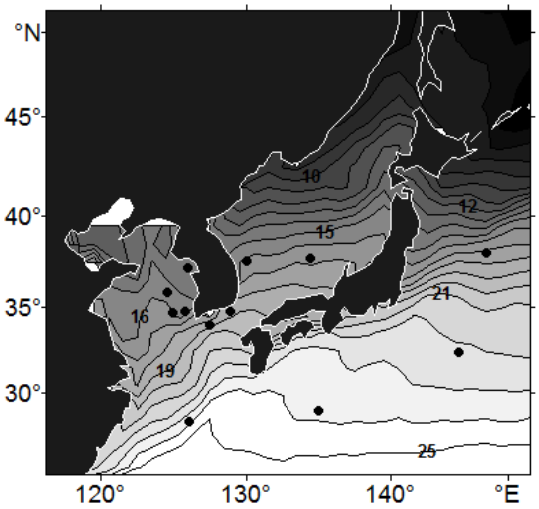

Figure 1. Buoy locations. The background field is the annual mean surface temperature (°C) field from the ICOADS during 1979-2012.

Table 1. Locations of buoy stations used in the study, and the period of observation at each station.

Expt	ID	Period	Location	Times	Lon° (E) / Lat° (N)
KMA	K1	1996. 7. -	Yellow Sea	1 hourly	126.02/37.24
	K2	1996. 7. -	Yellow Sea		125.78/34.79
	K3	1998. 1. -	East China Sea		127.47/34.00
	K4	1998. 5. -	East China Sea		128.90/34.77
	K5	2005. 5. -	East/Japan Sea		130.00/37.54
KIOST	K6	2008.0. -	Yellow Sea	1 hourly	124.58/35.86
JMA	J1	1978. - 2000	East/Japan Sea	3 hourly	134.38/37.75
	J2	1982. - 2000	Kuroshio		135.00/29.00
	J3	1978. - 2000	Kuroshio		126.08/28.33
JKEO	J4	2008. 2. -	Kuroshio Expention	10 min, 2min	144.60/32.40
KEO	J5	2004. 6. -	Kuroshio Expention		146.50/38.00

A fair comparison of fluxes based on data from buoys and products is not an easy task because of the different specification of products and buoys. Data intervals of the reanalysis products are different, varying from hourly (MERRA) to daily (OAFlux), and the buoy data at all stations are obtained on an interval shorter than an hour (Table 1). NCEP1 and NCEP2 provides the coarse-resolution instantaneous values at synoptic times (00, 06, 12 and 18 GMT). For the consistency, all variables from other products and buoys are subsampled at every 6 hours, the same as those NCEP products, and then averaged on daily basis. Then the daily variables are used for calculating the THFs with COARE algorithm.

Buoy measurement is a single point data while reanalysis products are gridded data with spatial resolutions of 0.313°~2.5°. Thus caution should be exercised in evaluating the reanalysis products at buoy locations close to coast due to an inclusion of land surface to grids of reanalysis

products. We mainly use bilinear interpolation with the surrounding four grid points around the buoy position. However, in some cases, for example, the reanalysis products having low spatial resolution such as NCEP1 and NCEP2, we just chose the nearest grid point to the buoy locations (K1, K2, K3, and K4) to avoid using land contaminated grid point data: fortunately, the distances between any two points are not far, less than a few km.

Bulk variables observed at different heights are adjusted to the reference height (10 m for wind, 2 m for specific humidity (qa) and air temperature (Ta)) for comparison with products via COARE algorithm. The specific humidity at buoy stations (qa) is determined from the measured relative humidity and Ta using TeTen's formula. However, relative humidity is not available for J1, J2 and J3. Instead, 2m dew point temperature (Td) and Ta and pressure are used to calculate qa following Henderson Sellers (1984). ERA-I also provide not qa but Td.

3. COMPARISONS OF LATENT HEAT FLUXES

In this section we just show the results of comparison of LHFs from products and buoy. More details on the comparison of SHFs will be presented in the workshop.

a. Product-to-product comparison of mean LHFs

Figure 2 shows climatological annual mean LHFs in the East Asian marginal seas obtained from NCEP1, NCEP2, ERA_I, CFSR, MERRA, and OAFlux. The most striking and compelling feature in Fig. 2 is that reanalysis products tend to reveal similar spatial patterns in THFs; all products agree that the East Asian marginal seas loses THFs to the atmosphere on the annual mean basis and the maximum loss occurs along the path of the Kuroshio. However, the magnitude of long-term mean heat losses differs significantly with NCEP2 being the greatest heat loss and MERRA being the smallest heat loss. The difference is as large as 80 Wm^{-2} in the center of the maximum heat loss around 30N°.

b. Validation with in situ flux measurements

We calculate the record-length mean LHF and SHF (referred to as buoy flux hereafter, BF) based on all available daily mean time series of those fluxes at each buoy station (see Table 1). Assuming the LHFs calculated with the COARE algorithm using buoy data are true values, BFs are then compared with mean fluxes from the 6 reanalysis products (referred to as RFs hereafter) at grid points nearest to the buoy station during the same time span. In calculating the THFs, BF is calculated using the COARE algorithm and RFs are calculated using either the bulk formula in the original reanalysis products, or the COARE algorithm.

Figure 3 shows the comparisons of LHFs at buoy locations. The filled symbols in Fig. 3 indicate that the magnitude of mean biases between BF and RF vary depending on stations and selected reanalysis product. At four sites (K1- K4), closer to the land boundary within 45 km and located on shallower depths (<~80 m), all of the reanalysis products except MERRA tend to overestimate LHF. Especially, the reanalysis products significantly overestimate the LHF at sites K2 and K3; the mean biases at K2 and K3 are in the range of 24~58 Wm^{-2} and 24~83 Wm^{-2}, respectively, which correspond to 56~135% at K2 and 31~103% at K3 of the mean LHFs based on buoy observations. This comparison poses a significant problem for the use of reanalysis products in coastal region.

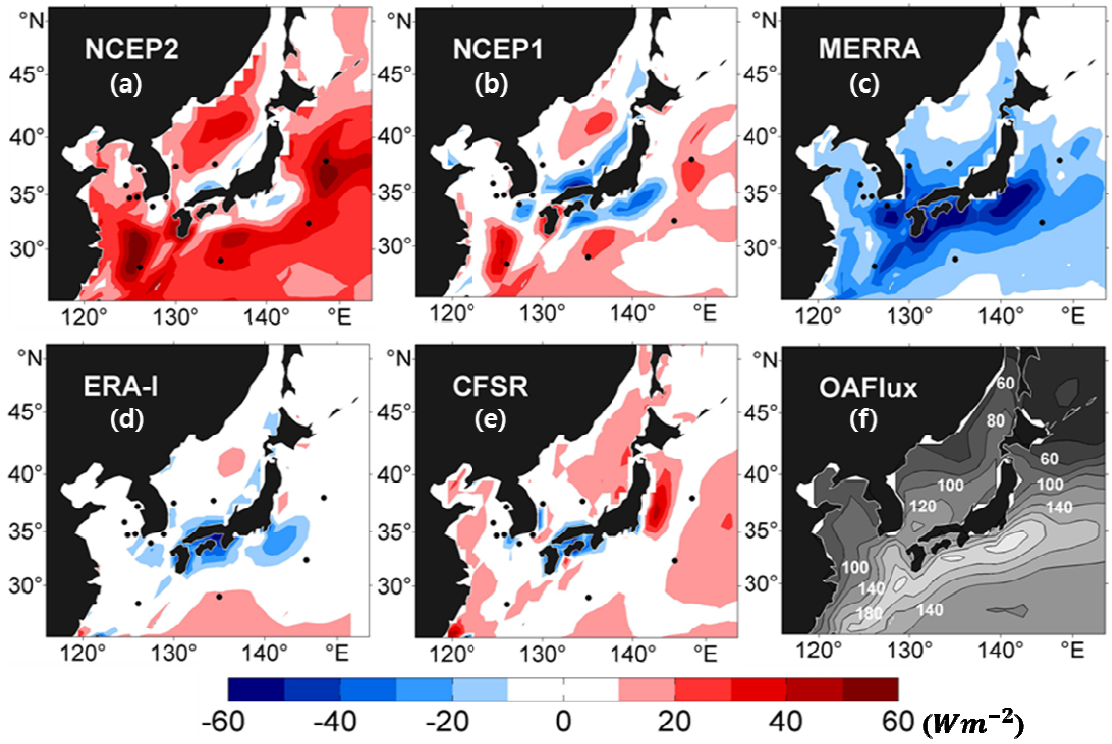

Figure 2. Climatological annual mean LHFs in the East Asian marginal seas derived from (a) NCEP2, (b) NCPE1, (c) MERRA, (d) ERA-I, (e) CFSR, (f) OAFlux. The values from (a)-(e) is shown as the mean difference of LHF for each product from the LHF for OAflux, so positive values from (a) to (e) mean the overestimation of heat loss by LHF as compared to that from OAFlux. Contour interval is $10Wm^{-2}$. Positive value in (f) OAFlux denotes the oceanic heat loss. All fields are averaged over the 1989-2009 period.

As different flux algorithms are adopted in different products, the biases could be due to the difference in the algorithms as well as biases in variables. We recalculate LHFs using the COARE algorithm with bulk variables from all reanalysis products. In Fig.3 hollow figures shows the difference in LHFs between those from reanalysis products recalculated using the COARE algorithm and derived from buoy data also with the COARE algorithm. Large positive mean biases in NCEP1, NCEP2 are drastically reduced when the fluxes are recalculated with the COARE algorithm; the mean bias of the LHF is reduced by 25.6~ 47.4 W/m^2 for NCEP1, 26.3~46.2 W/m^2 for NCEP2, and 17.4~17.3 W/m^2 for MERRA. In case of CFSR and ERA-I, the difference with buoy flux are also changed, but to lesser extents (0.2~11.5 W/m^2) as compared to those for NCEP1, NCEP2, and MERRA, indicative of relatively insensitive to the change in the algorithm for those products. Although the mean biases based on recalculated fluxes are reduced at coastal sites, they are still large, up to 114% (ERA-I at K3) of the mean fluxes based on buoy data. It suggests the important contribution of the variable caused bias to the large mean bias.

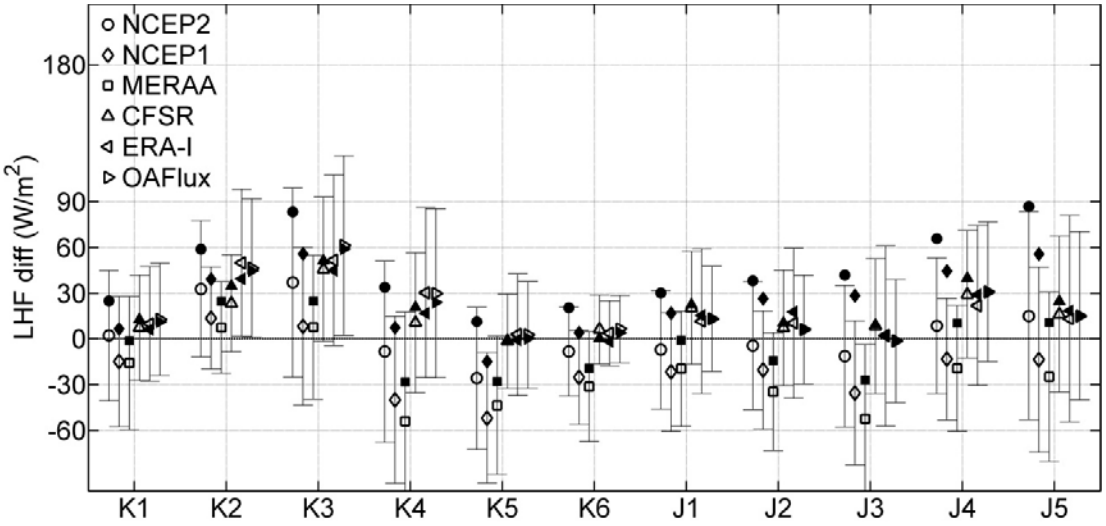

Figure 3. Differences in long-term mean LHFs calculated from the products and buoy data. The filled symbols are the LHF differences based on original algorithms in each product. The open symbols are the LHF differences when the LHFs are all calculated using the COARE algorithm with capped lines to indicate standard deviations. Positive value in y-axis means the reanalysis products overestimate the fluxes (greater heat loss) as compared to the fluxes based on the buoy observation.

Figure 4 shows the Taylor diagram (Taylor, 2001) used to illustrate the relative accuracy of demeaned temporal variability amongst products as compared to BF: The product that agrees well with observed variability will lie nearest the point marked 'REF', representing the observation, on the x-axis.

ERA-Interim, CFSR, and OAFlux, are very close each other on Taylor diagram, indicating that their temporal variations are similar. For those products, the distances to the point REF are short in most cases in Fig. 4(a) while NCEP1 and NCEP2 lie remote from REF at all sites, indicating the temporal variation of LHFs from NCEP1 and NCEP2 is much different from those based on buoy observation. In spite of large mean biases shown in Fig. 3, all products have high correlation coefficients (0.83~0.97) with even higher correlation (>0.95) at offshore sites. The relative amplitude of variation (denoted by standard deviation, STD, in the figure), however, varies from place to place but with a common feature in terms of the magnitude of amplitude amongst products. For NCEP1 and NCEP2, the amplitudes of the variation are much larger than those from other products at all sites. On the other hand, the flux calculated from MERRA has the smallest standard deviation at all sites, and the standard deviations of the LH fluxes from the other products (ERA-Interim, CFSR and OAFlux) lie between MERRA and NCPE1. In Fig. 4(b), Characteristics of temporal variability of recalculated LHFs change little in terms of the amplitude of variation and RMS difference except for NCEP1 and NCEP2, which show reduced amplitude and RMS difference and now become comparable to the observation. MERRA showed a large reduction in LHFs when its algorithm switches to the COARE, but shows relatively small changes in the characteristics of temporal variability.

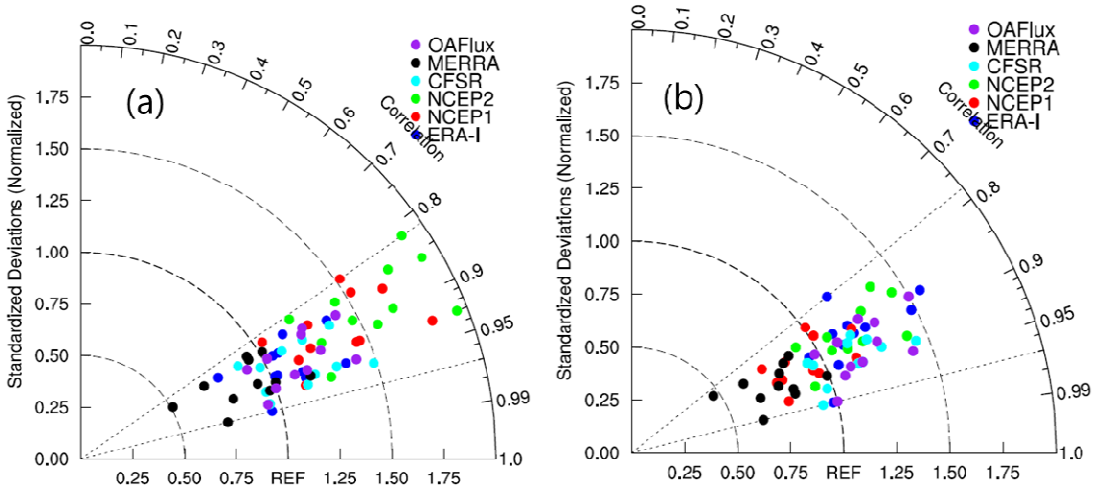

Figure 4. Taylor diagram of LHFs from six reanalysis products at all buoy stations. The radial co-ordinate gives the magnitude of total standard deviation, normalized by the observed value, and the angular co-ordinate gives the correlation with observations. The distance between the observed point (REF) and any product's point is proportional to the centered RMS error. All second-order statistics are calculated using the demeaned time series ((a) is for the original products and (b) is for the recalculated products).

4. CONCLUSIONS

LHFs are calculated with COARE3.0 algorithm based on meteorological variables acquired from ocean buoy observations, and compared with those fluxes archived from five reanalysis products (ERA-Interim, NCEP1, NCEP2, CFSR, MERRA) and objectively analyzed data (OAflux) to validate their performance. The difference in long-term mean LHFs based on reanalysis products and buoy data is generally large for all products, and the degree of mean biases depends on locations. According to Brunke's (2011) study covering broad areas, the total biases and variable-caused biases are relatively small (-3 ~ 20W/m^2 for total LH biases, -13~8 W/$m^2$for variable caused biases). He also addressed that most of LHF biases from the products used here, except MERRA, come from algorithm biases. In contrast to their results, the variable caused biases are main contributor to large mean biases in LHFs for the locations chosen in this study.

REFERENCES

1. Brunke, M. A., C. W. Fairall, X. Zeng, L. Eymard, and J. A. Curry (2003), Which bulk aerodynamic algorithms are least problematic in computing ocean surface turbulent fluxes?, J. Clim., 16, 619–635.
2. Brunke, Michael A., Zhuo Wang, Xubin Zeng, Michael Bosilovich, Chung-Lin Shie, (2011), An Assessment of the Uncertainties in Ocean Surface Turbulent Fluxes in 11 Reanalysis, Satellite-Derived, and Combined Global Datasets. J. Climate, 24, 5469–5493.
3. Fairall, C. W., E. F. Bradley, J. E. Hare, A. A. Grachev, and J. B. Edson (2003), Bulk parameterization of air-sea fluxes: Updates and verification for the COARE algorithm, J. Clim., 16, 571–591.

4. Lucas, M. A., N. Ayoub, T. Penduff, B. Barnier, P. de Mey (2008), Stochastic study of the temperature response of the upper ocean to uncertainties in the atmospheric forcing in an OGCM, Ocean Modelling., 20, 90-113
5. Sun, B., L. Yu, and R. A. Weller (2003), Comparisons of surface meteorology and turbulent heat fluxes over the Atlantic: NWP model analyses versus moored buoy observations, J. Clim., 16, 679– 695.
6. Taylor, P. K. (2001), Intercomparison and validation of ocean–atmosphere energy flux fields. Final report of the Joint WCRP/SCOR Working Group on Air–Sea Fluxes (SCOR Working Group 110). Geneva, Switzerland, World Meteorological Organization, World Climate Research Programme, 306pp. (WCRP Report, WCRP-112 (WMO/TD-1036))
7. Taylor, K. E. (2001), Summarizing multiple aspects of model performance in a single diagram. J. Geophys. Res., 106, 7183-7192 (also see PCMDI Report 55, http://wwwpcmdi. llnl.gov/publications/ab55.html)
8. Zeng, X., M. Zhao, and R. E. Dickinson (1998), Intercomparison of bulk aerodynamic algorithms for the computation of sea surface fluxes using TOGA COARE and TAO data. J. Climate, 11, 2628–2644.

Development of Regional and Coastal Operational Hydrodynamic/Wave Forecasting System in Korea

Do-Youn Kim[1], Sang-Kwon Hyun[1], Seong-Min Lee[1], Jang-Won Seo[2], Sung-Hyup You[2]

[1]ARA Consulting & Technology, Incheon 406-840, Korea
[2]Marine Meteorology Division, Observation Infrastructure Bureau, KMA, Seoul 156-720, Korea
E-mail: Doyoun71@gmail.com

1. Introduction

A need of high-resolution and characterized information at the open ocean, coastal sea and port/harbor has been increased to support marine activity, fisheries, port management and maritime safety. Nationwide interests and technology improvement have required the development of a highly accurate ocean forecasting system with a high-resolution grid.

Ocean modeling for the coastal area around Korea is still challenging because the oceanographic systems along the Korean coast depend on its variety and complexity. Specifically, the western and southern coasts are characterized with large tidal ranges and complex coastline whereas the eastern coast is characterized with small tide, large wave height and deep water depth.

The Korea Meteorological Administration (KMA) has been developing operational forecasting system for the coastal and harbor areas of Korea using the MOdelo HIDrodinâmico (MOHID) modeling system and the Simulating Waves Nearshore (SWAN) wave model. The 72 hours hydrodynamic information (sea surface elevation, currents, temperature, and salinity) is predicted once a day and the 72 hours wave information (wave height, period and direction) is predicted twice a day. This system produce hourly sea surface height(SSH), sea surface temperature(SST), sea surface salinity(SSS), current speed and vector, wave height, wave direction, wave period distribution and time series. The main advantage of this system is to use a downscaling approach which incorporates the circulation, sea temperature, salinity and wave from large scales to regional and/or local scales effectively.

Downscaling of a global/regional to the regional/local scale is mainly related to the initial state of the coastal model and its lateral open boundary conditions. The first challenge of downscaling is to generate initial conditions by interpolating ocean 3D/2D fields provided by a larger coarse resolution model into a smaller fine resolution model. The second challenge is to use these forcing fields as the open boundary conditions for the smaller/downscaled model.

2. Method and Data

This forecasting system has 2 regional domains: Level 1(1/6˚), Level 2(1/12˚) and 3 local (coastal and port) scale domains (Level 3-1/48˚, Level 4-1/192˚ and Level 5-1/768˚). For hydrodynamic model, Level 1 is a 2D-barotropic domain forced by NAO global tide solution

only and Level 2 is a fully 3D-baroclinic domain with the initial and boundary conditions obtained from a global circulation model and meteorological surface forcing. Open boundary conditions for Level 3, Level 4 and Level 5 are individually forced from their higher levels and the surface boundary conditions are directly forced into individual levels. The wave model has depth-integrated 2D domains (Level 2 to Level 5 with surface wind and lateral wave height, direction and period.

The General Bathymetry Chart of the Ocean (GEBCO), KorBathy30s(Seo, 2008) and the Korea Hydrographic and Oceanographic Administration (KHOA) digital charts were used to generate model coastline and Bathymetry. The bathymetry in model grids was manually interpolated with detailed nautical chart along the Korean coastline.

As initial conditions, the hydrodynamic system uses daily oceanic currents, sea surface height (SSH), temperature and salinity of the HYbrid Coordinate Ocean Model (HYCOM) global data. And also the hydrodynamic model uses HYCOM data as boundary conditions with relaxation scheme. In the wave system, initial condition is "0" (cold start) and boundary conditions are specified with KMA's operational wave model (WAVEWATCH-Ⅲ, 1/12˚ horizontal grid) results. After first run, the hydrodynamic and wave model uses the previous results as initial condition (hot start).

For the meteorological surface forcing, the hydrodynamic model uses the KMA's Unified Model (UM, 1/12˚ horizontal grid) outputs, i.e., wind velocity, air temperature, mean sea level pressure, solar radiation, relative humidity and downward long wave radiation. These data are provided every 3 hours for 72 hours.

The major river (ChangJiang, HuangHo, Han, Imjin, YeSung, Nakdong river) discharge at the Korean and Chinese coast, which affect mass transport of the Yellow Sea, has been considered with climatological monthly averaged discharge (Kwon et al., 2011, Park et al., 2008).

3. Results

The predicted hydrodynamic and wave model results compared with buoy and sea level observation data. The time series comparison between the predicted and observed wave height, SSH, SST are showed in Figure 3. The model results have comparatively good agreement with the observation. And parts of model results are showed in Figure 4 ~ 6.

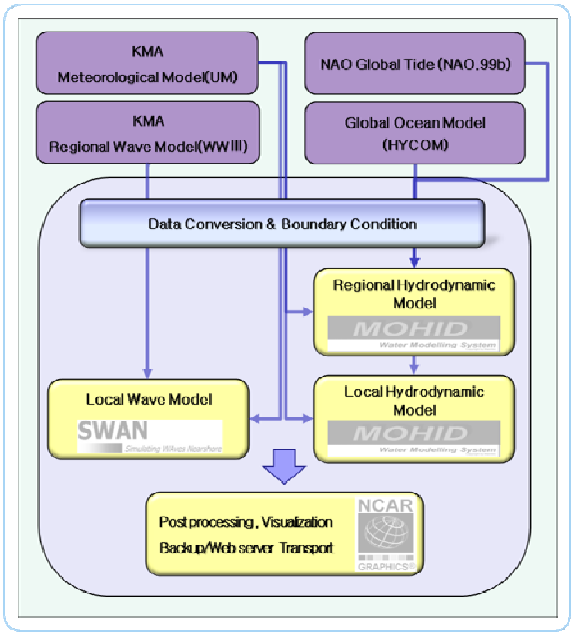

Figure 1. Flow chart of the KMA's Operational Ocean Forecasting System.

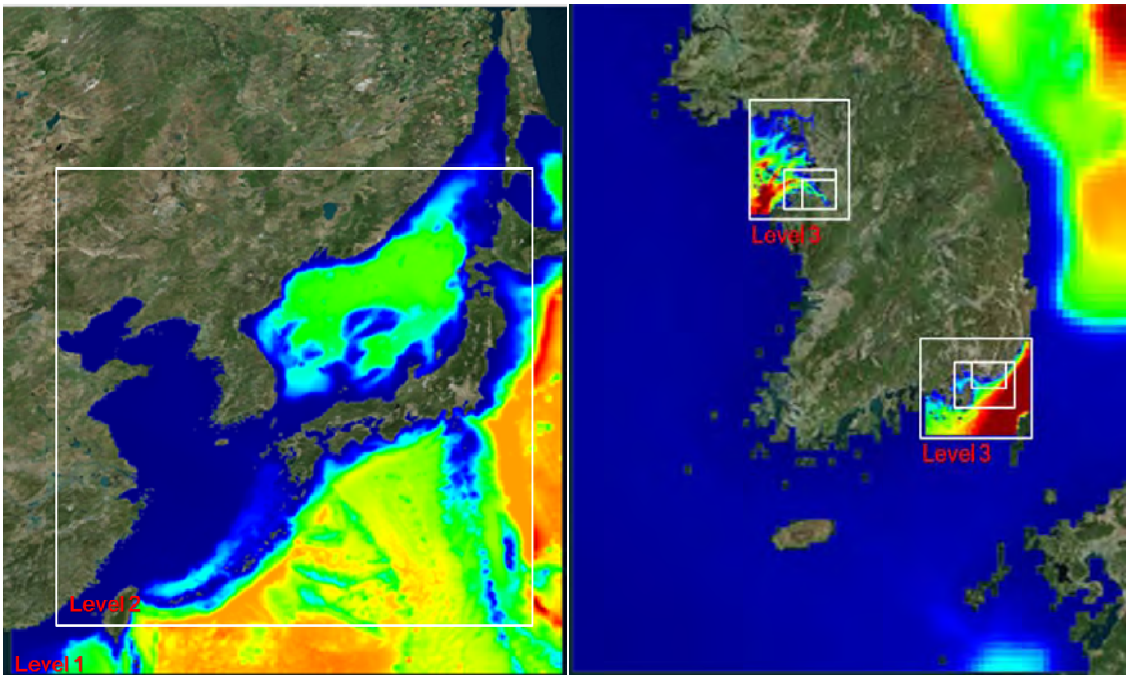

Figure 2. Domain and Bathymetry of Regional scale Hydrodynamic Model (left), Local Scale Hydrodynamic & Wave Model (right).

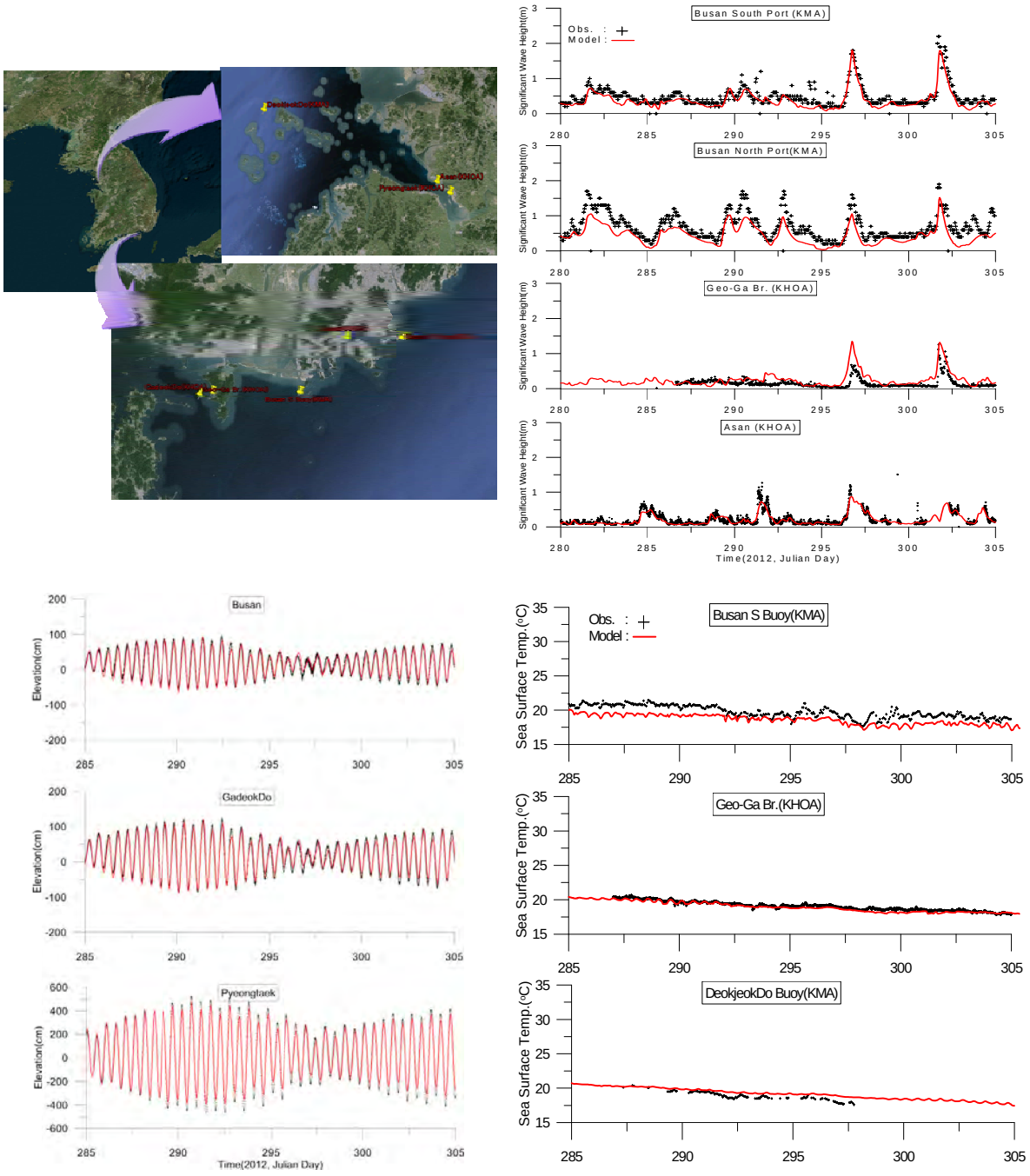

Figure 3. Observation (buoy and tidal St.) locations (upper left) and time series of model comparison with obs. wave height (upper right), sea level (lower left), sea surface temp.(lower right).

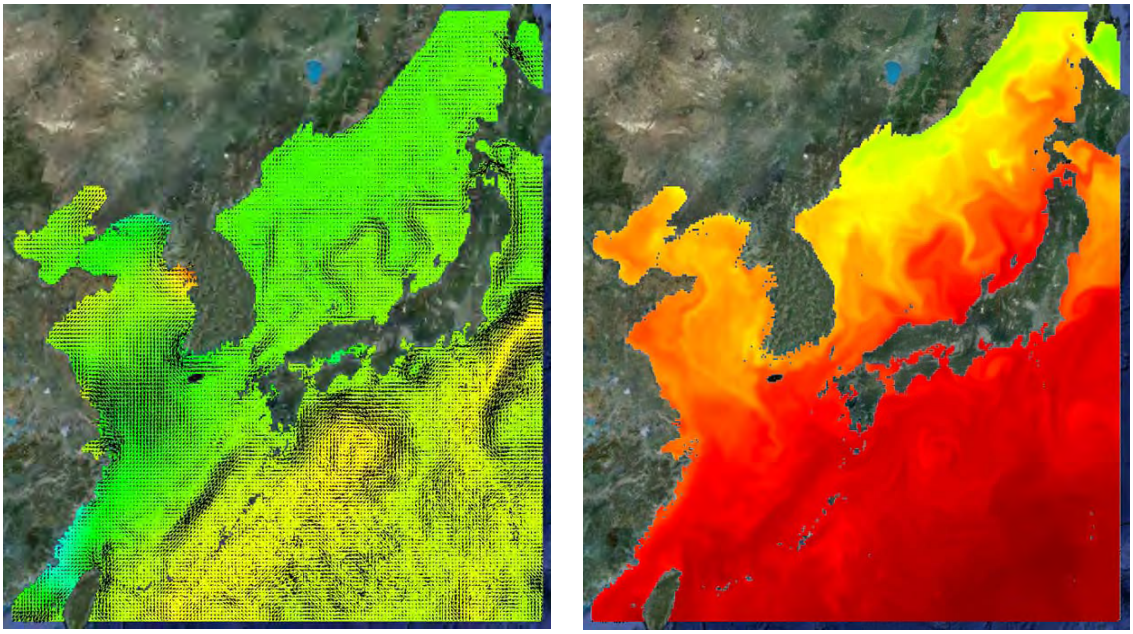

Figure 4. Regional scale hydrodynamic model results (sea level & current - left, sea surface temperature - right).

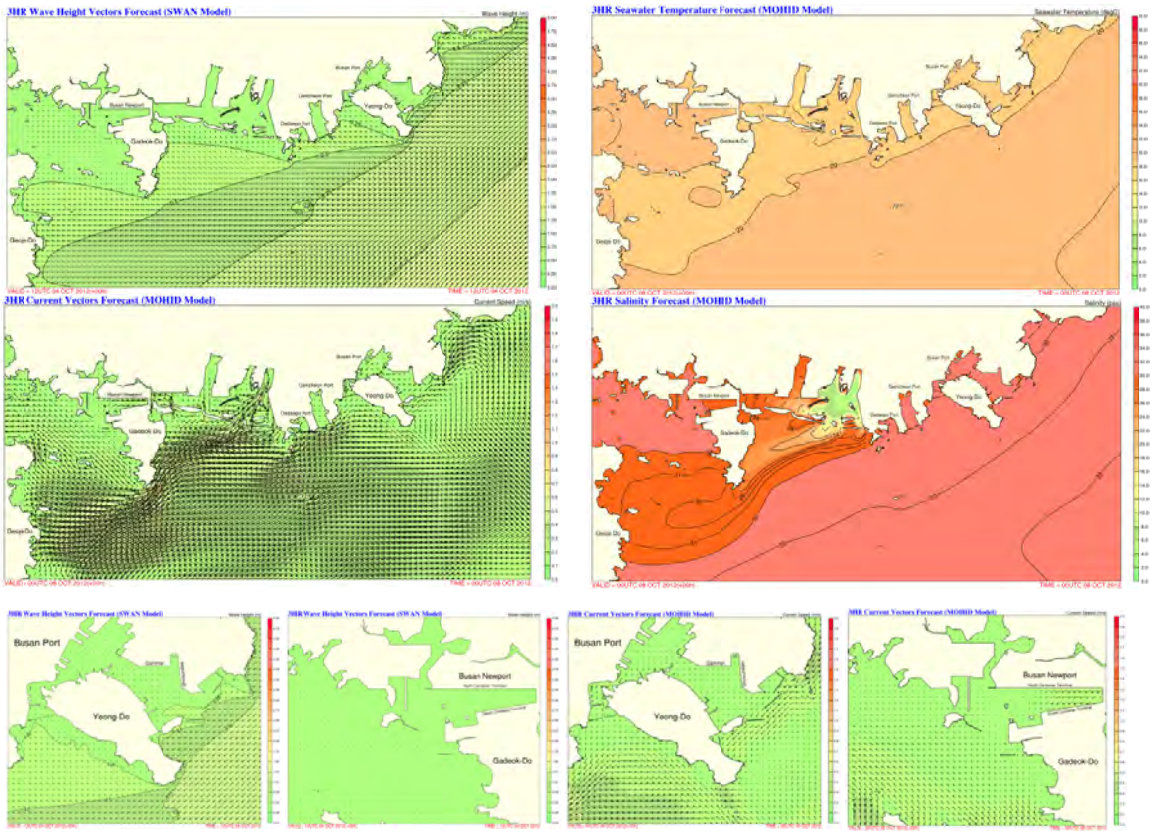

Figure 5. Local scale (Busan coast, Busan Port and Busan New Port) hydrodynamic and wave model results (wave vector & height, current vector, temperature, salinity)

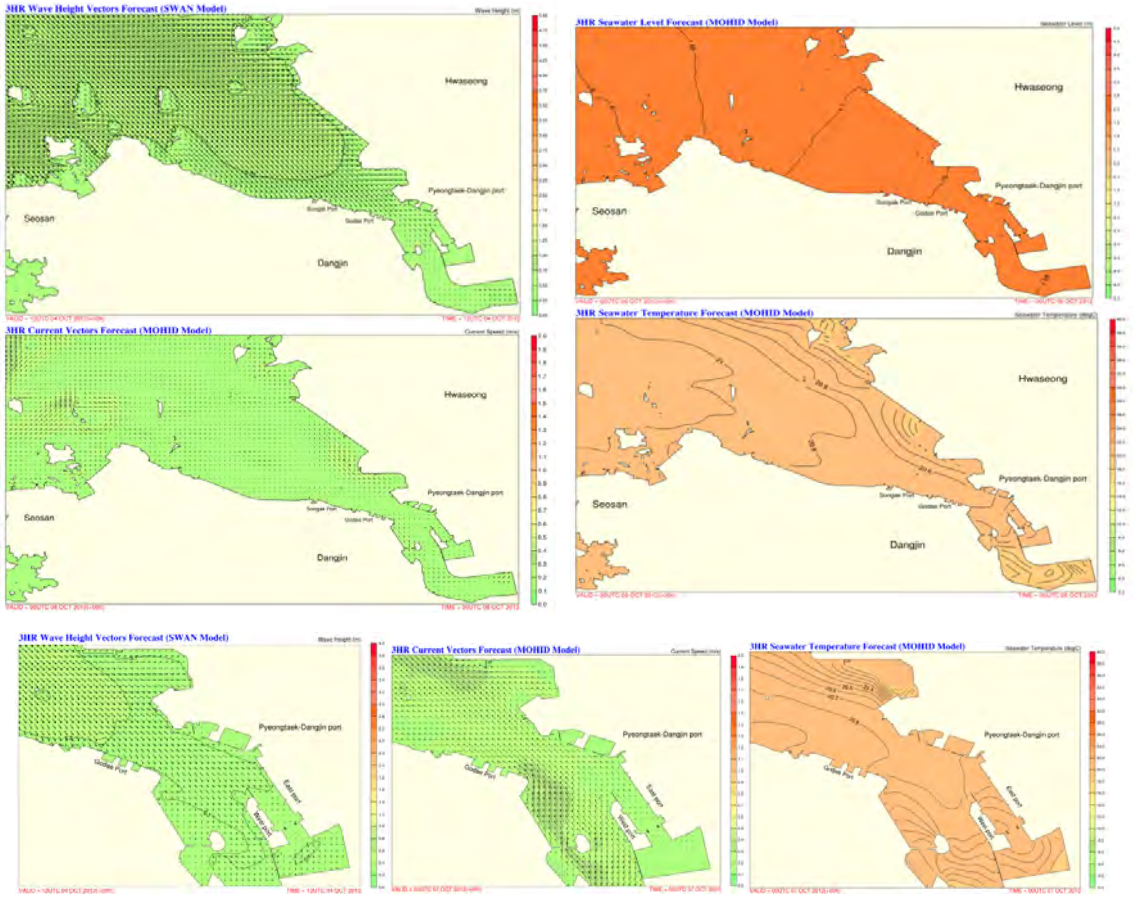

Figure 6. Local scale (Asan coast and Pyeongtaek-Asan Port) hydrodynamic and wave model results (wave vector & height, sea level, current vector, temperature).

Acknowledgements

This research was carried out as a part of the KMA's project "Development of Marine/Harbor meteorological operating system".

References

1. Kyung Man Kwon, Byoung-Ju Choi, Sang-Ho Lee, Yang-Ki Cho, and Chan Joo Jang. (2011). Coastal current along the eastern boundary of the Yellow Sea in summer: Numerical simulations. *Journal of the Korean Society of Oceanography*, 16, 155-168.
2. Matsumoto, K., T. Takanezawa, and M. Ooe. (2000). Ocean Tide Models Developed by Assimilating TOPEX/POSEIDON Altimeter Data into hydrodynamical model: A global model and a regional model around Japan, *Journal of Oceanography*, 56, 567-581.
3. Seung-Nam Seo. (2008). Digital 30sec gridded bathymetric data of Korea marginal seas – KorBathy30s. *Journal of Korean Society of Coastal and Ocean Engineering*, 20, 110-120.
4. Son Park, Han-Sam Yoon, In-Cheol Lee, Heon-Tae Kim. (2008). Correlation between meteorological factors and water discharge from the Nakdong River Barrage, Korea. *Journal of the Korean Society of Marine Environment & Safety*, 14, 111-117.

5. P. Leitão, H. Coelho, A. Santos, R. Neves. (2005). Modelling the main features of the Algarve coastal circulation during July 2004: A downscaling approach. *Journal of Atmospheric & Ocean Science, 10*, 421-462.

An improvement of reproducibility of Pacific decadal oscillation in CMIP5

Youngji Joh[1], Chan Joo Jang[1], Minho Kwon[1], Ho-Jeong Shin[1] and Taewook Park[1,2]

[1]Ocean Circulation and Climate Research Division, Korea Institute of Ocean Science and Technology, 1270 Sa2-dong, SangRok-gu, Ansan 426-744, Korea.

[2]Helmholtz Centre for Ocean Research Kiel, Kiel, Germany.

E-mail: yj_joh@kiost.ac

1. Introduction

The Pacific decadal oscillation (PDO), a dominant phenomenon of North Pacific decadal variability (NPDV), has shown a variability of sea surface temperature (SST) on decadal timescales in the North Pacific (Mantua et al., 1997; Mantua and Hare, 2002; Oshima and Tanimoto, 2008). The PDO which was known for its association with the changes in distribution and abundance of marine species in the North Pacific ecosystems (Mantua, 1997; Hare et al., 1999), recently has received great attention due to its significant impacts on the large scale oceanic and atmospheric variability over the North Pacific as well as the regional climate (Trenberth and Hurrell 1994; Garreaud and Battisti 1999; Dettinger et al., 2000). PDO is characterized by a horseshoe pattern: cold (warm) SST anomaly in the central North Pacific and a warm (cold) SST anomaly along the west coast of North America in positive phase (negative phase). During the 20th century, PDO events persisted for 20-to-30 years, and displayed strengthening in the 1920s and 1970s and weakening in 1940s, showing climatic regime shifts (Mantua et al., 1997; Minobe, 1997).

Previous studies based on atmospheric and ocean models in intermediate level or with full dynamics have demonstrated that various factors including oceanic and atmospheric processes (e.g. Aleutian Low, El Nino-Southern Oscillation (ENSO), equatorial Kelvin waves, and sea surface height in KOE region) generate and impact on PDO (Park et al., 2013). Among these processes, ENSO is the most influenceable contributor, because the ENSO is the critical cause which impacts not only on PDO, but also modify other oceanic and atmospheric factors influencing on it. For example, the ENSO impacts on PDO by generating the oceanic variability of extratropical Pacific through oceanic teleconnection of the coastal Kelvin wave as well as connecting with the Aleutian Low by an atmospheric bridge (Lau and Nath, 1994; Alexander et al., 2002).

PDO variability is similar to the low-frequency variability of ENSO, and has been largely dependent upon the ENSO on interannual or interdecadal timescales (Gershunov and Barnett, 1998; Yu and Zwiers, 2007). Thus, the relationship between the PDO and ENSO has been given attention and studied with a focus on the teleconnection between the extratropical and tropical region. The anomalous warming of the tropical Pacific during El Niño events enhances tropical precipitation with energy transport from ocean to atmosphere and causes atmospheric planetary waves to propagate into extratropics (Alexander et al., 2002 and Liu and Alexander, 2007). This planetary wave pattern is a Pacific/North American pattern (PNA), a linkage between ENSO and

a characteristic atmospheric pattern in the North Pacific sector (Wallace and Gutzler, 1981).

Likewise, using atmospheric and ocean models has provided continuous simulation of PDO and has given us clues to PDO mechanisms; however, specific physical causes for the PDO remain still uncertain, and only a few valid mechanisms have been partly confirmed (Trenberth and Hurrell, 1994; Newman et al., 2003; Schneider and Cornuelle, 2005). It is because model's representation confidence has shown wide variation in fidelity depending upon models, and climate models have computational constraints on the ability of simulations in reproducing present climate conditions due to the limited understanding of interactions and feedbacks in the climate system. Therefore, we have to note that there are still constraints in utilizing climate models and those climate models should be necessarily evaluated and improved for reproducing more precise climate features or physical processes and projecting the reliable global climate changes.

Now, new versions of coupled general circulation models (CGCMs) are available and are expected to show better fidelity of simulation. The changes in physics parameterization of a model from CMIP3 to CMIP5 are diverse from model to model, and minor uncertainties in mechanism in climate models may lead to considerable uncertainties in the accuracies of simulations of physical dynamics. A few studies have previously assessed the PDO simulations of CMIP3 models (Oshima and Tanimoto., 2008), a need for a comparison with CMIP3 and evaluation of new versions of CMIP5 CGCMs has arisen.

The purpose of this study is to evaluate state-of-the-art climate models with a focus on the reproducibility of their simulated spatial pattern of PDO. We pay attention to whether there has been improvement in PDO simulations by CMIP5 models relative to CMIP3 models, and if so, whether the improvement of PDO simulations has been related to an enhanced simulation of ENSO or ENSO-PDO teleconnections. In this study, we used both of the CMIP3 20C3M simulation data and the historical simulation data from the CMIP5 models. In order to assess the simulated tropics-extratropics linkage between ENSO and PDO, we investigated the ENSO simulation and the representation of the precipitation sensitivity to tropical SST and PNA.

2. Data and methods

CMIP3 models from Intergovernmental Panel on Climate Change Fourth Assessment Report in 2007, and CMIP5 models which will be used for the upcoming IPCC Fifth Assessment Report were utilized. 21 CMIP3 models and 20 CMIP5 models were used based on their availability, and SST, precipitation, and easterly wind from CMIP3 and CMIP5 models were analyzed. Because PDO and ENSO show strong peaks during winter season, DJF winter monthly-averages outputs computed by removing the linear trend to extract the decadal variability were used for analysis. Variables that were utilized in this study have different time ranges for convenience in comparison with the observation data. We used SST data from 1900 to 1998, precipitation data from 1979 to 1998, and easterly wind data from 1948 to 1998, for assessment of PDO and ENSO representation, precipitation sensitivity, and PNA representation respectively. All the simulations were bilinearly interpolated onto 2.5° longitude × 2.5° latitude, for comparison with observations data. For evaluating simulation of dynamics in this study, we used Taylor diagram (Taylor 2001).

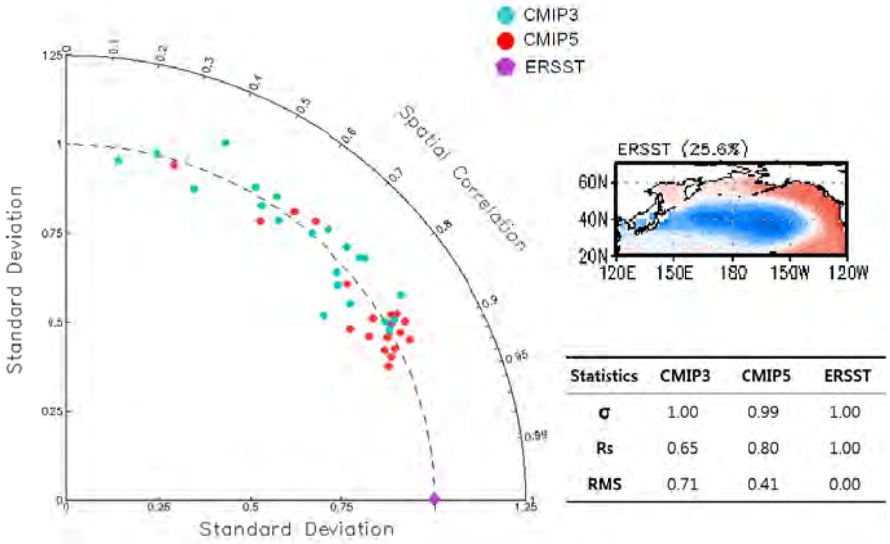

Statistics	CMIP3	CMIP5	ERSST
σ	1.00	0.99	1.00
Rs	0.65	0.80	1.00
RMS	0.71	0.41	0.00

Figure 1. Taylor diagram displaying the main statistics between the spatial distributions of observed and simulated PDO, where the blue circles correspond to CMIP3 models, the red ones to CMIP5 models, and the purple one to the observations. The average of standard deviation σ, spatial correlation Rs, and RMS difference in CMIP3 and CMIP5 are shown together with observations respectively.

3. Result

A Taylor diagram (Fig. 1) shows that CMIP5 models generally have higher spatial correlation, Rs, and lower RMS difference than CMIP3 in the diagram. From CMIP3 to CMIP5, Rs and RMS difference are significantly improved showing that Rs increases from 0.65 to 0.80 and RMS error decreases from 0.71 to 0.41 respectively. In the diagram, it is characterized that there doesn't exist anymore poor performance group of Rs in CMIP5, while CMIP3 have, which indicates that the improvement of CMIP5 is attributed to disappearing of this low Rs group.

The multi-model ensemble (MME) analysis (Fig.2) shows that both CMIP3 and CMIP5 models have a problem with overestimating SST anomalies in part of KOE region; however, the simulated PDO pattern of CMIP5 models exhibit much similar to the observation than one of CMIP3 with the strong signal and location of cold anomaly in the Central Pacific. The better-5 of CMIP5 models (Fig.2-a) shows the slightly increased spatial correlation coefficient, 0.95, from 0.93 of CMIP3 (Fig.2-b), while the spatial correlation of poor-5 significantly increased from 0.50 to 0.79 from CMIP3 to CMIP5..

Taylor diagram for ENSO (Fig.3) shows that the number of outlier decreases from 4 to 1 from CMIP3 to CMIP5. Without these outliers, from CMIP3 to CMIP5, the spatial correlation increase from 0.86 to 0.89 and the RMS difference decrease from 0.28 to 0.21. As like PDO in Fig.1, however, the mean of standard deviation has not improved.

Precipitation-SST relationship for NINO3.4 for December, January and February during 1979-1998 from the observed, CMIP3 and CMIP5 are shown in Fig.4. In observed scatter plot (Fig.4-a), the precipitation is highly correlated with SST for tropical Pacific. The mean precipitation increases slowly with SST up to around 27°C, which might be a threshold, and sensitively responses to SST between 27~29°C. The regression coefficient of observations is 2.36 and correlation coefficient between two variables is 0.835. Through Fig.4, it is found the regression coefficient (correlation coefficient) of CMIP5 increases from 0.75 to 1.41 (0.55 to

0.80), as approaching statistic values of the observations.

The Taylor diagram for PNA (Fig.5) shows that both CMIP3 and CMIP5 have the same problem that the variations of PNA pattern is not of the right amplitude but too weak; however, the average of standard deviation and spatial correlation both increase from 0.34 to 0.39 and from 0.58 to 0.67 respectively. RMS error decreases from 0.71 to 0.63 showing enhanced simulation in CMIP5.

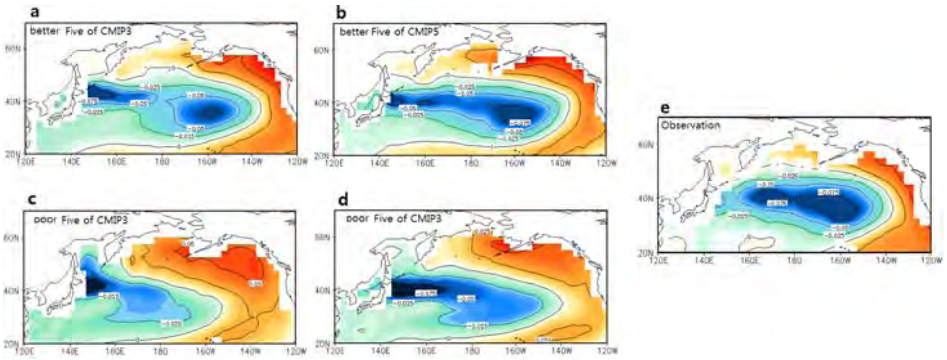

Figure 2. Better-5 and poor-5 multi-model ensemble mean of the leading EOF eigenvectors of CMIP3 and CMIP5 models and the observation data. From left, better-5 of CMIP3 (a) and CMIP5 CGCMs (b), poor-5 of CMIP3 (c) and CMIP5 CGCMs (d), and the observation data (e)

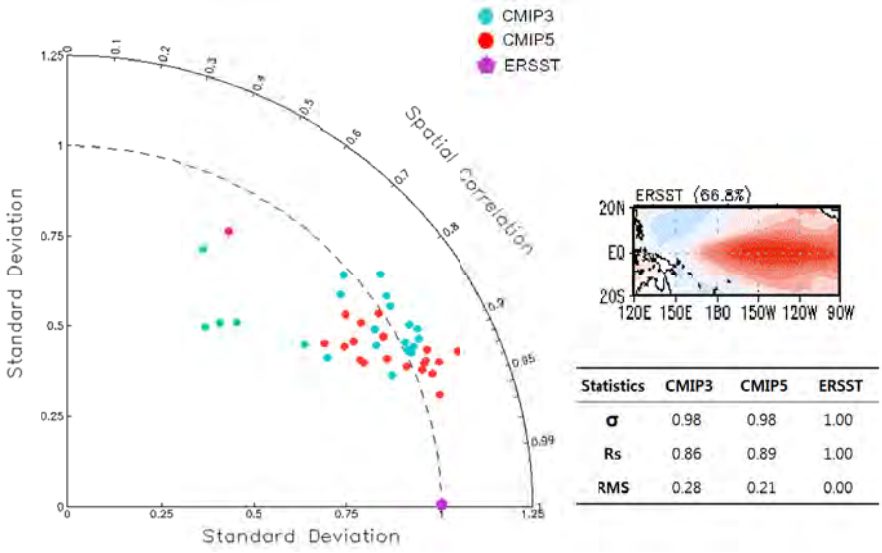

Statistics	CMIP3	CMIP5	ERSST
σ	0.98	0.98	1.00
Rs	0.86	0.89	1.00
RMS	0.28	0.21	0.00

Figure 3. As in Fig.1 but for the ENSO

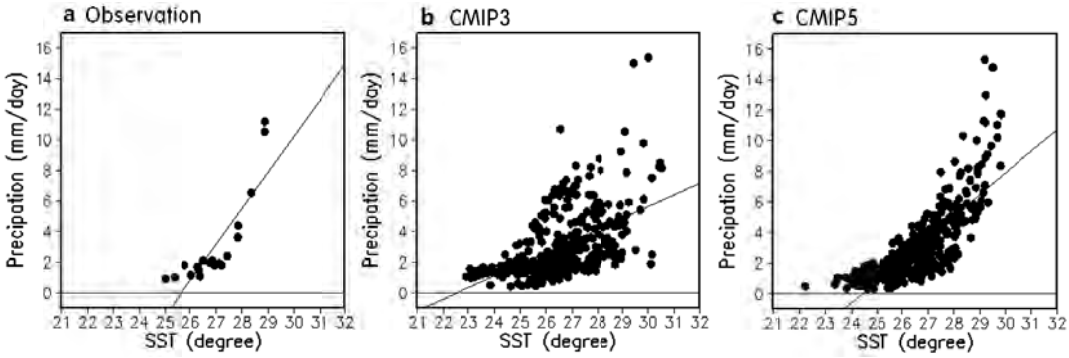

Figure 4. Scatter plots with the linear regression between precipitation and SST for DJF during 1979~1998 for NINO3.4. From left to right, the observations (a), CMIP3 CGCMs (b), and CMIP5 CGCMs (c) are shown respectively.

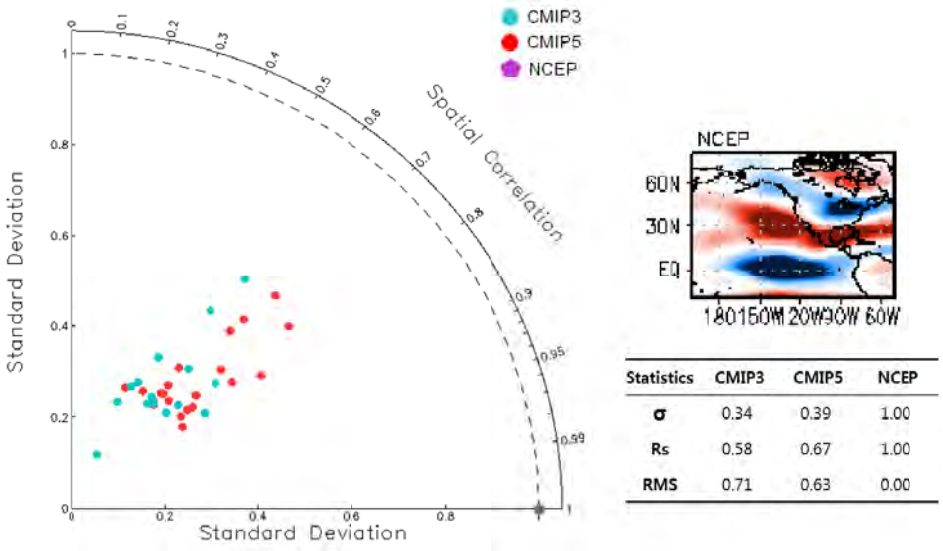

Statistics	CMIP3	CMIP5	NCEP
σ	0.34	0.39	1.00
Rs	0.58	0.67	1.00
RMS	0.71	0.63	0.00

Figure 5. As in Fig.1 but for the PNA

4. Discussion and Conclusion

In this study, we assessed the reproducibility of PDO in CMIP3 and CMIP5 models by directly comparing the simulated pattern and the observed one. We also examined the reproducibility of ENSO and simulation of the air-sea feedback to figure out the roles of ENSO and extratropics-tropics linkage on the PDO simulation in the coupled models. We used the PDO and ENSO indices for representing the SST over the North Pacific and the tropics respectively, and evaluated their spatial patterns and amplitude of them using the Taylor diagram. For the simulation of ENSO-PDO teleconnections, we assessed the sensitivity of precipitation to tropical SST and PNA representation.

It is found that an improvements of PDO simulations from CMIP3 to CMIP5 is deeply related to the enhanced simulation of ENSO and ENSO-PDO teleconnections. First, compared with CMIP3 models, CMIP5 models show some enhancement in simulating the amplitude and spatial

patterns of ENSO. It is considered that the enhancement of ENSO is directly related to the one of PDO, because the maximum anomalous SST in the central North Pacific which shows the significant improvement of the PDO pattern coincides with the characteristics of SSTA composite over the North Pacific during El Nino events in multi-ensemble mean analysis. Oshima and Tanimoto (2008) also indicated that the high reproducibility of extratropics-tropics linkage in SST variability on decadal time scale influences on the high PDO metric of CMIP3 simulations. Second, the precipitation in CMIP5 is more highly correlated with the tropical SST than in CMIP3, simulating more realistic processes of convection/precipitation and the nonlinear nature between SST and precipitation in the Tropics. Thus, this improvement may allow the tropically forced (SST driven) air-sea feedback for transporting energy from the tropical sea into the atmosphere to be represented better in CMIP5. Lastly, it is found that CMIP5 models show some improvement in simulating PNA patterns, especially the North Pacific center which indicates Aleutian low. As previously noted, the PNA-like pattern over North Pacific is associated with the pattern in the in-phase ENSO-PDO relationship from 20C3M (Kwon et al., 2012), and it is considered that the improvement of PDO simulations in this study has been attributed to this enhanced ENSO-PDO teleconnections, because whether a formation of planetary waves has an appropriate locations is important to the representation of PDO in the climate models.

Reference

1. Alexander, M.A., I. Bladé, M. Newman, J.R. Lanzante, N.C. Lau, and J.D. Scott (2002), The Atmospheric Bridge: The Influence of ENSO Teleconnections on Air-Sea Interaction over the Global Oceans. *J. Climate*, 15, 2205-2231.
2. Dettinger, M. D., D. S. Battisti, R. D. Garreaud, G. J. McCabe, Jr. and C. M. Bitz (2000), Interhemispheric effects of interannual and decadal ENSO-like climate variations on the Americas. p. 1–16. In Present and Past Interhemispheric Climate Linkages in the Americas and their Societal Effects. ed. by V. Markgraf, Cambridge University Press. Cambridge, U.K.
3. Gershunov A, Barnett TP. 1998. Interdecadal modulation of ENSO teleconnection. *Bulletin of American Meteorological Society* **79**: 2715–2725
4. Kwon, M., S. W. Yeh, Y. G. Park and Y. K. Lee (2012), Changes in the linear relationship of ENSO-PDO under the global warming. *Int. J. Climatol*. doi: 10.1002/joc.3497
5. Lau, N.-C., and M. J. Nath (1994), A modeling study of the relative roles of tropical and extratropical SST anomalies in the variability of the global atmosphere- ocean system. *J. Climate, 7*, 1184-1207.
6. Liu, Z. and M. A. Alexander (2007), Atmospheric Bridge Oceanic Tunnel and Global Climatic Teleconnections. *Rev. Geophys., 45*, RG2005, doi:10.1029/2005RG000172.
7. Mantua, N.J., Hare, S.R., Zhang, Y., Wallace, J.M. and R.C. Francis (1997), A Pacific interdecadal climate oscillation with impacts on salmon production. *Bull. Amer. Met Soc.*, 78, 1069-1079.
8. Mantua, N.J. and S.R. Hare (2002), The Pacific Decadal Oscillation. *J. Oceanogr*. 58: 35-44.
9. Minobe, S. (1997), A 50–70 year climatic oscillation over the North Pacific and North America. *Geophysical*
10. *Research Letters, 24*, 683–686.
11. *Newman*, M., G. P. Compo and M. A. Alexander (2003), *ENSO-Forced Variability of the Pacific Decadal Oscillation. J. Climate, 16*, 3853–3857.
12. Oshima, K. and Y. Tanimoto (2009), An evaluation of reproducibility of the Pacific Decadal

Oscillation in the CMIP3 Simulations. *Journal of the Meteorological Society of Japan, 87*: 755-770.
13. Overland, J. E., and M. Wang (2007), Future climate of the North Pacific Ocean, *Eos Trans. AGU 88*: 182.
14. Park, J., S. An, S. Yeh and N. Schneider (2013), Quantitative assessment of the climate components driving the pacific decadal oscillation in climate models. *Theor. Appl. Climatol.*, 112:431-445
15. Schneider, N., A. J. Miller, and D. W. Pierce (2002), Anotomy of North Pacific decadal variability. *J. Clim., 15*, 586-605
16. Schneider, N., and B. D. Cornuelle (2005), The forcing of the Pacific Decadal Oscillation. *J. Clim., 18*, 4355- 4373
17. Taylor, K. E., (2001), Summarizing multiple aspects of model performance in a single diagram. *J. Geophys. Res.*, 106, 7183-7192.
18. Trenberth K. E, Hurrel J. W (1994), Decadal atmospheric-ocean variations in the Pacific. *Clim Dyn 9*:303–319
19. Wallace, J. M. and D. S. Gutzler (1981), Teleconnections in the Geopotential Height Field during the Northern Hemisphere Winter. *Mon. Wea. Rev.*,109, 784–812.
20. Yu, B. and F. W. Zwiers (2007), The impact of combined ENSO and PDO on the PNA climate: a 1000-year climate modeling study. *Clim. Dyn. 29*:837-851

Dynamical downscaling of future projections of precipitation change over the East Asia

Chun-Yong Jung[1], Chan Joo Jang[1], Hyung-Jin Kim[2], and Min-Ho Kwon[1]

[1]Korea Institute of Ocean Science and Technology, Ansan, Korea
[2]APEC Climate Center, Busan, Korea
E-mail: cyjung@kiost.ac

1. Introduction

Global climate change induced by an increased level of greenhouse gases is typically estimated by global general circulation model (GCMs). However, this approach has been difficult to provide regional details due to GCM's limitations in horizontal resolution as well as in physical parameterizations. To overcome such difficulty, downscaling methods have been proposed, through which local to regional climatic conditions can be produced in greater details. Two major techniques include dynamical downscaling, where GCM output is used to drive a regional model with higher spatiotemporal resolution and more sophiscated physcal schemes, and statistical downscaling, where an observed statistical relationship between large-scale and local variables is applied to GCM simulation results to extract small-scale information (Murphy 1999; Wood et al. 2004; Wang et al. 2004). The conventional dynamical downscaling utilizes GCM outputs as initial and lateral boundary conditions. In comparison, the Pseudo Global Warming Method (PGWM) introduced recently by Kimura (2007) and Sato et al. (2007) adopts a mixture of observations and GCM simulations to carry out regional climate model (RCM) simulation. The present study aims to investigate climate change in an anthropogenically warmed climate with the aid of the PGWM, with particular focus on the summer rainfall variability over East Asia.

2. Evaluation of the CMIP5 GCMs for dynamical downscaling

The PGWM relies on the differences between present and future climates simulated by GCMs. The selection of GCMs used for downscaling, therefore, is of central importance for the PGW simulations. It is generally believed that a GCM's ability to realistically simulate the present climate could be considered a measure of its capability to project the future. In this context, we assessed the fidelity of the present East Asian monsoon simulated by a suite of coupled GCMs (CGCMs) by applying a multi-variate EOF (MVEOF) to climatological monthly rainfall (PR) and zonal wind at 850 hPa (U850) as these variables faithfully reflect the seasonal contrast and reversal of precipitation and circulation associated with the East Asian monsoon. As of early 2013, 41 CGCMs have participated in the Couple Model Intercomparison Project Phase 5 (CMIP5) under the protocol of the "historical run". Among them, MVEOF was applied only to 16 CGCMs that provide U850 data over high terrain. The modeled climatological MVEOF was validated against that derived from the Global Precipitation Climatology Project (GPCP; Huffman et al., 2011) for PR and NCEP/NCAR reanalysis data (NRA1; Kalnay et al., 1996) for U850 during 1981-1990 (Fig 1).

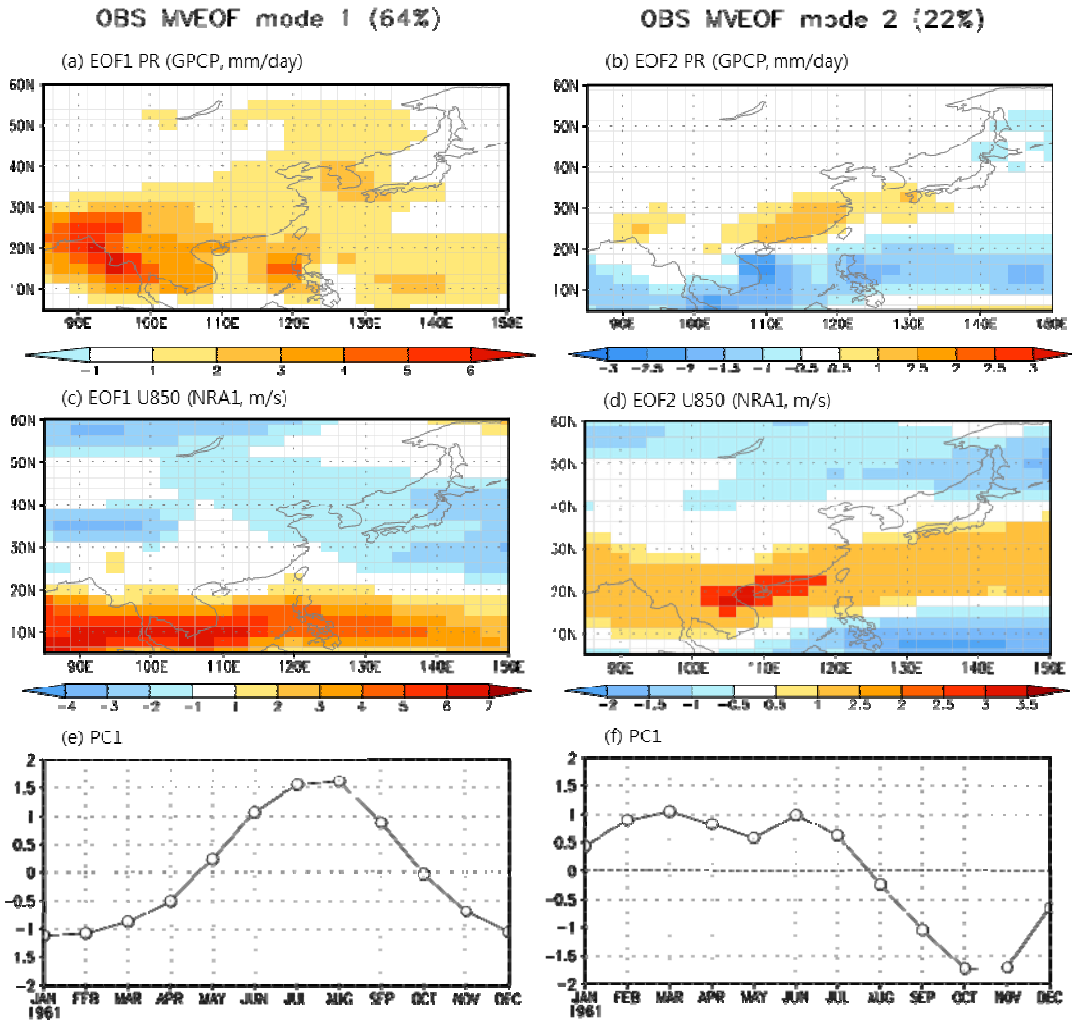

Figure 1. (Left) The first and (right) second leading MVEOF modes and their fractional variances obtained from the observations.

In observations, the first two leading modes account for 64% and 22% of the total variance and faithfully represent summer-winter and spring-fall contrast, respectively. Accordingly, the reality of the simulated MVEOF is estimated using spatial correlation (SC) of eigenvectors and temporal correlation (TC) of principal components weighted by the observed fractional variance

$$SC = \frac{0.64*\left(\frac{PREOF1+U850EOF1}{2}\right)+0.22*\left(\frac{PREOF2+U850EOF2}{2}\right)}{0.64+0.22},$$

$$TC = \frac{0.64*PC1+0.22*PC2}{0.64+0.22}.$$

Then a spatiotemporal correlation (STC) of the simulated MVEOF can be defined using the

degree of freedom in space (DOFS) and time (DOFT) as follows

$$STC = \frac{SC * DOFS + TC * DOFT}{DOFS + DOFT}.$$

In addition, the CGCMs' performance in reproducing the climatological monthly mean over East Asia region (85E-150E, 5N-60N) is quantified using the arithmetic average of mean monthly pattern correlation coefficients of PR and U850 (PCC). Fig 2 shows a scatter plot of STC (ordinate) and PCC (abscissa) calculated from the 16 CGCMs. The results indicate that three CGCMs (i.e., CanESM2, CanCM4, CNRM-CM5) exhibits better agreement with the observations than other models. As a preliminary study, we only used the results of CanESM2 model to carry out the PGW experiments.

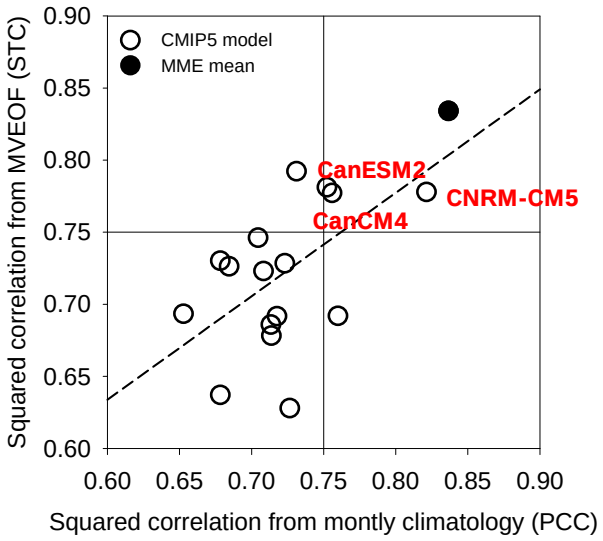

Figure 2. Evaluation of CGCM performance on the East Asian monsoon. The ordinate is the spatiotemporal correlation (STC) of the simulated MVEOF and the abscissa is the average of mean monthly pattern correlation coefficients (PCC).

3. Dynamical downscaling with the Pseudo Global Warming Method

We used the Advanced Research of Weather Research and Forecasting (WRF) model version 3.4.1 (Skamarock et al., 2012). A set of control run (CTRL) was conducted using the NCEP/DOE reanalysis (NRA2, Kanamitsu et al., 2002) for 10 summers (April 20 – August 30) from 1981 to 1990. As for the PGW experiments, the climatological 6-hourly differences (i.e., the differences in climatology between 1981-2000 under "historical run" and 2081-2100 under "RCP4.5" scenario) simulated by CanESM2 were added to CTRL's boundary conditions (termed as PGW-CanESM2). As such, the future data sets for the PGW-CanESM2 reflect the simulated future climate change imbedded with short-term disturbances and interannual variability occurred in 1980s. These procedures are summarized in Fig 3. The model domain (80E-190E, 5N-65N) was covered by 215 x 155 grids with 50-kilometer grid interval (Fig 4). The Physics packages include the WRF Single-Moment 6-Class (WSM6) microphysics scheme (Hong and Lim, 2006), the new

Kain-Fritsch cumulus parameterization scheme (Kain, 2004), YSUPBL (Hong et al.,2006), a simple cloud-interactive radiation scheme (Dudhia, 1989), and Rapid Radiative Transfer Model (RRTM) longwave radiation (Mlawer et al., 1997) scheme.

Note that we present the simulation results from May to August because the first 10 days were regarded as a spin-up period.

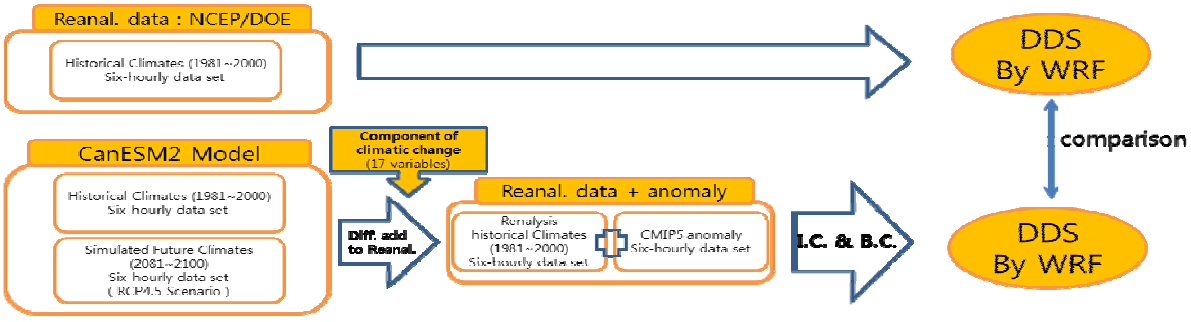

Figure 3. Flow chart of the PGW simulation. "Diff" denotes climatological difference between the present (1981~2000) and future (2081~2100) climates.

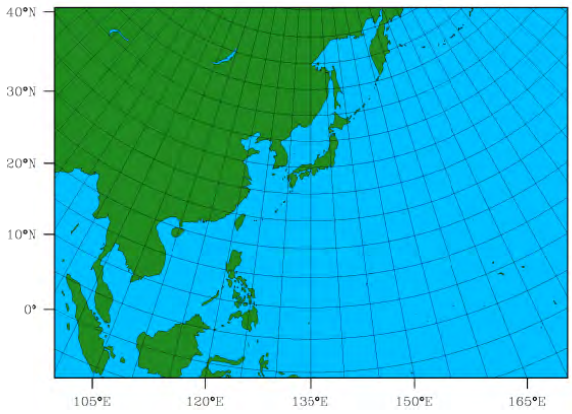

Figure 4. The model domain for PGW simulation.

4. Results

4.1 Control simulations

Figure 5a shows the 10-year mean summertime (June through August) precipitation derived from the CMAP. Heavy precipitation exceeding 420mm/month is observed over the tropics and subtropics, including the Bay of Bengal, the Indochina Peninsula, the South China Sea, and the Western North Pacific. A large amount of precipitation exceeding 200mm/month is also appeared along the Meiyu-Changma-Baiu front over East Asia. The CTRL simulation captures well the observed precipitation patterns, in particular the centers of pluvial maxima, in spite of a moderate underestimation over the mid-latitude regions (e.g., the Korean peninsula) and a prominent overestimation over most of the tropical rainbands (Fig 5b).

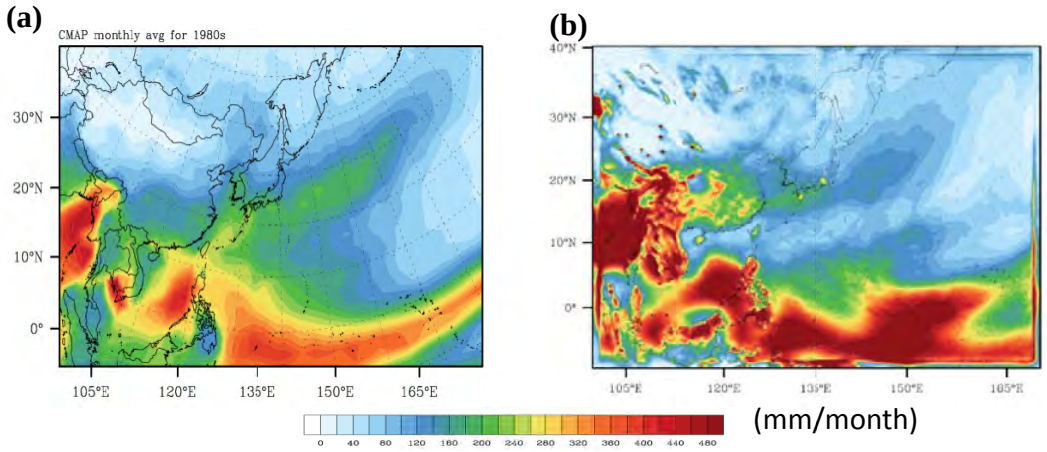

Figure 5. Distributions of 10-year mean summertime precipitation (mm/month) (1981-1990) from (a) CMAP and (b) CTRL run.

4.2 PGW simulation and projected change

The PGW-CanESM2 simulates excessive precipitation compared to the CTRL run, as shown in Fig 5. and Fig 6. Fig 7 shows difference for summer precipitation between CTRL run and CanESM2 run. In this figure, precipitation increases over the Meiyu-Baiu front and southern part of the Korean peninsula, while precipitation decreases are projected over the Changma front (from the central China to the mid-Korean peninsula). These facts suggested that future changes in precipitation by global warming appear to be different depending on region. In the Korean peninsula, the spatial patterns of precipitation change between northwestern region and southern region were particularly different. This north-south contrast of summertime precipitation anomaly is a characteristic feature of the future projections around the Korean peninsula.

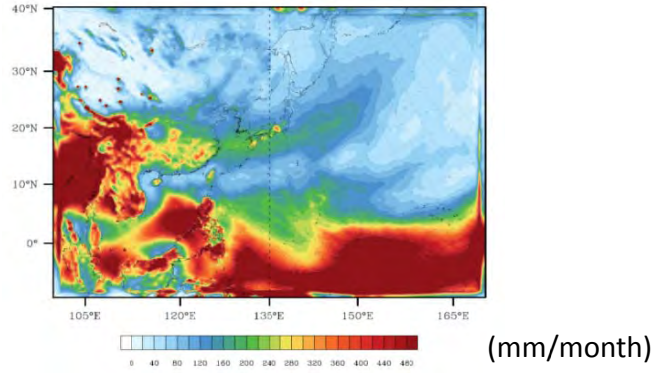

Figure 6. Summer precipitation (mm/month) simulated by PGW-CanESM2 run.

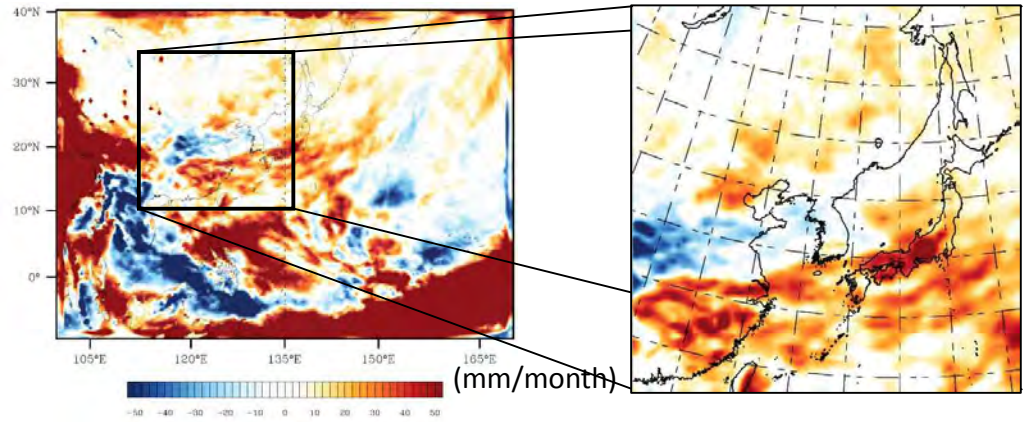

Figure 7. (Left) Difference for summer precipitation (mm/month) between CTRL run and PGW-CanESM2 run and (right) the detailed description of the East Asian region, including Korea, China and Japan.

5. Conclusions

This study presents preliminary results on the future changes of East Asian summer monsoon precipitation through the Psudo Global Warming Method. Because successful PGW simulation depends on a CGCM's performance, we quantified the reproducibility of East Asian monsoon simulated by a suite of CGCMs. As a results, three models, including CanESM2, were distinguishable from the others. The PGW-CanESM2 run, in which the climatological 6-hourly differences between the present and the future in CanESM2 were added to the observed to drive a regional model, tends to enhance precipitation along the Meiyu-Baiu front. On the other hand, the intensity of the Changma decreased in spite of the fact that it is also an essential part of East Asian monsoon. As the air masses that define Meiyu, Changma, and Baiu fronts differ from one region to another, it is speculated that the regional rainfall differences likely result from the different changes of air masses.

References

1. Dudhia, J., 1989: Numerical study of convection observed during the winter monsoon experiment using a mesoscale two-dimensional Model. *J. Atmos. Sci*., 46, 3077–3107.
2. Hong, S.-Y., and J.-O. J. Lim, 2006: The WRF single-moment microphysics scheme(WSM6), *J. Korean Meteorol. Soc*., 42, 129-151.
3. _____, Y. Noh, and J. Dudhia, 2006: A revised vertical diffusion package with an explicit treatment of entrainment processes. *Mon. Wea. Rev*., 134, 2318–2341.
4. Huffman, G. J., D. T. Bolvin, and R. F. Adler (2011), Global Precipitation Climatology Project Version 2.2 Combined Precipitation Data Set, World Data Center A, National Climatic Data Center, Asheville, NC, Available at www.ncdc.noaa.gov/oa/wmo/wdcamet-ncdc.html.
5. Kain, J. S., 2004: The Kain-Fritsch convective parameterization: An update. J. Appl. Meteor., 43, 170–181.
6. Kalnay, E., et al. (1996), The NCEP/NCAR 40-Year Reanalysis project, *Bull. Amer. Meteorol. Soc,* 77, 437–471.
7. Kawase, H., T. Yoshikane, M. Hara, B. Ailikun, F. Kimura, and T. Yasunari (2008), Downscaling of the climatic change in the Mei-yu rainband in East Asia by a pseudo climate

simulation method, *SOLA*, 4, 73 – 76,doi:10.2151/sola.2008-019.
8. _____, _____, _____, F. Kimura, T. Yasunari, B. Ailikun, H. Ueda, and T. Inoue (2009), Intermodel
9. variability of future changes in the Baiu rainband estimated by the pseudo global warming downscaling method, *J. Geophys. Res*., 114, D24110, doi:10.1029/2009JD011803.
10. Kimura, F., and A. Kitoh (2007), Downscaling by pseudo global warming method, *Final Rep*., pp. 43– 46, ICCAP, Res. Inst. for Humanity and Nat., Kyoto, Japan.
11. M. Kanamitsu, W. Ebisuzaki, J. Woollen, S-K Yang, J.J. Hnilo, M. Fiorino, and G. L. Potter. 1631-1643, Nov 2002, Bulletin of the American Meteorological Society.
12. Mlawer, E. J., S. J. Taubman, P. D. Brown, M. J. Iacono, and S. A. Clough, 1997: Radiative transfer for inhomogeneous atmospheres: RRTM, a validated correlated-k model for the longwave. *J. Geophys. Res.*, 102(D14), 16663-16682.
13. Sato, T., F. Kimura, and A. Kitoh (2007), Projection of global warming onto regional precipitation over Mongolia using a regional climate model, *J. Hydrol*., 333, 144–154, doi:10.1016/j.jhydrol.2006.07.023.
14. Skamarock, W. C., J. B. Klemp, J. Dudhia, D. O. Gill, D.M. Barker, M. G. Duda, X-Y. Huang, W. Wang and J. G. Powers, 2008: A Description of the Advanced Research WRF Version 3, NCAR Technical Note, NCAR/TN–475+STR, 123 pp. [Available on-line at: http://www.mmm.ucar.edu/wrf/users/docs/arw_v3.pdf]
15. Xie, P., and P. A. Arkin (1997), Global precipitation: A 17-year monthly analysis based on gauge observation, satellite estimates, and numerical model outputs, *Bull. Am. Meteorol. Soc.*, 78, 2539–2558, doi:10.1175/1520-0477(1997)078<2539:GPAYMA>2.0.CO;2.

Development of Regional Climate Model for western North Pacific: Assessment of a present ocean climate simulation

Chul Min Ko, Chan Joo Jang, Chun Yong Jung

Ocean Circulation and Climate Research Division, Korea Institute of Ocean Science and Technology, Ansan, Gyeonggi, 424-744, Korea
E-mail: kkobchul@kiost.ac

1. Introduction

Recent study based on satellite and Korea Oceanographic Data Center (KODC) observations conducted over the eastern coast of Korea shows the linear trend of 10m ocean temperature during 1961-2007 years is negative in coastal areas, in contrast with positive trend offshore (Park et al., 2010). Park et al. (2010) attributed spatial difference of 10m ocean temperature trend to linkage to the long-term changes in the large-scale atmospheric and oceanic environment of the western North Pacific. Also, Deep convection south of Vladivostok in the East Sea apparently occurs with different Mixed Layer Depth (MLD) every winter (Tally et al., 2003). Kang et al. (2004) investigated the impacts of surface atmospheric forcing with different time-space scales on the simulation of water mass in the East Sea using POM (Princeton Ocean Model) and the results indicate that the deep convection is the effects of synoptic events when large heat loss and strong wind stress associated with cold-air outbreaks and extratropical cyclones occur. For the long-term changes of these ocean properties in western North Pacific marginal seas, we need to investigate changes between present and future ocean climate for the ecosystem study through high-resolution data. Usually, the general circulation models (GCMs) is applied to understand the climate system and to project the future climate. However, simulating and predicting climate variability from GCMs is difficult due to too coarse resolution of approximately 100-200 km to resolve the complex air-sea interaction system in marginal and coastal areas. The regional climate models (RCMs) have been used to downscale the GCMs output to obtain high-resolution results. Therefore, we focused on a developed regional ocean climate model using Regional Ocean Modeling System (ROMS) to study interannual variation of ocean property of present climate for the western North Pacific marginal seas.

2. Model description and Experimental design

The ROMS used in this study is a free-surface, hydrostatic, and primitive equations ocean model with stretched terrain-following coordinate. The ROMS ocean domain is the western North Pacific marginal seas ranging from 105˚E to 180˚E and from 10˚N to 55˚N. The ROMS has 1/12˚ of horizontal resolution and 30 vertical layers which is similar to the vertical configuration of Data Assimilation and Model Evaluation Experiments-North Atlantic Basin (DAMEE-NAB) case. The bathymetry is interpolated from ETOPO1 with r-factor less than 0.2 to avoid error of pressure gradient. The K-profile parameterization (KPP) scheme is used for turbulent vertical mixing. The initial and boundary data are obtained from Simple Ocean Data Assimilation (SODA) with 0.5˚ of horizontal resolution and the National Centers for

Environmental Prediction (NCEP) RA2 data with 2.5˚ of horizontal resolution are calculated for surfacing forcing using bulk formulae. The radiation and nudging method is applied to boundary field with time scales of 1 year and 1 day to prevent climate drift. The domains used in this study are shown in Fig. 1. The spin-up experiment is achieved using monthly SODA and daily NCEP data of 1979 years during 10 years to reach quasi-equilibrium ocean state then the model is integrated during 1979-2008 years.

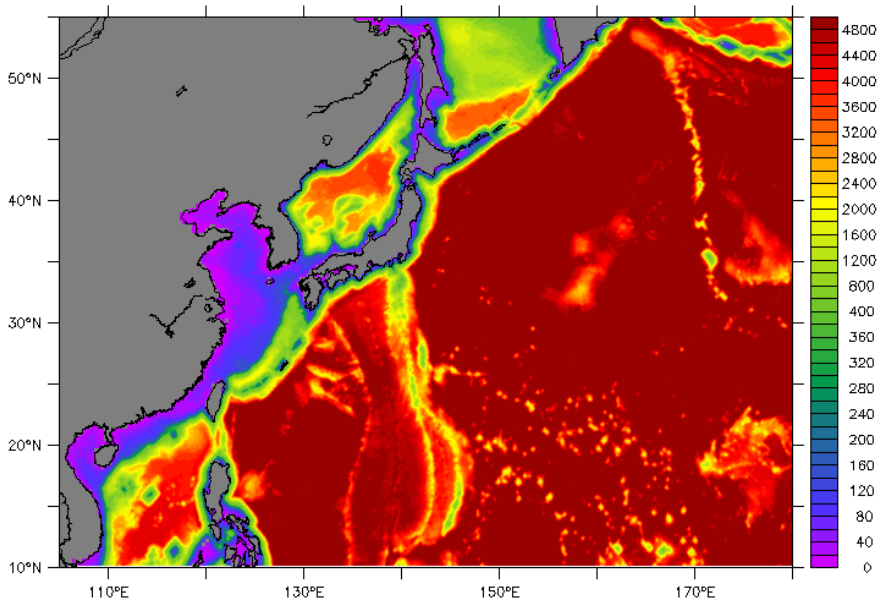

Figure 1. The western North Pacific domain and topography for the ROMS model

3. The preliminary results

The long-term means of Sea Surface Temperature (SST) can be a valid diagnostics of model skill in the regional ocean model. The model results show seasonal cycles in monthly mean SST with minimum in February and maximum in August and spatial distributions of climatological mean agree well with the Levitus climatology (Fig. 2). The time series of the simulated mean SST in all marginal seas are comparable to the observation. The variances of marginal seas are relatively larger than that of open oceans such as the Kuroshio extension regions. The linear trend of simulated SST is compared with monthly NOAA Extended Reconstructed SST (ERSST) during 30 years, which is similar to observation, although a period is too short to analyze the data. However, the long-term temperature changes in the ocean intermediate layers using the KODC observations show the negative trend which is different from the positive trend in the surface layers off the east of Korea during summertime, while model cannot simulate the changes in the intermediate layers properly. As the other valid diagnostics of model skill, we compare the model results and the observed data with the vertical structures of the currents along the observational lines and volume transports near the Taiwan Strait, the Korea Strait, and the Tsugaru Strait, etc. There is good agreement between observed annual mean geostrophic current and the simulated current in terms of current strength, location of the strongest current, and horizontal and vertical gradients in the PN line, where long-term hydrographic data are available (Oka et al. 2000). The

seasonal variation of volume transport in the Tsugaru Strait is the maximum in autumn and the minimum in winter, but time-averaged transports in the Korea Strait are underestimated, compared with the observation estimated by Teague et al. (2002). This is attributed to unsuitable topography smoothing near the East China Sea shelf in the model.

To examine the variation of the ocean upper layers, the simulated Mixed Layer Depth (MLD) is estimated following the criterion of de Boyer Montegut et al., (2004). The spatial distributions of climatological monthly mean MLD show similar pattern of the observation, except for winter season in the Kuroshio extension regions and north of the East Sea (Fig. 3). The bias of simulated MLD in winter is shown to be attributed to the inherent error of the model vertical coordinate. The interannual variations of MLD south of Vladivostok in the East Sea indicate that the deep convection is related to cold air temperature and strong cyclonic wind stress. In addition, the deep MLD is found when the coastal upwelling occurred due to the strong southerly winds in the east of Korea.

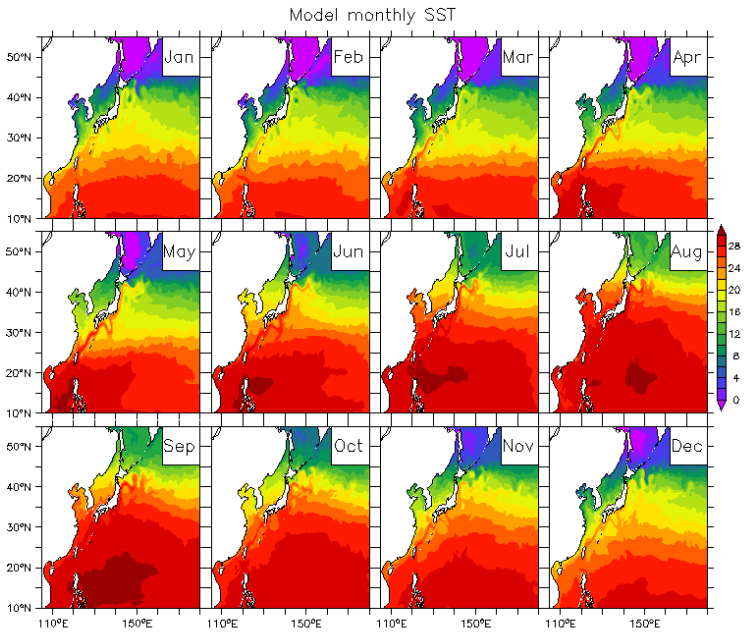

Figure 2. The monthly mean SST simulated in the ROMS model

4. Conclusion

We developed a regional ocean climate model to investigate interannual variations of the present ocean climate for the western North Pacific marginal seas, in particular, focused on the East Sea. The model results show that the time series of the SST mean and variance value in all marginal sea are comparable to the Levitus climatology. The linear trend of simulated SST is similar to that of monthly ERSST, but model cannot simulate negative long-term changes of ocean intermediate layers in the east of Korea, shown in KODC observations during summertime. Although the time-averaged model transport in the Tsugaru Strait is underestimated due to topography smoothing in the East China Sea shelf, the vertical structure of current in the PN line shows a similar pattern of the observation. The simulated MLD is compared with Montegut MLD, showing the bias in winter due to model internal error. We suggest that this model show the

reasonable results for regional climate model. In the future, this model will be corrected with the Kuroshio and the East Korea Warm Current overshooting and transport problems and compared with coupled model to study the future projection for the seas around Korea.

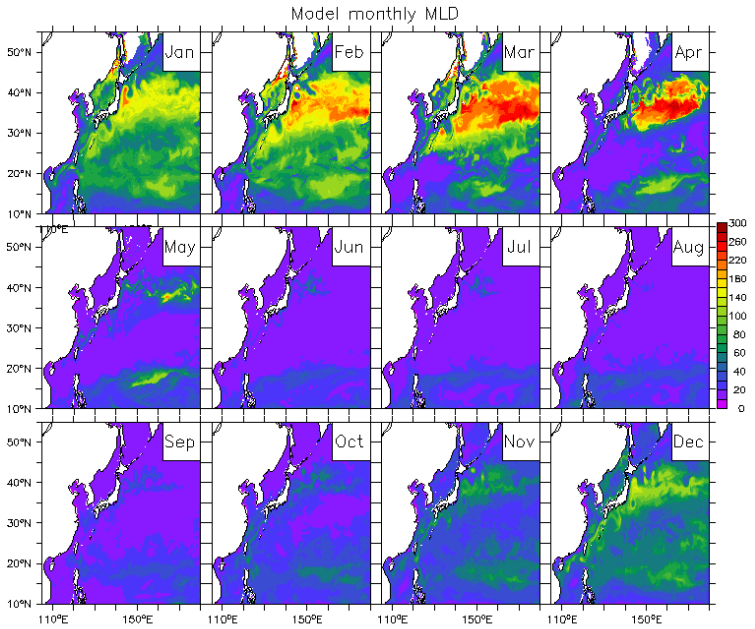

Figure 3. The monthly mean MLD simulated in the ROMS model

References

1. de Boyer Montegut, C., G. Madec, A. S. Fischer, A. Lazar, and D. Iudicone, Mixed layer depth over the global ocean: An examination of profile data and a profile-based climatology, 2004. J. Geophys. Res., 109, C12003, doi:10.1029/2004JC002378.
2. Kang, H. S., C., N.K. Mooers, Diagnoses of simulated water-mass subsuction/formation /transformation in the Japan/East Sea (JES), 2004. Deep-Sea Res. II 52 (2005), 1505-1524.
3. Marchesielllo, p., J. C. McWilliams, A. Shchepetkin, Open boundary conditions for long-term integration of regional oceanic models, 2000. Ocean Modelling 3 (2001), 1-20.
4. Oka, E., M. Kawabe, Characteristics of Variations of Water Properties and Density Structure around the Kuroshio in the East China Sea, 1998. J. Oceanogra. 54, 605-617.
5. Park, K. A., K.-R. Kim, Unprecedented coastal upwelling in the East/Japan Sea and linkage to long-term large-scale variations, Geophys. Res. Lett., 37, L09603, doi:10.1029 /2009GL04 2231, 2010.
6. Tally, L. D., V. Lobanov, V. Ponomarev, A. Salyuk, P. Tishchenko, I. Zhabin, S. Riser, Deep convection and brine rejection in the Japan Sea, Geophys. Res. Lett., 30(4), 1159, doi:10.102 9/2002GL016451, 2003.
7. Teague, W. J., G. A. Jacobs, H. T. Perkins, J. W. Book, K.-I. Chang, and M.-S. Su, 2002: Low-frequency current observation in the Korea/Tsushima Strait. J. Phys. Oceanogr., 32, 1621-1641.

Effects of mixed layer depth on the changes in the sea surface temperature under global warming in CMIP5 models

Dongwon Yi[1,2], Chan Joo Jang[1], Sang-Wook Yeh[2], Yong Sun Kim[1]

[1]Ocean Circulation and Climate Research Division, Korea Institute of Ocean Science and Technology, Ansan, 426-744, Korea

[2]Department of Marine Sciences and Convergence Technology, ERICA, Hanyang University Ansan, 426-791, Korea

E-mail: yidongwonyi@gmail.com

1. Introduction

The mixed layer depth (MLD) responds directly to atmospheric fluxes. In recent study, it is reported that MLD is a key parameter for regulating the response of tropical Pacific mean the sea surface temperature (SST) to increasing greenhouse gases[2]. Thus, understanding the role of the MLD on the changes in the SST is important to project future climate[1]. This study investigates effects of the MLD on the changes in the SST within the equatorial Pacific under the historical and RCP4.5 using the Coupled Model Intercomparison Project Phase 5 (CMIP5) simulation data sets.

2. Model and Methods

This study utilized 12 coupled general circulation model (CGCM) simulations[3]. These models are provided by the Intergovernmental Panel on Climate Change (IPCC) Fifth Assessment Report (AR5) and its data are available from the Program for Climate Model Diagnosis and Intercomparison (http://cmip-pcmdi.llnl.gov/cmip5).

There are two scenarios: the “historical” run forced by observed atmospheric composition changes covering over the industrial period (from the mid-nineteenth century to near present) thus referred to as “twentieth century” simulations, and “future” projection simulations forced with a midrange mitigation emissions scenario (RCP4.5) to project future climate. To analyze effects of the MLD changes on SST, two groups are classified as “shallow” and “deep” groups based on the annual mean MLD values of each model in a common historical run period (1901-2000) in the tropical pacific (120^{o}E-90^{o}W, 15^{o}S-15^{o}N). MLD was defined as a depth where water temperature changes in 0.5 °C from the surface temperature.

3. Results

To analyze the relationships between MLD and SST, annually-averaged fields are again averaged to group mean values. In MLD difference between shallow and deep group in historical period, as shown in Figure 1, it differs up to 30 meter on whole equatorial pacific region, which is consistent with SST difference except eastern equatorial pacific and coastal region. In figure 1a, the regions where SST difference shows negative maximum of 1 to 2 degrees, are off the equator in both hemispheres, implying that the turbulent mixing process within the MLD affects directly on SST warming in these regions. Whereas the region, where the negative maximum SST

difference locates on the eastern equatorial (see, red circle in Fig 1b) is not likely affected by the changes of MLD. One of candidates controlling SST there might be wind-driven upwelling that is a dominant process along the eastern Pacific coast[4]. Analyzing SST and MLD temporal variability both the shallow and deep groups, the domain averaged SSTs from the both groups gradually increases as the MLDs decreases during 100 year (not shown). The MLD in shallow group shows a higher SST trend than one for the deep group. It indicates that SSTs of the shallow MLD group is relatively sensitive to the changes of atmospheric heat flux. Similarly, in case the ratio between MLD and SST changes (=ΔSST/ΔMLD) over 100 year in historical period, the SST in shallow group reveals higher value more than 3 times than the deep group, implying relatively greater changes in MLD temperature compared to deep MLD.

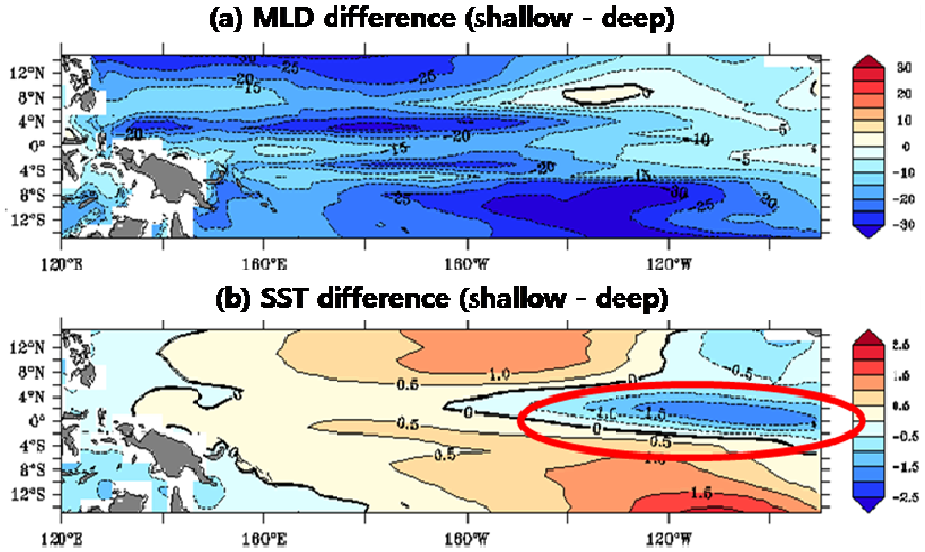

Figure 1. (a) MLD (m) and (b) SST (℃) ensemble differences between shallow and deep groups in equatorial Pacific in historical run (1901-2000).

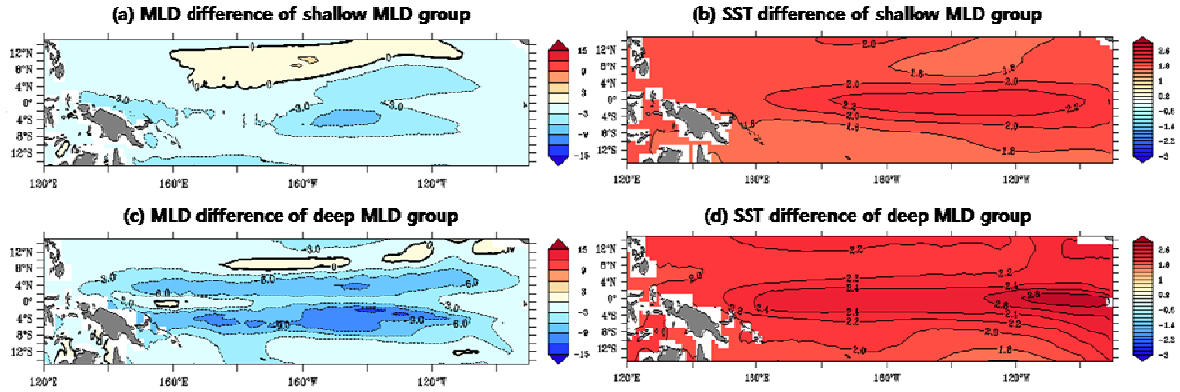

Figure 2. Ensemble differences between RCP4.5 and Historical (RCP4.5 - Historical) run in MLD (m) and SST (℃) of the shallow and deep MLD groups.

Figure 2 shows the MLD and SST differences between RCP4.5 and historical scenarios (RCP4.5 – historical) in two MLD groups. The MLD difference in most equatorial regions except small part of northern hemisphere shows that MLD becomes shallower in both groups and appears the lowest value in nino3.4 (170^{o}W-120^{o}W in Fig. 2a, c) region. The depth change of MLD in the deep group is two times bigger than shallow group, and then it seems that the SST warming is also bigger in deep group than shallow group. However, the ratio ($℃ \cdot m^{-1}$) of SST and MLD indicates a different result that MLD in the shallow group shows higher ratio relatively than the deep group. That means the shallow group reacts sensitively by heat forcing and warms SST more than the deep group. It is clear that SST becomes warmer in future and the SST warming is shown centering on the equator and maximum rise about 3 degrees in eastern equator (Fig. 2b, d). Suggesting the temperature gradient in the east-west equator will be reduced.

4. Discussion and conclusions

We analyzed two simulations, the control simulation using industrial greenhouse gas concentrations (historical run) and the experiment simulation using doubled CO_2 concentrations (RCP4.5 run) to investigate relationship of changes in the MLD with SST changes under the anthropogenic climate change in selected data set from CMIP5 simulations. The shallow MLD group simulated higher SST compared to the deep group in all equatorial Pacific regions except eastern equator and near the coast during historical period. The region has high value of SST difference along the off equator in mid Pacific consisted with maximum value of MLD difference. Therefore, it proved that MLD shoaling enhances stratification in the upper ocean and then it leads to SST warming.

The projected changes in SST as well as MLD are larger at the deep group than the shallow group, and thus it allows us to expect that MLD in deep group might become much shallow and result in steep SST warming. However, the ratio of SST difference and MLD difference in all period showed the higher value in shallow group than deep group, implying that models with shallow MLDs have a substantial SST increase, thus enhancing surface stratification in the ocean and this process constitutes a positive feedback between MLD and SST. Therefore, to confirm this feedback, the future study about the stratification in the CMIP5 model will be necessary.

References

1. Carton, James A., Grodsky, Semyon A., Liu, Hailong. 2008. Variability of the Oceanic Mixed Layer, 1960-2004. *American Meteorological Society*, 1029-1047, doi:10.1175/2007JCLI1798.1.
2. Yeh, Sang-Wook., Yim, Bo Young., Noh Yign., Dewitte, Boris. Changes in mixed layer depth under climate change projections in two CGCMs. *Climate dynamics* 33.2-3 (2009): 199-213.
3. Taylor, Karl E., Ronald J. Stouffer, Gerald A. Meehl, 2012: An Overview of CMIP5 and the Experiment Design. *Bull. Amer. Meteor. Soc.*, 93, 485–498.
4. Halpern, D., R. A. Knox, D. S. Luther, and S. G. H. Philander (1989), Estimates of equatorial upwelling between 140° and 110°W during 1984, J. Geophys. Res., 94(C6), 8018–8020, doi:10.1029/JC094iC06p08018.

Decadal variability and cooling trend of intermediate layer heat content in the southwestern East/Japan Sea

Seung-Tae Yoon, Kyung-Il Chang

School of Earth Environmental Science, Seoul National University, Korea
E-mail: styoon@curl.snu.ac.kr

1. Introduction

Recent studies clearly show that global oceans are undergoing secular changes. Heat content of the world's upper ocean (0-300m) increased by 7.03×10^{22}J between 1955 and 2003, which corresponds to mean temperature increase of 0.171℃ (Levitus et al., 2005). The upper ocean heat content averaged over the regional oceans, however, exhibits large decadal variations rather than a monotonic warming (e.g., Palmer et al., 2009). Also basin-averaged changes and variability can often mask important spatial differences (Lozier et al., 2008). In the East/Japan Sea (EJS), the basin-averaged, non-seasonal upper ocean heat content down to 300 m also shows an increasing trend superimposed on a large decadal variation (Na et al., 2012). However, there exists a regional difference in the heat content variation, notably a cooling trend in the southwestern EJS, the Ulleung Basin (UB).

The upper 100 m of the UB receives warm surface waters from the south carried by the Tsushima Warm Current, and colder waters originating from the north of the subpolar front occupies the thick layer below the warm waters. The cold waters consist of the East Sea Intermediate Water (ESIW, Kim and Chung, 1984), Deep Water, and Bottom Water (Kim et al., 2004). The ESIW has a potential temperature range of 1~5°C with a depth range of 100~500 m, and it is carried to the UB either by the coastal current (North Korean Cold Current) or by subduction along the subpolar front. Hence, the warm and cold water advection would affect the upper-layer heat content in the UB as well as local air-sea heat exchanges.

This study aims to investigate the upper-ocean (0~500 m) heat content variability in the UB using a 36-year bi-monthly temperature dataset from 1976 to 2011 provided by Korea Oceanography Data Center (KODC). The KODC temperature data are provided at standard depths (0, 10, 20, 30, 50, 75, 100, 125, 150, 200, 250, 300, 400 and 500 m). A standard quality control of data was performed before calculating the heat content.

2. Characteristics of heat content anomaly (HCA) variation

We divide the upper 500 m depth into upper and lower layers with their respective integrated heat content anomalies of UHCA and LHCA. The LHCA from 100 m to 400 m has a significant (95%) negative trend, while UHCA from 0 m to 50 m has an increasing trend during 36 years (Fig. 1). The increasing trend in the UHCA is not statistically significant.

Time series of LHCA is similar to the HCA for the total layer (THCA), and characterized by an interdecadal variation before 2000, predominant negative anomalies without any distinct interdecadal variation after 2000 (Fig. 1a, 1c). Both the THCA ($-4.82 \pm 4.59 \times 10^7$ J/m^2/year) and LHCA ($-4.65 \pm 3.10 \times 10^7$ J/m^2/year) have a significant decreasing trend. The UHCA

also shows an interdecadal variation before 1996 concurrent with the LHCA, while shorter period fluctuations with predominant positive anomalies are obvious after 1996 (Fig. 1b). The UHCA has long-term positive trend ($0.33 \pm 0.75 \times 10^7$ J/m^2/year), but it is not statistically significant. Hence, the UHCA and LHCA co-varied before around 1996-1997, but their variations were decoupled afterwards until about 2008.

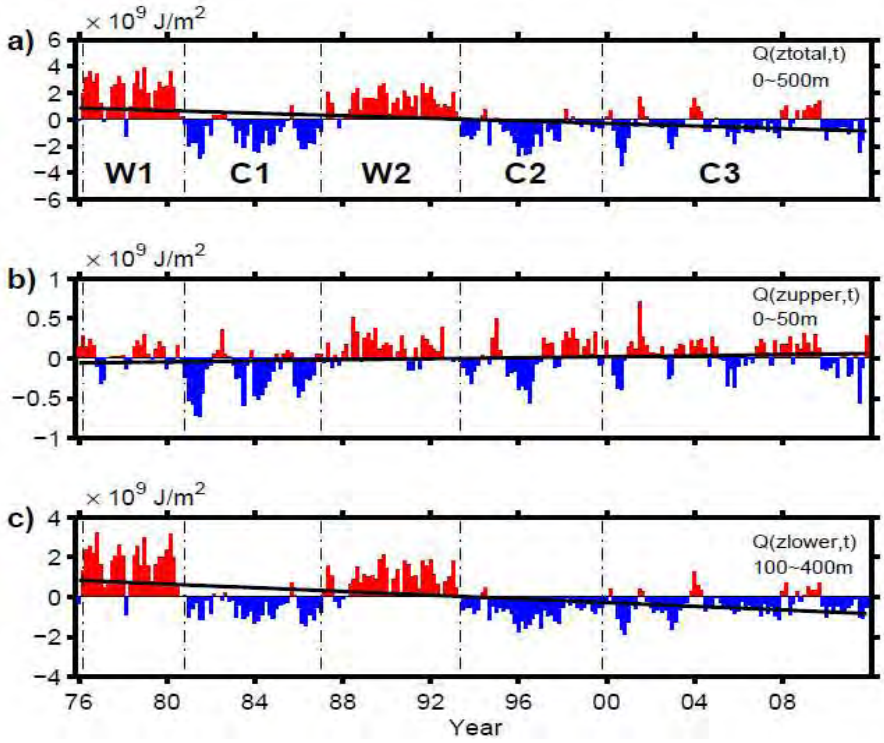

Figure 1. Time series of basin-averaged non-seasonal heat content anomalies, (a) THCA, (b) UHCA, and (c) LHCA. Five periods of high (W) and low (C) HCA are also shown.

To understand the causal mechanisms of the UHCA and LHCA variations, we divided total period into five sub-periods based on the THCA time series; W1 - from April, 1976 to December, 1980, C1 - from February, 1981 to February, W2 - from April, 1987 to June, 1993, C2 - from August, 1993 to December, 1999, and C3 - from February, 2000 to December C3 (Fig. 1a).

3. Spatial pattern of temperature in each sub-period

We calculate temperature anomalies at 30 m and 200 m in each sub-period by subtracting the record-length mean temperature from mean temperatures during the each sub-period (Figs. 2, 3). Mean temperature distribution at 30 m during the entire study period shows that most of the UB is occupied by warm waters with temperature higher than 10°C, indicating the influence of the Tsushima Warm Current (Fig. 2a). The record-length mean temperature at 200 m ranges 1~5°C, which corresponds to the temperature range of the ESIW (Fig. 3a).

During the W1 and W2 sub-periods, positive temperature anomalies over 1℃ prevailed at 30 m especially in the northern part of the UB (Fig. 2b, 2c). On the contrary to sub-periods W, negative temperature anomalies are predominant at 30 m in the northern part of the UB during the C2 and C3 sub-periods, but the anomaly values do not exceed 1.0°C (Fig. 2e, 2f). During the

C1 sub-period, negative temperature anomalies occurred at all stations with anomalies larger than 2°C in the northwestern and southeastern regions (Fig. 2d).

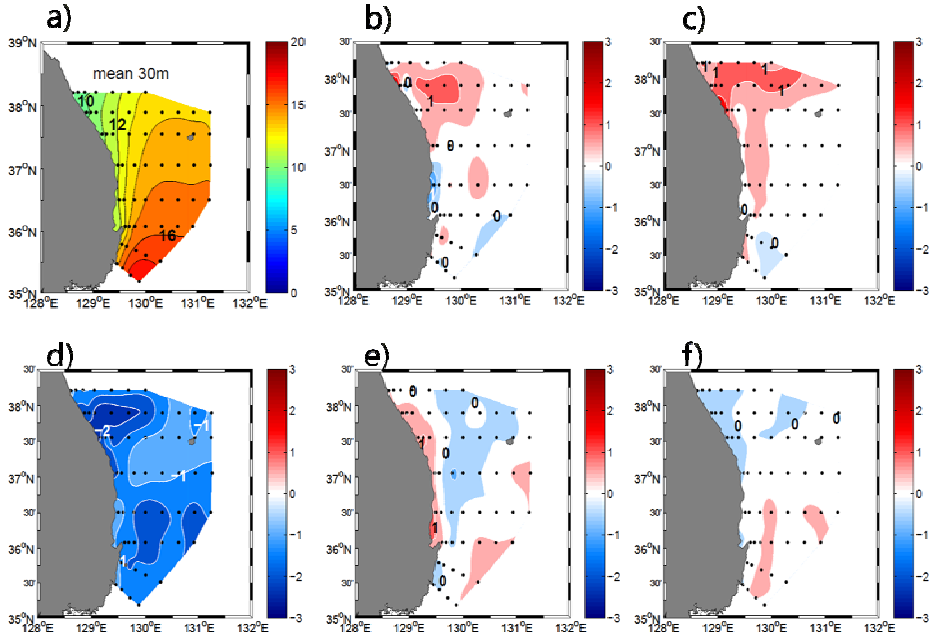

Figure 2. Horizontal distributions of (a) mean temperature, and temperature anomalies during the sub-periods (b) W1, (c) W2, (d) C1, (e) C2, and (f) C3 at 30 m.

The LHCA is thought to be mainly affected by the influence of the ESIW having a temperature range from 1 to 5℃. During the sub-periods W1 and W2, positive anomalies can be seen at 200 m at most stations and the anomaly values are especially large during the sub–period W1 (Fig. 3b). Temperature anomalies at 200 m are negative at all stations during the C1, C2, and C3 sub-periods, and especially strong during the C2 sub-period (Fig. 3e).

We also calculated temperature anomalies at each standard depth level by subtracting mean temperature over the entire period from mean temperature over the each period (Fig. 4). The temperature anomalies are positive (negative) at the whole depth during W1 and W2 (C1) but the temperature anomalies during C2 and C3 are positive at upper layer and negative at lower layer. Thus the predominant negative THCA and LHCA and positive UHCA in recent years during C2 and C3 are due to the negative temperature anomalies at lower layer and positive anomalies in the upper layer. Also shown in Fig. 5 are basin-averaged depths of three isotherms (10°C, 5°C, and 1°C), showing that all isotherms deepened during W1 and W2 while they shoaled during C1. The two isotherms of 1°C and 5°C remained positive during C2 and C3, and the 10° isotherm changed little from W2 to C3.

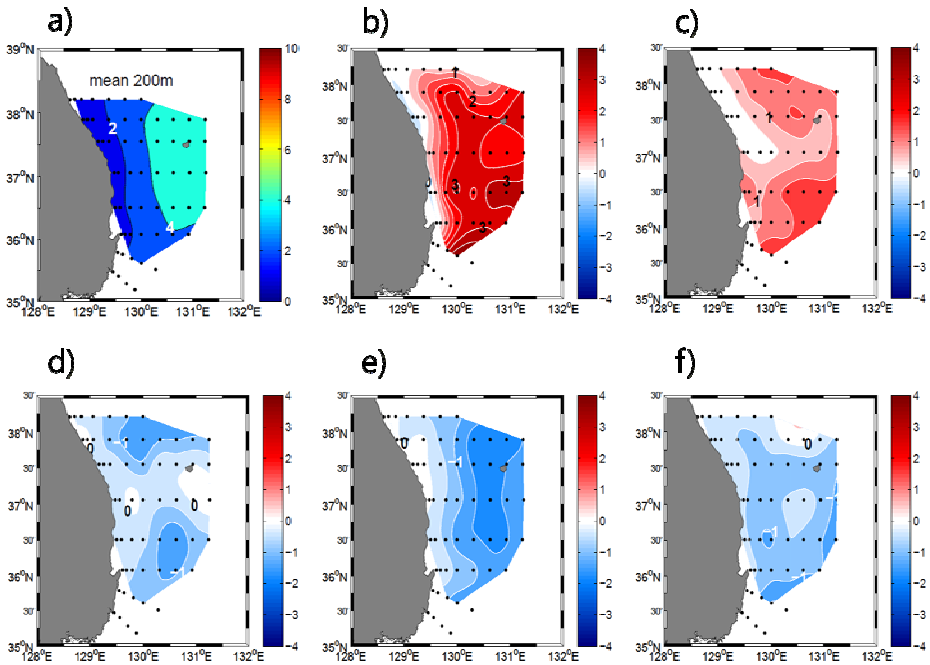

Figure 3. Horizontal distributions of (a) mean temperature, and temperature anomalies during the sub-periods (b) W1, (c) W2, (d) C1, (e) C2, and (f) C3 at 200 m.

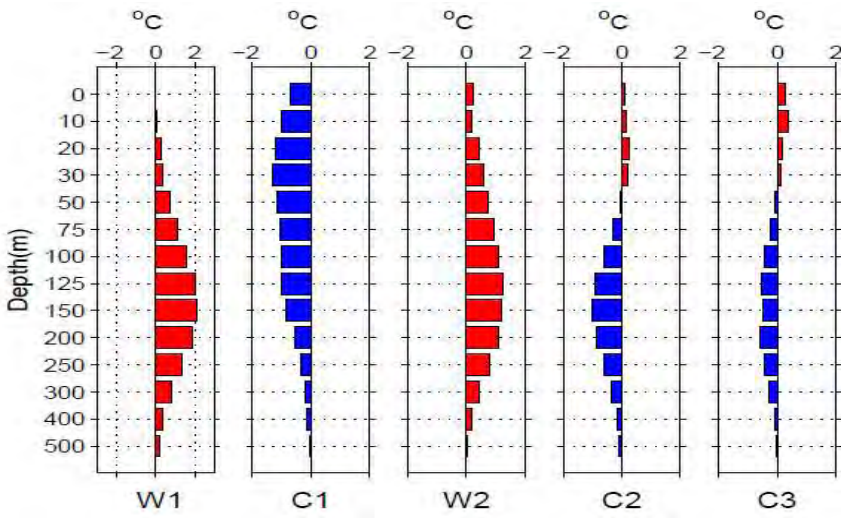

Figure 4. Temperature anomalies at standard depth levels during five sub-periods.

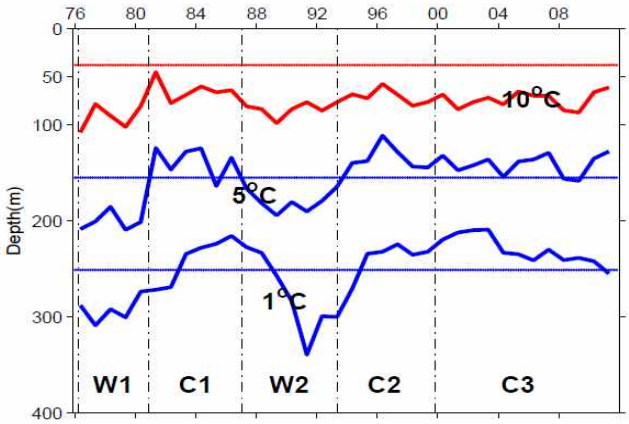

Figure 5. Basin averaged depths of 10℃, 5℃, and 1℃ isotherms.

4. Conclusion

We demonstrate the regional HCA variability in the southwestern East Sea is determined by the strengthening or weakening of the Tsushima Warm Water (TWW) of the southern origin and cold East Sea Intermediate Water (ESIW) of the northern origin. The two warm sub-periods of W1 and W2 are due to strengthening of the TWW and weakening of the ESIW. On the contrary, the C1 sub-period was characterized by the strengthening of the ESIW and weakening of the TWW. Both the TWW and ESIW were influential during the most recent sub-periods, C2 and C3, and the UHCA and LHCA showed opposite HCA. The cooling trend of the HCA during the entire period is due to the persistent negative LHCA since 1994.

Reference

1. Kim, K., et al. (2004). Water masses and decadal variability in the East Sea (Sea of Japan). Progress in Oceanography 61(2-4): 157-174.
2. Levitus, S. (2005). Warming of the world ocean, 1955–2003. Geophysical Research Letters 32(2).
3. M. Susan Lozier., et al. (2008). The spatial Pattern and Mechanisms of heat-content change in the North Atlantic. Science 319: 800-803.
4. Palmer, M. D., et al. (2009). A new perspective on warming of the global oceans. Geophysical Research Letters 36(20).
5. Yanlin Cui and Tomoharu Senjyu. (2010). Interdecadal Oscillations in the Japan Sea Proper Water related to the Arctic Oscillation. Journal of Oceanography 66: 337-348.
6. Park, S., et al. (2011). Interannual-to-interdecadal variability of the Yellow Sea Cold Water Mass in 1967-2008: Characteristics and seasonal forcings." Journal of Marine Systems 87(3-4): 177-193.
7. Na, H., et al. (2012). Decadal variability of the upper ocean heat content in the East/Japan Sea and its possible relationship to northwestern Pacific variability. Journal of Geophysical Research 117 (C2).